

**THE EFFECT OF CHLORIDE CONCENTRATION ON THE CORROSION-FATIGUE
CRACK BEHAVIOR OF AN AGE-HARDENABLE MARTENSITIC STAINLESS STEEL**

(CUSTOM 465)

A Thesis

Presented to

the faculty of the School of Engineering and Applied Science

University of Virginia

in partial fulfillment

of the requirements for the degree

Master of Science

By

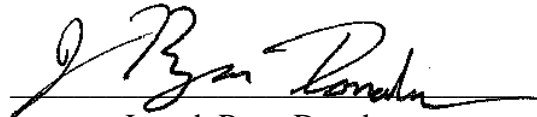
Joseph Ryan Donahue

May

2015

Approval Sheet

The thesis
is submitted in partial fulfillment of the requirements
for the degree of
Master of Science



Joseph Ryan Donahue

This thesis has been read and approved by the examining Committee:

Advisor (James T. Burns)

Committee Chair (Robert G. Kelly)

James M. Fitz-Gerald

Accepted for the School of Engineering and Applied Science:



Dean, School of Engineering and Applied Science

May

2015

Abstract

Ultra-high strength stainless steels (UHSSS) are desirable for aerospace structural components due to their desirable mechanical properties and corrosion resistance. While these steels are more resilient to corrosive environments than their low-alloy counterparts, concentrated aqueous chloride environments are reported to be highly detrimental to the fatigue endurance limit of these stainless steels when compared to less concentrated environments. This research seeks to better understand this deleterious effect by independently studying the effect of various environments (and related corrosion damage) on the pit-to-crack transition, crack initiation life, and short/long crack growth kinetics. To study this behavior fatigue experiments are carried out in aqueous solutions ranging from distilled water to 0.0006-3.0M NaCl. Two types of experiments are performed. First, dog-bone fatigue specimens are subject to one of four pre-fatigue corrosion conditions to induce pitting damage to induce a pit-to-crack transition under constant maximum load fatigue. Scanning electron microscopy is used to characterize the initiation site and capture load-induced marker bands imparted during fatigue. These markings are used to quantify initiation life and small crack growth behavior. Second, single edge notch specimens are used to quantify the long crack growth kinetics, in which a direct current potential drop technique is used to monitor the crack progression, thus providing real-time control of the ΔK -based loading protocol.

Custom 465 is shown to be highly corrosion resistant, such that localized surface corrosion damage (from several exposure conditions in NaCl-based solutions) is not sufficiently severe to form a crack. Rather, microstructural inclusions and other features dictate crack nucleation location. Short crack growth is shown to be highly dependent on local microstructure and relatively insensitive to the bulk chloride concentration. Long crack growth was shown to be relatively insensitive to the bulk chloride concentration as modeling predictions estimate that crack growth rates taken from various NaCl environments exert a minimal effect on fatigue life. Initiation life, however, exhibits a strong dependence on bulk chloride concentration and is likely the main factor governing similar trends in the overall fatigue life. Such precise knowledge of

factors governing fatigue life will improve fatigue behavior modeling by incorporating environmental effects on fracture mechanics and stress/strain life predictions.

Acknowledgements

This work was funded by the US Office of Naval Research (Vasudevan/Mullins) and the DoD Corrosion Office (Hayes).

Table of Contents

Approval Sheet	ii
Abstract	i
Acknowledgements	iii
Table of Contents	iv
List of Tables	vi
List of Figures	vii
Nomenclature	xvi
1 Introduction	1
1.1 Background of Aerospace Steels	2
1.2 Goals	3
1.2.1 Background	6
1.2.1.1 Pitting in Stainless Steel	6
1.2.1.2 Crack Initiation	9
1.2.1.3 Crack Growth	11
2 Experimental	15
2.1 Phase I	16
2.2 Phase II	19
2.2.1 Mechanical Loading Parameters	19
2.2.2 Loading Environment	20
2.2.3 Specimen Pre-Fatigue Exposure Condition	20
3 Results and Discussion	22
3.1 Goal 1: Pitting Characteristics under Various Conditions	22
3.1.2 Corrosion Exposure Protocol Development	25
3.2 Goal 2: Effect of Various Exposure Conditions on Fatigue Life	26
3.2.1 Condition 1	27
3.2.2 Condition 2/3	28
3.2.3 Condition 4	30

3.2.3.1 Characterization of the Crack Formation Location within the Pit	31
3.2.3.2 Macro-scale Pit Characteristics	33
3.3 Goal 3: Quantitatively Assess the Influence of [Cl ⁻] on Fatigue Life	35
3.4 Goal 4: Establish Relative Influence of [Cl ⁻] on Different Fatigue Regimes	36
3.4.1 Crack Propagation	37
3.4.1.1 Long Crack Growth	37
3.4.1.1.1 Increasing K	38
3.4.1.1.2 Decreasing K	39
3.4.1.1.3 Corrosion Fatigue	40
3.4.1.2 Small Crack Growth	41
3.4.1.2.1 Variability in Growth Rates	42
3.4.1.2.2 Effect of [Cl ⁻] on Small Crack Growth	43
3.4.2 Crack Formation Life	44
3.4.2.1 Effect of Chloride Concentration on Initiation Life	44
4 Conclusions	46
5 Tables and Figures	49
Appendix A	106
A.1 Validation of SCC	106
A.2 Sub-threshold Fatigue Cracking	108
A.2.1 Ripple Load Effects	109
Appendix A Figures	113
Appendix B	122
Appendix B Figures	123
6 References	126

List of Tables

Table 1: Compositions of UHSSS used in aerospace applications, reproduced from Garrison 1990 [17].

Table 2: Mechanical properties of UHSSS used in aerospace applications, reproduced from Garrison 1990 [17].

Table 3: Composition of Custom 465 as reported by Carpenter [30].

Table 4: Mechanical properties of Custom 465-H950 reported by Carpenter [30].

Table 5: Phase II exposure condition and polarization parameters are listed here. “Adj. Pol.” denotes pre-fatigue polarizations that had to be truncated. Test 2 and 14 did not produce any data.

Table 6: Conditions at which decreasing- ΔK da/dN deviates from linear behavior.

List of Figures

Figure 1: Research by Hata shows that UHSSS exposure to aqueous chloride environments may decrease fatigue life of UHSSS (in this case a 13%Cr SUS410JI). Reproduced from Hata 2008 [6].

Figure 2: A typical representation of autocatalytic pit growth in a sodium chloride aqueous solution. Oxygen is depleted towards the base of the pit, and diffusion of oxygen through solution is too sluggish to maintain aeration of solution at the base of the pit. The tip of the pit acidifies as the base metal hydrolyzes to form metal hydroxides. Chloride anions migrate into the pit to neutralize the ionic imbalance from the formation of positively charged metal hydroxides. Reproduced from Fontana, 2005 [150].

Figure 3: Proposed mechanism of pitting at an MnS inclusion in steels. Reproduced from Baker 1993 [49].

Figure 4: Electrochemical reactions in an immersed crack. Electrochemical reactions both at the crack tip and along the crack walls create an aggressive chemistry that may occlude the crack tip from the bulk solution. Figure reproduced from Turnbull 2001 [151].

Figure 5: Low (a) and high (b) magnification SEM backscatter electron images of polished C465-H950 (working distance=1-2mm, positive stage bias).

Figure 6: Electron backscatter diffraction (EBSD) orientation maps of Custom465. Small (50-250 nm) islands of retained austenite are denoted by white arrows. Low magnification maps (a) were obtained using a step size of 250 and 200 nm, respectively. High magnification maps (b) were obtained using a step size of 12 nm. Reproduced from Pioszack 2013 [115].

Figure 7: A schematic detailing Phase I specimen design.

Figure 8: Optical micrograph side view of the square notch.

Figure 9: In Phase I, the specimen is loaded into a 360mL Plexiglas cell, loaded into a test frame and connected to a potentiostat.

Figure 10: General representation of the wave forms used for the increasing-K (a) and decreasing-K (b) Phase I fatigue tests. Reproduced from Herman, 1988 [127].

Figure 11: Wires are spot-welded close to the notch to collect dcPD measurements. Exposed sections of the wire were coated in stop off lacquer to prevent corrosion of the electrical leads.

Figure 12: Schematic detailing the Phase II dog-bone specimen design.

Figure 13: In Phase II, the dog-bone specimen is loaded into a 500mL Plexiglas cell, loaded into a test frame and connected to a potentiostat.

Figure 14: This figure explains the placement of Condition 4 pits on a Phase II fatigue specimen. (a) A basic rendering showing pit placement (black dots) on one side of a fatigue specimen. The hidden side has an identical arrangement of pits. (b) An optical image showing pit placement on an actual specimen.

Figure 15: An overview of pre-fatigue pit characterization and analysis via white light interferometry is presented in (a). The operations shown are a fraction of potential analyses. (b) shows an SEM secondary electron image of the same pit.

Figure 16: OCP measurements taken 1 hour prior to fatigue from Condition 4 specimens in various NaCl environments.

Figure 17: Example of corrosion damage in C465 after 1 year of full immersion in 0.6M NaCl. The feature shown is less than $2\mu\text{m}$ in diameter and lacks significant depth.

Figure 18: Polished C465 electrode after 36 hours of polarization at $150\text{mV}_{\text{SCE}}$ in a 0.6M NaCl solution. Pits litter the polished surface and measure less than $1\mu\text{m}$ in all dimensions.

Figure 19: Profilometry of the surface of a C465-H950 electrode post-polish obtained via white light interferometry.

Figure 20: This is an example of a larger flaw generated by the Condition 3 exposure with a 3D rendering provided in (a) and a cross-sectional profile provided in (b).

Figure 21: Backscatter electron image of a Condition 4 pit prior to cleaning. The dark phases are primarily chromium-oxides, validated by EDS.

Figure 22: Low (a) and high (b) magnification images of the cross-section of a pit typical of the Condition 4 exposure. The red highlighting indicates the body of the pit.

Figure 23: A plot of C465-H950 fatigue lives for various chloride concentrations tested at $R=0.5$, a frequency of 2Hz, and a maximum stress of 1153MPa. Data is presented for each specimen condition 1-4 described in the text.

Figure 24: Micrographs of C465-H950 of polished dog-bone specimen fatigued in humid N_2 at an $R=0.5$, $f=2$, and a maximum stress of 1153MPa. (a) contains an overview micrograph of the fracture surface proximate to the initiation site of polished dog-bone specimens fatigued in humid N_2 . Grain(s) immediately about the initiation site are cleaved (b), but intergranular fracture dominates past this point and continues for several hundred micrometers (c).

Figure 25: Initiation site of a Condition 2 dog-bone specimen polarized to $-200mV_{SCE}$ for 24 hours prior to fatigue. Fatigue was conducted at an $R=0.5$, $f=2$, and a maximum stress of 1153 MPa. Secondary electron (a) and backscatter electron (b) micrographs of a typical TiC inclusion responsible for crack nucleation.

Figure 26: This EDS image of the TiC particle (red) shows that it is a secondary phase inclusion distinct from the matrix. This is the same inclusion as seen in Figure 25.

Figure 27: These secondary and backscatter electron micrographs exemplify titanium carbide inclusions observed in the path of the crack. This Condition 2 specimen was polarized to $-200\text{mV}_{\text{SCE}}$ for 24 hours prior to fatigue. Fatigue was conducted at an $R=0.5$, $f=2$, and a maximum stress of 1153 MPa.

Figure 28: Typical current flow associated with pre-fatigue and fatigue polarizations of $150\text{mV}_{\text{SCE}}$ and $-200\text{mV}_{\text{SCE}}$ respectively in 0.6M NaCl.

Figure 29: Low magnification (a) and high magnification (b) SEM image of a Condition 3 specimen polarized to $100\text{mV}_{\text{SCE}}$ for 15 minutes prior to fatigue. Fatigue was conducted at an $R=0.5$, $f=2$, and a maximum stress of 1153 MPa.

Figure 30: These plots contain all Condition 2 and 3 specimens initiating on a TiC particle. Fatigue was conducted at an $R=0.5$, $f=2$, and a maximum stress of 1153 MPa. Fatigue life is plotted against TiC depth into microstructure (a) and 2D cross-sectional area (b).

Figure 31: Micrograph of initiating TiC particles from a Condition 2 specimen polarized to $-200\text{mV}_{\text{SCE}}$ for 24 hours prior to fatigue. Fatigue was conducted at an $R=0.5$, $f=2$, and a maximum stress of 1153 MPa. A TiC inclusion with a sharp edge protruding into the matrix is seen in (a) and a more blunt TiC inclusion is seen in (b).

Figure 32: Initiation site of a Condition 2 specimen polarized to $-200\text{mV}_{\text{SCE}}$ for 24 hours prior to fatigue. Fatigue was conducted at an $R=0.5$, $f=2$, and a maximum stress of 1153 MPa. A backscatter electron image (a) and a corresponding EDS image (b) show the silicon inclusion initiating the crack. This initiating particle was located underneath stop off lacquer, unaffected by bulk environment.

Figure 33: EDS from a Condition 3 specimen polarized to $150\text{mV}_{\text{SCE}}$ for 1 hour prior to fatigue. Fatigue was conducted at an $R=0.5$, $f=2$, and a maximum stress of 1153 MPa. This EDS shows the TiS inclusion responsible for one crack initiation underneath the lacquer. The overview,

inclusive of all elements, is shown in (a). For clarity, individual profiles of titanium (b) and sulfur (c) are included.

Figure 34: Close-up images of initiation point as indicated by the red arrow in (a) conducted in 0.06M [Cl⁻] and (b) conducted in 3.0M [Cl⁻].

Figure 35: SEM and white light profilometry from a Condition 4 specimen fatigued at R=0.5, f=2, and a maximum stress of 1153 MPa. Initiation location (green box) can be easily determined on the fracture surface (a) via the marker band technique. Once the location has been identified on the fracture surface, it can also be found at the edge of a fractured pit on the corroded surface (b). The initiation location can be traced on an image of the pit pre-fatigue (c) and can be correlated to the height profile shown in (d). This provides exact metrics regarding crack initiation location. The relative height scale in (d) ranges from 0 μ m (black) to 60 μ m (pink).

Figure 36: (a) Crack initiation locations for all Condition 4 specimens are plotted on a generic representation of a pit 175 μ m in diameter. Initiation locations are condensed into a single quadrant represented by the box on the colored pit image. The origin represents the exact center of the pit. The red box highlights the pit area within 40 μ m of the centerline. The green circles indicate crack initiation at an inclusion particle in (a). (b) shows a secondary electron image of a pit initiating a crack within a pit. The white line delineates the fracture surface from the pit. The inclusion is circled in green.

Figure 37: Modeling efforts by Burns [126] (a) and Horner/Turnbull [127] (b) showing stress and strain profiles in hemispherical pits.

Figure 38: This graph shows pit initiation location as a function of chloride concentration. All data is taken from Condition 4 specimens polarized to -200mV_{SCE} for the duration of fatigue. Fatigue was conducted at an R=0.5, f=2, and a maximum stress of 1153 MPa.

Figure 39: Fatigue life is plotted against pit size in (a) (depth into microstructure) and 2D cross-sectional area (b). All data is taken from Condition 4 specimens polarized to -200mV_{SCE} for the

duration of fatigue. Fatigue was conducted at an $R=0.5$, $f=2$, and a maximum stress of 1153 MPa.

Figure 40: Identical to Figure 38 except this figure includes the $[Cl^-]$ of the environment. All data is taken from Condition 4 specimens polarized to $-200mV_{SCE}$ for the duration of fatigue. Fatigue was conducted at an $R=0.5$, $f=2$, and a maximum stress of 1153 MPa.

Figure 41: This plot includes all Condition 2 and 3 specimens initiating on a TiC inclusion and all Condition 4 specimens initiating from a pit. Fatigue was conducted at $-200mV_{SCE}$, an $R=0.5$, $f=2$, and a maximum stress of 1153 MPa. Initiating inclusion measurements are included for relevant Condition 2 and 3 specimens.

Figure 42: Fracture surface of a Condition 1 specimen fatigued at an $R=0.5$, $f=2$, and a maximum stress of 1153 MPa in humid N_2 . The red arrow shows direction of crack growth perpendicular to the initiating surface. (a) This is an overview of crack morphology for a humid N_2 test. (b) shows a higher magnification image of the transgranular cracking proximate to the initiation while (c) shows an example of competing fracture modes in an intergranular-dominated region.

Figure 43: da/dN data collected from SEN specimens the Phase I increasing- K regime. All fatigue was conducted at an $R=0.5$, $f=2$, and a nominal stress between 300-450MPa. K increased up to a K_{max} of $55MPa\sqrt{m}$.

Figure 44: Transgranular cleavage exemplifying typical fracture morphology in the Phase I increasing- K regime. This is taken from a specimen fatigued in a $0.0006M [Cl^-]$ solution at an $R=0.5$, $f=2$, and a nominal stress of 300MPa.

Figure 45: da/dN vs ΔK for the constant K_{max} -decreasing ΔK fatigue testing. All fatigue was conducted at an $R=0.5$, $f=2$ and a K_{max} of $55MPa\sqrt{m}$.

Figure 46: Increasing-K data more clearly demonstrating deviation from atmospheric crack behavior at low ΔK . The red arrows show the contribution of corrosion fatigue phenomena as an increase in da/dN from humid N_2 testing. The black line denotes the $\Delta K=11.5\text{MPa}\sqrt{\text{m}}$. All fatigue was conducted at an $R=0.5$, $f=2$, and a nominal stress between 300-450MPa. K increased up to a K_{max} of $55\text{MPa}\sqrt{\text{m}}$.

Figure 47: Low $[\text{Cl}^-]$ decreasing-K fatigue test. All fatigue was conducted at an $R=0.5$, $f=2$, and a nominal stress between 300-450MPa. K increased up to a K_{max} of $55\text{MPa}\sqrt{\text{m}}$.

Figure 48: Summary of the marker band identification process taken from a Condition 4 specimen fatigued at an $R=0.5$, $f=2$, and a maximum stress of 1153MPa in a 0.6M NaCl solution at $-200\text{mV}_{\text{SCE}}$. Marker bands are used to quantify initiation life and small crack growth. (a) shows a close up of a single marker band, highlighted by the white arrows. (b) shows an overview of the initiation feature and site to $\approx 400\mu\text{m}$ of crack depth. Low magnification allows for identification of marker bands further from the initiation site and a comprehensive shape of the crack front. (c) A high magnification stitch of the area close to the initiation point is represented by the green box. Short range marker bands measured along a single trajectory (red arrow) perpendicular to the initiation site.

Figure 49: Plot showing the minimal effect of $[\text{Cl}^-]$ on small crack growth kinetics nucleating at Condition 4 designer pits. Condition 4 specimen fatigued at an $R=0.5$, $f=2$, and a maximum stress of 1153MPa at $-200\text{mV}_{\text{SCE}}$.

Figure 50: Images of the initiation area of Condition 4 specimens fatigued at an $R=0.5$, $f=2$, and a maximum stress of 1153MPa at $-200\text{mV}_{\text{SCE}}$. Low magnification (a) and higher magnification (b) fractography of the initiation site of two Condition 4 pits in 3.0M NaCl solution.

Figure 51: N_i , $N_{i,25}$, and N_f for Condition 4 specimens fatigued at an $R=0.5$, $f=2$, and a maximum stress of 1153MPa in various NaCl environments and humid N_2 .

Figure 52: Total crack propagation life for Condition 4 specimen fatigued at an $R=0.5$, $f=2$, and a maximum stress of 1153MPa and a polarization of $-200\text{mV}_{\text{SCE}}$.

Figure 53: Overview shots of two Phase I tests fatigued at an $R=0.5$, $f=2$ and a nominal stress of 300MPa for the increasing-K test and fatigued at $K_{\text{max}}=55\text{MPa}\sqrt{\text{m}}$ and a decreasing- ΔK starting at $20\text{MPa}\sqrt{\text{m}}$ to threshold or failure. Both specimens were polarized to $-200\text{mV}_{\text{SCE}}$. The crack initiates at the notch on the right and propagates in the direction given by the red arrow. The fracture surface in (a) is from a specimen that was fatigued in 0.0006M aqueous NaCl, and the fracture surface in (b) is from a specimen that was fatigued in 0.6M aqueous NaCl. Both tests were polarized to $-200\text{mV}_{\text{SCE}}$.

Figure 54: This figure breaks down the fracture morphology of a C465-H950 SEN specimen fatigued in a 0.6M NaCl solution polarized to $-200\text{mV}_{\text{SCE}}$ in accordance with the increasing-K protocol where $R=0.5$, $f=2$, nominal stress = 300MPa, and the decreasing-K protocol where $K_{\text{max}}=55\text{MPa}\sqrt{\text{m}}$, $f=2$. Red arrows show the direction of crack propagation.

Figure 55: An abridged plot of decreasing- ΔK crack growth rates is presented to show the effect of frequency modulation. All fatigue was conducted with a K_{max} of $55\text{MPa}\sqrt{\text{m}}$ and polarized to $-200\text{mV}_{\text{SCE}}$.

Figure 56: Threshold stress intensity (K_{TH}) vs. applied potential (E_{app}) for Custom465 stressed in 0.6 M NaCl at an increasing-K rate of $1\text{MPa}\sqrt{\text{m/hr}}$. Open triangles indicate tests reaching maximum nominal load with no resolvable hydrogen-assisted crack growth. Reproduced from Pioszak 2013 [115].

Figure 57: Monotonic tensile testing performed showing K_{TH} , given by the sudden onset of stage I crack growth, and stage II crack growth rates. This test was performed on C465-H900 in 0.6M NaCl at an applied potential of $-575\text{mV}_{\text{SCE}}$. K rose at a rate of $1\text{MPa}\sqrt{\text{m/hr}}$. Reproduced from Pioszak 2013 [115].

Figure 58: Monotonically increasing-K stage II crack growth rates with respect to applied potential are plotted for C465-H900 in 0.6M NaCl at a $K=40\text{MPa}\sqrt{\text{m}}$. Reproduced from Pioszak 2013 [115] .

Figure 59: Ripple loading protocol and its potential effect on K_{ISCC} is visually represented. The small cyclic load superimposed over constant monotonic tension seen in (a) effectively reduces K_{ISCC} in many materials shown schematically in (b) [158].

Figure 60: This plot summarizes sub-threshold crack growth in different environments at different loading parameters. Testing was conducted in accordance to increasing and decreasing-K fatigue parameters at $f=2$ and the applied potential of $-200\text{mV}_{\text{SCE}}$. Further conditions specific to individual tests are noted in the legend.

Figure 61: Micrographs show different fracture modes in Phase I testing. Mixed fracture modes in (a) are observed at an $R=0.5$, an $f=2$, and a nominal stress of 300MPa in a 3.0M NaCl solution polarized to $-200\text{mV}_{\text{SCE}}$.subject to the increasing-K loading protocol (b) shows tests conducted at a K_{max} of $55\text{MPa}\sqrt{\text{m}}$ in 3.0M NaCl polarized to $-200\text{mV}_{\text{SCE}}$ subject to a $\Delta K=1\text{MPa}\sqrt{\text{m}}$.

Figure 62: This plot is an abridged version of the Phase I decreasing-K data in order to show the unusual crack growth behavior induced by the chloride-free water environment. All fatigue is conducted at $f=2$, a K_{max} of $55\text{MPa}\sqrt{\text{m}}$, and a decreasing ΔK to either threshold or failure.

Figure 63: Fracture surface taken from the DI water test fatigued in accordance to increasing and decreasing-K protocol at the OCP. The red arrow indicated direction of crack propagation.

Figure 64: Other research has also reported unusually rapid SCC-induced stage II crack growth behavior in a chloride-free water environment. Reproduced from Kalnaus 2011 [146].

Nomenclature

f – Loading frequency

R- Stress Ratio ($\sigma_{\min}/\sigma_{\max}$)

K – Stress intensity

K_{IC} – Plane strain fracture toughness

K_{\max} – Maximum stress intensity

K_{TH-SCC} – Stress corrosion cracking threshold stress intensity

ΔK – Stress intensity range

N_{pit} – Pit formation cycles

N_i – Crack formation cycles to $\approx 5\mu m$

$N_{p-small}$ – Small crack propagation cycles to failure

N_p – Long crack propagation cycles to failure

N_f – Total cycles to failure ($N_{pit} + N_i + N_{p-small} + N_p$)

σ_{\max} – Maximum applied-uniform tensile stress

σ_{\min} – Minimum applied-uniform tensile stress

η_H – Crack tip overpotential for hydrogen evolution

ΔK_{eff} – Effective ΔK accounting for closure effects

[Cl⁻] – Aqueous chloride concentration

1 Introduction

Ensuring structural integrity of highly stressed aerospace components operating in corrosive environments requires an engineering approach grounded in precise understanding of mechanisms governing environment-cyclic strain assisted localized corrosion, crack formation, and crack growth. Steels contribute 7-20% of commercial and military aircraft weight [1, 2] and are implemented for applications requiring high strength (e.g. aircraft landing gear, torque tubes, arresting hooks, engine attachments, etc.). By mass, a state-of-the-art aircraft (such as the Boeing 787) is approximately 10% steel despite significant use of advanced composites [3]. Aqueous chloride environments are pertinent to air frame operation in sea-coast and marine environments where a component is either fully immersed or where sea-salt aerosol contaminants (with NaCl as a major component [4]) result in a wetted surface under ambient humidity [5]. As such, evaluating the influence of aqueous chloride environments on fatigue performance of high strength steel is essential to the design and structural integrity management of critical airframe components. In this study, fatigue characteristics of the ultra-high strength stainless steel (UHSSS) Custom 465 (C465) are studied by gathering crack growth and fatigue limit data across different full immersion NaCl concentrations ($[Cl^-]$).

Modern precipitation-hardened martensitic UHSSS are often selected for aerospace structural applications as they exhibit desirable combinations of strength, fracture toughness, and corrosion resistance. Some endurance limit (S-N) research has been performed on this material class [6-10] demonstrating the deleterious effect of $[Cl^-]$ on fatigue life (Figure 1), however, specific information describing the effects $[Cl^-]$ on different stages of corrosion fatigue failure phenomena in UHSSS is lacking. Incorporation of the loading environment into fatigue life predictions models is a critical aspect of next-generation structural integrity efforts and future component design. [11-16]. Fatigue life modeling efforts require (1) quantification of pit formation times, (2) an understanding and empirically based modeling of the cycles required to form a crack from a pit (note that linear elastic fracture mechanics (LEFM) models do not predict crack formation life), (3) an accurate prediction of crack propagation life based on crack growth kinetics specific to the operational environment. Understanding these points will elucidate how environmental-fatigue behavior depends on mechanical and electrochemical parameters. The purpose of this study is to better understand the corrosion-

fatigue interaction in UHSSS to better inform predictive models on the effect of chloride concentration on fatigue life in UHSSS Custom 465.

1.1 Background of Aerospace Steels

Ultra high strength steels (UHSS), such as 4340 and 300M, are widely used for aerospace structural components due to their high strengths. These low alloy martensitic steels derived strength and toughness from an unrecovered dislocation structure and various precipitated carbides derived from the first stage temper [17]. Though extremely strong, these steels are highly susceptible to environmental degradation and stress corrosion cracking (SCC). While they exhibit a plane strain fracture toughness (K_{IC}) of $71\text{MPa}\sqrt{\text{m}}$, the threshold stress intensity value for the onset of SCC (K_{ISCC}) measures considerably lower, ranging from 11-16 $\text{MPa}\sqrt{\text{m}}$. To improve fracture toughness, next generation UHSS featured higher proportions of nickel (8-10%) and cobalt (4-14%) in addition to other minor alloying elements (Cr, Mo). These additions increase the driving force for the formation of MC-carbides [18] on tempering, which not only serve as a strengthening mechanism but also delay dislocation recovery. These Ni/Co rich steels, most prominently AF1410 and AerMet100, are about as tough and strong as 300M but possess greater SCC resistance, as their K_{ISCC} ranges from 45-71 $\text{MPa}\sqrt{\text{m}}$ [17]. The compositions and properties of common aerospace steels are shown in Table 1 and Table 2.

Despite having good mechanical properties and reasonable SCC resistance, AerMet100 and other UHSS are expensive due to their alloying elements, and they are still susceptible to broad surface corrosion that can serve as fatigue damage nucleation sites. In order to protect these metals from corrosive environments and extend service life, hazardous coatings and platings containing cadmium, nickel, and/or chromium are used as a corrosion-resistant barrier [19, 20]. Efforts continue to develop and improve coating/plating materials [20, 21]. While such coatings are typically effective in countering environmental damage, the cost, hazards, and reliability issues posed by these coatings remain a challenge. Furthermore, detecting a discontinuity in a coating (and corresponding sub-coating) and stress corrosion cracking or corrosion fatigue events beneath the coating is challenging. The environmental and safety issues associated with the coatings coupled with inextricable inspection challenges motivate the development of high strength steels that are inherently resistant to degradation in the operational environment.

The shortcomings of UHSS created a demand for less expensive, highly corrosion resistant steels with comparable mechanical properties to incumbent UHSS. This demand prompted the development of UHSSS using 300M as a starting point in which chromium, nickel, and molybdenum are primary alloying elements with occasional trace additions of titanium, manganese, vanadium, and aluminum. These alloying additions generally serve to reduce corrosion susceptibility, reduce intergranular (IG) corrosion in welded materials, and improve mechanical properties [22, 23]. In particular, molybdenum and chromium work symbiotically to improve corrosion resistance by promoting the formation of a passive oxide film as it does in other stainless steels such as 304 and 316 [24, 25]. Due to the addition of chromium, these steels must be as free of carbon as possible as carbon will promote formation of Cr_{23}C_6 , rendering corrosion-resistant effects of alloyed chromium additions less effective [26]. Furthermore, carbon is a δ -ferrite stabilizer and must be minimized to ensure a fully-austenitic microstructure prior to quenching as ferrite will degrade mechanical properties [22]. Without carbon, M_2C and other carbides cannot form, eliminating a vital strengthening mechanism for UHSS alloys. Instead, in addition to unrecovered martensite, UHSSS alloys derive strength from a final precipitation hardening step in which nanoscale precipitates form [17, 22, 27, 28]. Not only do these precipitates improve toughness, but they can also trap hydrogen. In some instances this has been shown to slow sub-critical crack growth by reducing HE effects much like carbides do in UHSS alloys. Though not quite as tough as some UHSS, UHSSS may be employed uncoated due to their combination of mechanical properties and corrosion resistance.

There are several UHSSS currently in service throughout the aviation industry. These include, but are not limited to 17-4PH, 15-5PH, Custom 450, 13-8Mo Custom 455 and Custom 465 as well as next generation developmental alloys such as Ferrium S53, MLX17, and high nitrogen stainless steels [17, 29]. Due to its desirable combination of strength, toughness and corrosion resistance and current use in aviation, medicine and energy, C465 in the H950 aging condition was chosen for this research [30, 31].

1.2 Goals

Multiple sources report highly deleterious effects of aqueous chloride environments on the fatigue life of precipitation-hardened UHSSS despite their stainless nature [6, 7, 32, 33]. Figure 1 includes one such report showing that fatigue life can decrease by an order of

magnitude or more as the aqueous chloride fatigue environment increases in $[Cl^-]$ from 0.0006M to 3.0M. However, these reports do not further investigate specific causes of this observed trend. The study presented here will investigate the effect of chloride concentration on the corrosion fatigue behavior of C465-H950. The total fatigue life (N_f) of a metal cycled in an aggressive aqueous environment can be represented as the sum of four regimes, such that:

$$N_f = (N_{pit}) + N_i + N_{p-small} + N_p \quad (1)$$

Where:

N_f = total fatigue life

N_{pit} = the time (t) required for a crack-initiating corrosion pit to form times the loading frequency (f)

N_i = the number of cycles to initiate a crack (from either a pit or other formation feature)

$N_{p-small}$ = the number of cycles in the “chemically small” cracking regime

N_p = the number of cycles of long crack growth

Accurate and efficient modeling of the corrosion fatigue behavior requires (1) quantification and understanding of the influence of the aggressive environment on the controlling mechanisms in each regime and (2) identification of the regime that is most influenced by the environment so that modeling efforts are properly apportioned. The model above is only rigorously applicable to loading of a pristine specimen in an aggressive environment such that the dissolution occurs concurrent with loading resulting in a complex interaction of and N_i . Specifically, the size/morphology of the pit will change with time and the N_i will be critically dependent on the size/morphology of the pit. Both concurrent loading and dissolution of a pristine specimen as well as pre-pitting then loading in an aggressive solution are considered in this work.

In both cases, N_i will be defined as the cycles required to form a crack of fixed size ($a=1-25\mu\text{m}$) from the nucleation site, enabling a consistent quantification of crack formation. Extensive study has been performed to understand deviations of small crack growth rate behavior from that observed for long cracks. Despite minor discrepancies in literature, small crack phenomena are categorized into four groups (1) mechanically small cracks where the crack

length a is less than the plastic zone size, (2) microstructurally small cracks where a is less than the critical microstructural dimension, oftentimes defined as grain size, (2) physically small cracks where a is on order 5-10x the grain size or around 1 mm), and (4) chemically small cracks where a is 5-10 mm [34-36]. Characterization and analysis of $N_{p\text{-small}}$ will provide sub-millimeter crack growth rates starting at the initiation point, elucidating any effects that chloride concentration, local microstructure, and initiation feature may exert on short crack growth. It may also provide information on electrochemical processes and local chemistry at the crack tip at different depths, helping to define the extent of crack tip solution occlusion from the bulk solution. [36]. In the N_p regime, the crack is long compared to microstructural features and interacts with the material on a continuum scale; from a chemical perspective crack tip occlusion likely occurs where the chemistry at the crack tip differs significantly from the bulk solution. Measurement of N_p will show the effects of chloride concentration on long crack growth kinetics, and fracture surface characterization will inform mechanistic interpretation.

With this background, the current research has four goals that in total will aim to characterize and help to explain the effects of chloride concentration on each aforementioned individual corrosion fatigue crack growth regime in C465-H950:

Goal 1: Study pitting characteristics of C465-H950 at open circuit and anodic polarizations to develop controlled, repeatable pitting protocols. These protocols are then used in tests to evaluate the effect of corrosion damage on fatigue behavior.

Goal 2: Characterize fatigue crack formation location with respect to various corrosion-induced initiation features and investigate links between surface morphology, crack nucleation behavior, and fatigue life.

Goal 3: Quantitatively assess the deleterious effect of $[Cl^-]$ on the overall fatigue life of pre-corroded specimens of C465-H950.

Goal 4: Quantitatively assess crack formation, small crack growth and long crack growth in the context of S-N behavior of pre-corroded specimens to identify the corrosion fatigue regime(s) most severely affected by $[Cl^-]$.

1.2.1 Background

1.2.1.1 Pitting in Stainless Steel

Pitting corrosion behavior has been extensively studied in stainless steels [37-44]. Of the literature, the work performed on low chromium martensitic steels exposed to chloride environments is of particular interest [33, 45]. Stainless steels are protected by naturally forming a very thin, very stable passive (oxide-covered) surface film about 1nm thick, acting as a barrier between the base metal and the elements [23, 46]. Aggressive environments may cause local rupture of the passive film, initiating a sporadic, stochastic pitting process. The majority of pitting events in stainless steels are in the proximity of second phase particles, most notably at magnesium sulfide (MnS) inclusions [47, 48]. MnS particles are common in many stainless steels and are known to produce chromium-depleted zones adjacent to the pit as a result of processing. These depleted zones are particularly susceptible to high-rate dissolution which leads to pitting [43].

Some stainless steels are susceptible to pitting in aqueous solutions containing as little as 1mM chloride. While passive current densities for steel dissolution are typically on the order of nanoamperes per square centimeter. Active pitting processes are subject to distinctly different local environments within the pit which can reach 1M [Cl⁻], low pH, and dissolution current densities on the order of 1amp/cm². Figure 2 shows a diagram of an autocatalytic pit growth process. Studies have indicated that there is a critical current density as a function of pit depth that must be exceeded for pit growth to continue, though the application of this model to stainless steel is controversial due to [Cl⁻] possibly dominating pH as a driving force [39, 40]. The environment within the pit (or crevice/crack) is a result of the dissolution and hydrolysis of the base metal, represented by the following equation



This reaction acidifies the environment within the pit increasing the diffusion of chloride ions into the pit to maintain charge neutrality [43].

Pitting phenomenology is not drastically different in precipitation-hardened martensitic UHSSS than in other stainless steels. Pit growth mechanisms based on ionic and mass transport

are governed by well-defined growth models; as such, metal dissolution and hydrolysis phenomena are theoretically the same as in older stainless steels [37, 39, 40]. However, processing techniques associated with the manufacture of these UHSSS can produce microstructures and phase compositions markedly unique from non-stainless legacy steels. While aging treatments are essential for precipitation-hardening reactions, non-ideal tempering will affect the austenite:martensite ratio of the material not only decreasing strength but also decreasing pitting resistance, as Syrett observed in PH 17-4 [32]. Overaging may lead to the precipitation of chromium-depleting inclusions, most notably $M_{23}C_6$ particles, which can increase susceptibility to corrosion damage [8]. Hochanadel's studies reveal aluminum and sulfur inclusions present in PH 13-8Mo and the formation of $M_{23}C_6$ inclusions along δ -ferrite/martensite boundaries[28] all of which lead to favorable pitting conditions.

Work as also been performed to analyze the effect of inclusions, particularly manganese sulfide (MnS), on the size of pits. The dissolution of MnS inclusions, common in many carbon and stainless steels, has been shown to be the first stage of pit formation in several studies (Figure 3) [47-52]. Ke independently observed small pits of radius 0.75-3.5 μ m at MnS inclusions in 304 steel after various anodic polarizations [53]. Baker observes similar pitting phenomena in similar 18.6Cr-9.7Ni-2.3Mo stainless steel [49]. Work performed by Ernst in 304 foils produced very large pits, about 50 μ m in depth over 100 μ m in radius, after just a few minutes in aggressive solution at a highly anodic potential [37]. Turnbull's environmental fatigue studies of a 3NiCrMoV steam turbine disc steel reveal substantial pits up to 250 μ m in diameter in service conditions simulated by exposure to an aggressive condensate and a service stress 90% of the yield strength [54].

Little research on the pitting characteristics specific to C465 has been performed, but previous work on similar alloy systems can be used to predict what features or microstructural characteristics will promote pitting and eventually form a fatigue crack. Many of these steels derive strength from the formation of nanoscale intermetallic phases comprised of titanium, aluminum, and/or nickel. Metallic carbides are also often observed as strengtheners even in low carbon grades of steel [18, 55, 56]. MCs fall into one of two categories by size, (1) large 1-10 μ m particles formed during solidification which are ineffective strengthening agents, and (2) fine

strengthening precipitates on the order of 5nm to 500nm [57, 58]. Larger inclusions may serve as favorable pitting sites as per earlier discussion.

It is reasonable to expect similar behavior in C465-H950. Despite low manganese and extremely low sulfur compositions, MnS will likely form and could reasonably form pits initiating corrosion fatigue cracks. Other large, metallic inclusions may also play a role in this study. Even though carbon content is kept very low to prevent chromium segregation, metallic carbides will likely form. Their size scale is unknown, so they could manifest as either a nanoscale strengthening dispersion or as large particles consuming significant quantities of other alloying elements most likely to be chromium but may instead consume nickel and/or titanium. Large inclusions less soluble than MnS may also serve as favorable sites for pitting attack [47].

C465 also contains an unusually low amount of chromium for a stainless steel. By chromium content alone, it is expected that C465 will still be more corrosion resistant than legacy UHSSs but will likely perform poorly compared to other modern UHSSs of significantly higher chromium content. The addition of molybdenum will almost certainly improve corrosion resistance, as the symbiotic effects of molybdenum and chromium have been observed in other research [59]. The hypothetical pitting resistance equivalent number (PREN) is an attempt to correlate pitting corrosion resistance of stainless steels to their chemical compositions [60, 61]. In general, higher chromium, molybdenum, and nitrogen content will increase PREN and thus be less likely to pit. By PREN alone, C465 is expected to exhibit poorer corrosion resistance than other similar UHSSS. However, this metric does not account for the minor corrosion resistant properties of nickel and titanium, nor does it factor the deleterious effects of additions such as manganese, sulfur, and phosphorus, the latter series of which is nearly absent from C465. The purity of this vacuum induction melted-vacuum arc remelted (VIM-VAR) steel may improve its corrosion resistance and offset the relative lack of chromium and molybdenum.

The influence of the environment on corrosion and pitting in steel is critical to understand the crack formation behavior of C465. This study pertains directly to the effects of $[Cl^-]$ on corrosion fatigue behavior, it is important to understand how $[Cl^-]$ effects pitting which is a critical component of overall fatigue life. It is well known that chloride is extremely deleterious to the structural integrity of steels due to its propensity to encourage pitting [38, 62] and

accelerate crack propagation kinetics [63, 64]. Although pit chemistry is distinct from the bulk due to autocatalytic pitting processes, bulk $[Cl^-]$ has been shown to be critical to pitting mechanisms. Lowering bulk $[Cl^-]$ has been shown to alter pit shape and potentially encourage pit repassivation. However, bulk $[Cl^-]$ also doesn't appear to have a strong impact on pit growth rate, as Ernst shows that pit growth varies with the square root of time, regardless of bulk $[Cl^-]$. Models put forth by Kondo suggests that pit size is approximately proportional to the cube root of time [65], though this does not account for different environments. Both findings agree with Muto's work showing that pit growth kinetics are dependent on both material and environmental parameters [66]. This suggests that growth kinetics are on average dictated by diffusion control even though pitting mechanisms may vary with bulk $[Cl^-]$ [38]. For thin film electrolytes, maximum pit depths in 304L, 316L, Custom 465, and AerMet100 have been modeled by Shedd and vary based on salt loading density (governing film thickness) and relative humidity (governing $[Cl^-]$). Maximum pit sizes range from 30-380 μm depending on environmental conditions [67]. Pits observed immersed in marine environments in 410, 302, 316, and 321 stainless steels average about 60 μm in depths after just one year of service [68]. Work performed by Leckie shows that the critical potential for pitting in 18-8 steel shifts to more active values as $[Cl^-]$ increases [69]. Similar phenomena is observed by Schaller in C465 [70] and will also likely play a part in pitting corrosion processes in this study. In review, literature suggests that bulk $[Cl^-]$ will strongly influence pit depth, but it may also strongly affect pit morphologies and the corrosion potential.

1.2.1.2 Crack Initiation

The number of cycles required to form a crack is strongly dependent on the material, surface conditions (scratched, roughness, corrosion, etc.) and loading parameters. Former research gathered experimental initiation life data on UHSS under some corrosive conditions [71], but the effect of environmental chloride concentration on initiation life of a UHSSS has not been thoroughly studied.

Aqueous chlorides are known to degrade fatigue performance in UHSSS by inducing corrosion damage which can act as a greater stress concentrator than secondary phase particles and inclusions in the metal matrix. Former work has predicted the effects of corrosion damage shape and morphology via fracture mechanics, but these models are based largely on long crack

growth rates which are not affected by the local grain-scale plasticity factors relevant to crack nucleation and microstructurally small crack growth [65]. A comprehensive study to determine the influence of environmental variables on the pit-to-crack transition mechanism is lacking. This information will elucidate the role of environment and corrosion damage size and morphology on the initiation life which will improve accuracy of structural management, either by safe life and damage tolerance models.

Former studies coupling the effects of fatigue loading parameters and environmentally induced damage on the pit-to-crack transition have been conducted in Al-Zn-Mg alloys and AF1410 steel [71, 72]. Such methodology extensively quantifies crack formation mechanisms and subsequent fatigue life prediction models. A similar technique will be implemented here to analyze UHSSS-specific crack initiation behavior and its effect on fatigue performance in various environments. Imparting large crack-initiating corrosion features (pits) allows for characterization of pit morphology and surface character intrinsic to C465, and microstructural and corrosion features responsible for initiation will be precisely quantified. Introducing a corrosive environment will further elucidate corrosion fatigue crack initiation processes. It is well known that actively corroding pits create an aggressive local environment within the pit which could strongly influence crack nucleation life and location [54, 73, 74].

Understanding the role of natural pitting processes in UHSSS in the context of the pit-to-crack transition is also important for accurate environmental fatigue initiation life in service environments. The previous section touches on work performed on corrosion behavior of similar and legacy steels, but few studies examine the precise effects of mechanical loading on crack initiation in an aggressive environment. A better understanding of crack nucleation arising from an actively corroding pit will improve understanding of initiation not just as a function of mechanical stress concentration but also as a function of environment. As the pit actively corrodes and grows, the increasingly aggressive environment may increase the propensity for crack initiation. A more occluded, acidic environment is detrimental to the protective passive film, which would facilitate an increase of hydrogen available to diffuse into the microstructure, degrading mechanical properties and encouraging crack formation.

Even if pits were not in an active corrosion state, bulk $[Cl^-]$ may still have a role in crack nucleation and growth characteristics. Higher $[Cl^-]$ solutions may decrease N_i as they are known

to be deleterious to passive film resilience. Environmental effects on crack nucleation from pre-corroded pits may be more readily observed than in cracks nucleating from a smooth, polished surface. The passive layer within a pit may be more discontinuous, especially under tensile stress leading to amplified local strains due to pit roughness. These considerations would increase solution contact with the base metal, promoting crack formation. Thus, crack formation from pre-corroded pits (not actively dissolving) may show a higher dependence on bulk $[Cl^-]$ than formation from smooth, pristine samples.

Researchers have proposed engineering scale pit-to-crack transition models that consist of (1) corrosion pit growth (discussed in previous section) and (2) achieving a critical pit condition at which point a crack nucleates from the corrosion pit. Kondo proposes that critical size of the pit is given by that observed in failure analysis, suggesting that pit growth stops upon crack initiation, at which point the anodic region becomes the crack tip. At this point and stress conditions, fatigue crack growth rate exceeds pit growth rate, and a crack is nucleated. Critical pit size varies inversely with applied stress [65]. A critical assumption of this model is that a two-dimensional stress intensity solution calculated using the Newman-Raju semi-elliptical surface crack formula is applicable to a three-dimensional pit if the fracture surface cross-sectional dimensions are used. Additionally, this approach suggests that long crack growth kinetics associated with this calculated stress intensity range are pertinent for comparison to the rate of corrosion damage. Though these assumptions are clearly not rigorous, this approach can be useful for some engineering scale problems. Regardless, such an approach does not investigate the environmental effect on short crack growth and ignores microplasticity at the crack tip.

A comprehensive study accounting for all corrosion-induced mechanical stress concentration factors in UHSSS and their interaction with various chloride levels has not been performed. This research will take a closer look at corrosion morphology of the crack nucleation site in the presence of various $[Cl^-]$ environments. This will inform modeling efforts to precisely predict crack initiation life in UHSSS in a variety of service-like conditions.

1.2.1.3 Crack Growth

The total crack growth rate (da/dN) for environment assisted fatigue crack propagation (EFCP) is traditionally taken as the sum of three growth rate components [75-79]: (1) inert-

environment plasticity dominated crack growth progression that is independent of frequency, (2) time-cycle dependent cracking (da/dN_{CF}) governed by the accumulation of crack tip cyclic plastic strain, local tensile stress, and H concentration, and (3) “static load” environmental cracking (da/dN_{SCC}) at stress intensity levels during load cycle which are above the a threshold for monotonic load time-dependent cracking (K_{ISCC}). Cyclic loading, even at high R (>0.9) and well below the threshold cyclic stress intensity range (ΔK_{th}), have been shown enhance the time-dependent cracking component and lower the apparent K_{ISCC} [80-84]; proposed superposition-based modeling of da/dN must account for such complexities [85]. Contributions of both (2) and (3) have been widely reported for a range of steels and aggressive environments; this behavior is generally understood via a hydrogen environment embrittlement (HEE) mechanism [86-89]. Limited characterization of the EFCP behavior of precipitation hardened martensitic stainless steels has demonstrated a deleterious effect of cyclic loading in aqueous chloride environments; this effect is enhanced for high strength tempers, elevated temperatures, and cathodic polarizations [7, 8, 10, 90, 91]. A systematic study of the effect of chloride concentration at low frequencies for modern-high purity precipitation hardened martensitic stainless steels is lacking.

Aqueous chloride environments are pertinent to sea-coast and marine environments where a component is either fully immersed or where sea-salt aerosol contaminants (with NaCl as a major component [4]) result in a wetted surface under ambient humidity [5]. The thickness and composition (i.e. chloride concentration) of the deliquesced electrolyte film will be dependent on the salt loading density and relative humidity [92]. A broad literature has identified the phenomenological distinctions (and to a lesser extent the mechanistic distinctions [93-96]) between full immersion and thin-film atmospheric corrosion behavior [4, 93, 97]. For a constant chloride concentration and pH, EFCP behavior in a thin-film electrolyte may deviate from full immersion due to differences in the pertinent mass transport distances and/or local ionic resistance influencing the cathodic/anodic reaction kinetics that the control crack tip H production [64]. The EFCP behavior under thin-film conditions has not been studied outside of limited testing of an Al-Cu-Li alloy that suggested a secondary influence on crack growth kinetics [98]. This suggests that the influence of the varying thin film chloride concentrations (arising from different salt-loading densities and humidities) can be reasonably initially be studied via full immersion testing.

It is well known that saltwater, marine and hydrogen-containing environments lead to accelerated crack growth rates, and sub-threshold fatigue cracking [99, 100]. Low alloy steels fatigued in chloride solutions have been observed to crack at rates up to 500 times faster than in open air. [63] A number of stainless steels, such as Custom 450, 4340, 444, X52, X100, SUS410JI [7, 8, 64, 101, 102] also show enhanced crack growth rates when fatigued in aqueous chloride and hydrogen containing environments. Though generally erratic, short crack growth fatigue growth has been shown to occur and propagate in 3.5% NaCl environments below long crack propagation threshold values. The same tests run in air demonstrate crack arrest, suggesting that the environment plays a strong role in the crack tip damage process [35, 36, 103].

The HEE mechanism proposes that fatigue crack advance in aggressive environments is enhanced by the interaction of localized cyclic plasticity, tensile stress, and absorbed atomic H in the fracture process zone [64]; the fundamental details of this interaction are controversial [104, 105]. In aqueous environments, electrochemical conditions (pH and electrochemical potential) govern the overpotential (η_H) for hydrogen (H) production which determines available atomic H for adsorption. Of particular interest are the electrochemical conditions at the crack tip where active straining can rupture the local passive film and where there are short H diffusion distances to the highly stressed fatigue process zone [106]. For a wide range of high strength steel compositions in aqueous environments, researchers have demonstrated that the occluded crack tip environment deviates substantially from the bulk and is conducive to H-production [107]. Specifically, low alloy steels typically have a crack tip pH of 3.5-4 due to dissolution of ferrous ions. For stainless steels, hydrolysis of Cr^{3+} will dominate and further reduce the pH to near 1 [107-110]. A modest potential drop from the bulk surface to the crack tip has also been reported due to increased resistivity through the narrow crack wake channel [110]. Due to the need to maintain electroneutrality, this acidification process requires and results in a high anion concentration (e.g. Cl^-) at the crack tip [111], shown schematically in Figure 4. This enhanced chloride concentration exacerbates the hydrogen environment embrittlement cracking (HEAC) process by destabilizing the crack tip passive film and enhancing the H-activity. Researchers have shown that even extremely low bulk anion concentrations can support the crack tip acidification process; as demonstrated for chloride concentrations below 10^{-6} M and distilled water due to trace impurities or dissolved alloy constituents [89, 111]. These occluded crack tip conditions enhance the η_H and couple with active straining to destabilize and rupture the crack

tip passive film and enable the HEAC process. The development of an aggressive crack chemistry is also a function of the crack geometry and loading conditions [36]; a systematic study of the effect of chloride concentration on the corrosion fatigue crack progression from small to long cracking is lacking.

Crack size and geometry is critically important to the development of an occluded environment which links crack size to the chemical driving force for corrosion fatigue [63, 112, 113]. As previously discussed, it is useful here to distinguish between chemically short and long cracks as small cracks are not adequately described by conventional fracture mechanics due to mechanical, metallurgical, and chemical considerations, causing a breakdown in similitude for these short cracks [63]. Small cracks up to 5mm in length have been observed growing at faster rates than predicted by long crack fatigue mechanics, oftentimes below threshold conditions. Ritchie and Lankford posit four regimes of small fatigue crack growth which are all distinctly different from long crack growth: mechanically small, microstructurally small, physically small, and chemically small. The first three span the fatigue crack up to 0.5-1mm. Mechanically small cracks are on the order of a grain size, and growth is strongly dictated by plasticity in the initiating grain, resulting in highly variable crack growth kinetics. Microstructurally small crack growth kinetics are governed by crack tip shielding and crack shape, which are strongly influenced by the local microstructure since the crack front does not include many grains. Physically small cracks extend up to 1mm in which crack tip closure becomes a factor and the effective ΔK (ΔK_{eff}) better defines the driving force. Chemically small cracks extend up to about 10mm (depending on material and environment) during which crack length dependent local crack tip environment plays a critical role. Chemically small cracks may propagate at rates a few orders of magnitude greater than long cracks subject to the same driving force [63]. This is largely due to crack tip environment conditions which induce electrochemical phenomena that can promote hydrogen embrittlement and enhance passive film-rupture dissolution mechanisms. Such crack tip solution chemistries have been investigated by various methods, such as freezing the solution for analysis or microelectrode characterization [74, 114] of electrochemical parameters right at the crack tip. Beyond a certain crack depth, a steady-state environment is typically observed, which enables the reasonable use of similitude concepts for a given stress intensity and environment. This study is not intended to directly quantify the crack tip environment as others have done. Rather, results will be comparatively analyzed with respect to

different crack sizes and bulk environments to better understand the effect of bulk [Cl⁻] on small crack growth kinetics.

Specifically, this work will characterize the fatigue crack growth behavior of Custom 465 using a single edge notched (SEN) specimen at a constant stress ratio ($R = K_{\min}/K_{\max}$) under both rising and falling stress intensity range (ΔK) protocols. Testing environments will range from flowing distilled water and NaCl solutions ranging from 0.0006 to 3.0M polarized to various potentials. Crack growth rates data and fractographic analysis will quantify the effect of bulk chloride concentration on the crack progression and will inform mechanistic interpretation. Furthermore, the relative contribution of time-cycle dependent and “static load” cracking will be evaluated.

2 Experimental

Specimens were machined from a $\frac{3}{4}$ ” (19.05mm) diameter bar of Custom 465 and heat treated in the H950 condition with a composition detailed in Table 3. The monotonic tensile yield strength (σ_{ys}) and the ultimate tensile strength (σ_{UTS}) is 1648 MPa and 1765 MPa respectively, and a plain strain fracture toughness (K_{IC}) of 95 MPa \sqrt{m} , as reported by the manufacturer [30], seen in Table 4 . The tensile and ultimate strengths were independently confirmed to be 1827MPa (compressive). The threshold for stress corrosion cracking for C465-H950 at -550mV_{SCC} was reported to be greater than 90MPa \sqrt{m} as quantified by using a slow-rising displacement fracture mechanics based test [115].

Mechanical properties of C465-H950 approach the values required for UHSSS applications while maintaining acceptable fracture toughness values [29]. Oxidation resistance is achieved by the addition of 12% chromium, allowing for the formation of a continuous Cr₂O₃-based passive protective film. This double vacuum melted alloy is characterized by a single phase martensitic matrix with unrecovered dislocation structure contained in prior austenite grains with an average size of 50-80 μ m. EBSD analysis confirmed less than 1% retained austenite at the H900 treatment[115]; a similar fraction is expected at the H950 temper. Aging enhances fracture toughness and hydrogen embrittlement resistance by introducing a secondary phase nanoscale strengthening dispersion of coherent needle-shaped ω -phase possessing a

hexagonal crystal structure. Aging also causes a small fraction of austenite reversion along all interfaces (e.g. grain and lath boundaries) [116, 117]. Upon overaging, an incoherent, orthorhombic plate-like $\text{Ni}_3(\text{Ti},\text{Mo})$ precipitates, further increasing fracture toughness and SCC resistance at the expense of strength [30, 118, 119]. Limited literature confirms the presence MoC precipitates as well [99]. Figure 5 and Figure 6 show SEM and EBSD micrographs of polished C465 in the H950 condition.

In order to fully characterize each corrosion fatigue regime with high precision, research was conducted in two phases each with its own specimen design and procedure. Phase I was designed to investigate the effect of chloride concentration on long crack growth kinetics. These data will be used for isolated fatigue life modeling predictions. Phase II was designed to characterize the effect of chloride concentration on crack initiation characteristics and microstructure, initiation life, and small crack growth.

2.1 Phase I

Phase I experimentation will address Goals 1 and 4 by providing long crack growth rates as a function of $[\text{Cl}^-]$. Single-edge notch (SEN) specimens with threaded ends were machined with the rectangular reduced gauge section of width $10.16 \pm 0.127 \text{ mm}$, and thickness of $2.67 \pm 0.05 \text{ mm}$, and a length of $35.0 \pm 0.5 \text{ mm}$, detailed in Figure 7. Figure 8 shows the square notch, $0.508 \pm 0.03 \text{ mm}$ deep and $0.508 \pm 0.03 \text{ mm}$ wide, machined at the center of the reduced gauge via a slow-grind final machining process in order to avoid residual stresses and surface layer melting which could influence localized corrosion behavior [41, 52, 120, 121]. The notch morphology was initially designed in an attempt at rough-scale characterization of the influence of $[\text{Cl}^-]$ on crack formation like and potential corrosion damage of the notch surface. However, such subtle effects were overwhelmed by variable machining quality. Each SEN specimen polished with 600 grit SiC grinding paper except for the notch.

Fatigue crack initiation and propagation was studied in various environments, specifically in high humidity ($\text{RH} > 90\%$) nitrogen, in distilled water, and in aqueous 3.0, 1.5, 0.6, 0.06, 0.006, 0.0006 M NaCl solutions. Solutions were prepared using Millipore high purity deionized (DI) water (Resistivity = $18.2 \text{ M}\Omega \text{ cm}$) and reagent-grade crystalline NaCl from Fisher Scientific and Sigma Aldrich. Aerated solution was pumped using a peristaltic pump from a 1 liter reservoir at a rate of 20 mL/min into a Plexiglas cell with a volume of 360 mL . The pH did not undergo a

substantial change in any test as a result of corrosion processes. Pre-test solution pH averaged 5.75 with a standard deviation of 0.34, and post-test solution pH averaged 5.68 with a standard deviation of 0.31. The specimens were electrically grounded through the MTS 810 servo-hydraulic test frame. The fully prepared Phase I test setup is shown in Figure 9.

The open circuit potential (OCP) for C465 as-annealed in 0.6M NaCl is -220mV versus the standard calomel electrode (mV_{SCE}). After 1 hour, OCP measurements in 0.05, 0.9, and 5.3 M NaCl solutions shows that the corresponding OCP is -150 , -220 , and $-300 \text{ mV}_{\text{SCE}}$, respectively [70]. Each specimen was subject to OCP measurement for one hour prior to fatigue, and a $-200\text{mV}_{\text{SCE}}$ polarization (slightly anodic to the OCP of $-220\text{mV}_{\text{SCE}}$ in 0.6 NaCl) was applied to the specimen (working electrode) for the duration of the test. An Accument standard calomel reference electrode was inserted into the environmental cell via a port in the lid of the cell. The specimen was surrounded by a platinum mesh ring serving as the counter electrode. The potentiostat was operated in floating ground mode as the test frame provided a sufficient ground.

Crack tip hydrogen production is proposed to be controlled by pH and local potential, as such to maintain consistency between different solutions and to eliminate the effect of time dependent OCP changes testing is conducted at a fixed potential ($-200\text{mV}_{\text{SCE}}$) near the OCP for 0.6M NaCl solution. While such consistency is necessary to decouple the effect of chloride concentration from the influence of potential, due to the variation of OCP with $[\text{Cl}^-]$ (-150 , -220 , and $-300\text{mV}_{\text{SCE}}$ after 1 hour for 0.05, 0.9, and 5.3 M NaCl solutions, respectively) the constant $-200\text{mV}_{\text{SCE}}$ value results in an anodic polarization (compared to OCP) at high $[\text{Cl}^-]$ and cathodic polarizations at low $[\text{Cl}^-]$. While cathodic polarizations can influence the crack tip chemistry, current values are likely insufficient to prohibit acidification of the crack tip in a 12% Cr alloy [73, 109]. However, even for an acidified crack tip, a substantial cathodic polarization could potentially transfer a sufficient portion of OH^- production from the counter electrode to the bulk surface, which could create a strong gradient of pH from low at the tip to high at the mouth. This behavior could result in the precipitation of corrosion products near the crack mouth due to changes in solubility with pH; such corrosion product was not observed suggesting little effect of chloride dependent OCP values. Isolated tests were also conducted at a cathodic $-550\text{mV}_{\text{SCE}}$ potential. All tests were conducted at room temperature.

Cyclic loading (following a sinusoidal waveform) was applied at a maximum stress of 300MPa, a stress ratio (alternatively $R = \sigma_{\min}/\sigma_{\max}$) of 0.5, and a frequency (f) of 2Hz. If a crack failed to initiate after 1 million cycles, the stress was increased by 50MPa. This process was repeated until initiation was achieved, and the stress level at which a crack was formed is noted when the data is presented. After crack formation, the ΔK increased with crack extension (at constant stress) up to 27.5MPa \sqrt{m} reaching a maximum stress intensity (K_{\max}) of 55MPa \sqrt{m} . Subsequently, a decreasing ΔK protocol with a constant K_{\max} of 55MPa \sqrt{m} was initiated and run until either a minimum da/dN of 10^{-8} mm/cycle or a ΔK of 2MPa \sqrt{m} was observed. These fatigue protocols are represented visually in Figure 10.

Fatigue crack growth was monitored with a direct current potential drop (dcPD) technique [122, 123] as resistance increases as the crack grows due to decreasing area and increasing plasticity. Active and reference 0.127mm alumel wires welded to the specimen symmetrically about the notch on the notched edge with a Miyachi Unitek spot welder, as seen in Figure 11. Each active wire was placed 0.50mm from the center of the notch, and each reference wire was placed 17.5mm from the center of the notch. The welded alumel leads were coated with a peelable butyl rubber stop off lacquer (Micro-Super XP 2000) to prevent corrosion at the leads. In order to produce an IR drop across the crack tip, a constant direct current of 4 amperes was passed through the specimen. Johnson's equation for single edge cracks (below) gives the real-time crack length, a , in a plate of finite width, W , based on the potential across the crack tip.

$$a = \left(\frac{2W}{\pi}\right) \cos^{-1} \left(\cosh \left(\frac{\pi L_p}{W} \right) \right) / \cosh \left(\frac{V}{V_n} \right) \cosh^{-1} \left(\frac{\cosh \left(\frac{\pi L_p}{W} \right)}{\cosh \left(\frac{\pi a_o}{W} \right)} \right) \quad (3)$$

a_o and a_n is the known crack or notch size respectively. The immediate potential, V , and the initial reference potential, V_n , are measured over the distance L_p across the centered notch. An active feedback loop to a software program enabled precise K-control fatigue experiments. Each dcPD reading is a group average of 20 PD cycles. Visual linear corrections were made to account for the fatigue pre-crack and final crack depth, and a secant computation was employed to analyze da/dN .

2.2 Phase II

Goals 2-3 will be addressed by testing pristine and corroded dog-bone specimens in aqueous solutions of the aforementioned chloride concentrations. This will provide high fidelity crack initiation life, characterize initiation features, and collect small crack growth rate data. Test specimens with fillets tangentially blended to the uniform test section were machined conforming to the guidelines specified in ASTM E466-07 [124]. Specimens were machined from cylindrical bar stock of C465 19.05mm in diameter. Each specimen was 145.3mm in height, and 3.18 ± 0.05 mm thick. The full width of each specimen is 13.46 ± 0.05 mm, and the reduced gauge width is 7.62 ± 0.05 mm. The specimen grip length was 40.6mm, and at least 17mm of the grip section was directly engaged by the grip to prevent slippage. All tangentially blended fillets are 76.2mm in radius. The reduced width section edges were machined to a radius of 0.381mm to avoid stress concentrators at the corners. Further specifications for Phase II specimen design are detailed in Figure 12. All specimens were polished to a 600 grit finish to achieve a surface area roughness average (root mean square height, S_q) below $0.15 \mu\text{m}$ measured via white light interferometry. In some instances various corrosion pretreatments were performed prior to testing.

2.2.1 Mechanical Loading Parameters

Constant amplitude uniaxial fatigue testing was performed in accordance to ASTM E467-07 [124] on an MTS 793 servo-hydraulic test frame. Bending calibrations were carried out in accordance to ASTM E1012-12 [125] which resulted in a maximum bending strain of 2.16% of the total applied strain, well below the 5% standard maximum deviation. Specimens were centered in Instron hydraulically actuated grips textured with 90° diamond serrated wedges. An image of a typical testing setup is shown in Figure 13. Cyclic loading (following a sinusoidal waveform) was applied at a maximum baseline stress ($\sigma_{\text{max}} = 1153 \text{MPa}$ or $70\% \sigma_{\text{YS}}$), $R=0.5$, and $f=2\text{Hz}$.

A programmed loading sequence generated resolvable marker bands on the fracture surface which were observed and measured via scanning electron microscopy (SEM) fractography [126]. Each test began with 1000 baseline cycles. After the initial fatigue segment, a marker band sequences was applied to mark the fracture surface to identify the crack front location at a specific number of cycles. These marker sequences were then alternated with

baseline crack growth sequences (typically 2000-3000 cycles) such that 10-15 marker bands were imparted on each fracture surface. The exact details of the marker sequence evolved during the program to maximize marker band clarity. Generally, the σ_{\max} for marker band sequences was 20%-40% lower than baseline σ_{\max} . A single sequence used to create a single marker-band consisted of 3 to 11 segments of 5-20 cycles at $R=0.1$ then 10-40 cycles at $R=0.5$. Ensuring that the maximum stress value was well below that of the baseline loading precluded plasticity-induced retardation. Typically, the marker band loads comprised only 10-15% of the overall fatigue life. Prior work suggestions that such loading protocols do not cause da/dN transients or drastically influence the total fatigue life [127-132].

2.2.2 Loading Environment

Constant amplitude loading was performed on specimens in various environments, specifically in high humidity (>90%) nitrogen and in unbuffered, aqueous 3.0, 1.5, 0.6, 0.06, 0.006, 0.0006M NaCl solutions with a fixed applied potential of -200mVsce. The pH did not undergo a substantial change in any test as a result of corrosion processes. Pre-test solution pH averaged 5.56 with a standard deviation of 0.22, and post-test solution pH averaged 5.43 with a standard deviation of 0.19. Solution preparation, reservoir size, flow rates, electrode type, and electrode placement are identical to those in Phase I. For aqueous [Cl⁻] testing, OCP was measured for an hour immediately upon submersion in solution prior to fatigue testing. After one hour, the potential was fixed at -200mV_{SCE} for all fatigue cycling with the exception of tests in humidified N₂ environments. The environmental cell holds 500mL of solution. No peristaltic pump or solution reservoir was used so as not to disturb any local chemistry changes associated with pitting that may developed. The specimens are anchored into the Plexiglas chamber via an O-ring compression mechanism, and they are electrically grounded through the frame.

2.2.3 Specimen Pre-Fatigue Exposure Condition

Four different pre-fatigue specimen conditions were used on the dog-bone specimens prior to fatigue testing. The basis for these preparation protocols is addressed in Section 3.1.2. Table 5 lists each test and its corresponding exposure condition. Condition 1 specimens were tested in their as polished (pristine) condition in humid N₂ (>95% humidity) to serve as a reference. For Condition 2, pristine specimens were masked with stop-off lacquer to expose a constant area of 2cm², then were installed into the hydraulic frame and environmental cell

containing 0.6-3.0M NaCl and held at $-200\text{mV}_{\text{SCE}}$. After a 24 hour exposure the cycling was began immediately. Similarly, for Condition 3, pristine specimens were masked with stop-off lacquer to expose a constant area of 2cm^2 , then were installed into the hydraulic frame and environmental cell containing 0.6-3.0M NaCl and held at a more anodic potential of 100-150 mV_{SCE} . After a 24 hour exposure the cycling was began immediately. The prior two protocols attempted to induce corrosion pitting then study the crack formation from a growing pit.

Lastly, Condition 4 specimens included four designer pits (approximately $170\mu\text{m}$ in width x $50\mu\text{m}$ in depth) which were galvanostatically imparted into each specimen in a separate corrosion cell. For consistency between pits, only a single pit was produced at a time. A $50\mu\text{m}$ hole was drilled through rubber electro-plating tape (3M-471) which was then placed at the center of the gauge length and 2mm from the edge of the specimen. XP 2000 lacquer was used to mask the remainder of the specimen. The specimen was submerged in a room-temperature corroding solution of 1.0M NaCl acidified with HCl to lower the pH to 3. A potentiostat supplied a constant direct current of 18mA for 20 minutes. Additional corroding solution was pumped with a peristaltic pump into the tape hole to remove the H_2 bubbles produced during the corrosion process. These bubbles would otherwise adhere to the surface and tape, eliminating solution contact with the surface. This process is repeated three additional times for each specimen such that each face incorporated 4 coplanar designer pits, two on each broad face, each roughly hemispherical pit being approximately $41\pm 9.9\mu\text{m}$ deep and $176.6\pm 21.7\mu\text{m}$ in diameter. An example of a pitted specimen is shown in Figure 14. These pits were ultrasonically bathed in acetone, methanol, and commercial oxide remover (Branson brand containing citric acid, ethoxylated nonylphenol, and aqueous ammonia) for 20 minutes each to remove surface oxides. Pits were characterized via SEM and white light interferometry, shown in Figure 15. The protective masking was then removed and the specimens were loaded into the environmental cell and submerged in environment of interest. A 1 hour OCP measurement was performed, after which the specimen was polarized to $-200\text{mV}_{\text{SCE}}$ for fatigue loading. These OCP measurements are included in Figure 16. OCP measured in this research is more positive than the expected OCP ($\approx -200\text{mV}_{\text{SCE}}$) based on measurements made by Schaller [70]. This is likely not due to pH as pH differs little between Condition 4 tests. The increase in OCP could be due to differences in surface preparation and measurement protocol. Schaller's measurements were conducted within

minutes of surface preparation, whereas the measurements for Condition 4 specimens were made after days and weeks. Greater elapsed time leads to a thicker passive film, increasing nobility and thus OCP. Furthermore, $[Cl^-]$ influences OCP, so orders of magnitude changes in $[Cl^-]$ could significantly impact OCP measurements. Lastly, the duration of OCP measurement may also play a role as Condition 4 OCP was measured for only an hour. As OCP varies with time, the relatively short 1 hour window may produce a different measurement than when measured for a substantially longer time.

All specimens were fatigued to final fracture, at which point the specimen was immediately removed from the cell and cleaned in an ultrasonic bath of acetone and methanol for 20 minutes each. If necessary, Branson oxide remover was used to remove corrosion product. Fracture surfaces and corrosion surfaces were characterized via SEM.

3 Results and Discussion

In Phase I, 13 tests were performed using SEN specimens to analyze fatigue crack growth kinetics, and in Phase II, 37 tests were performed using dog-bone specimens to precisely characterize initiation characteristics and small crack growth. Sufficient data was collected to inform the goals of this research specifically, to (1) study pitting characteristics and develop controlled, repeatable pitting protocols, (2) characterize fatigue crack formation location with respect to various corrosion-induced features (3) quantitatively assess the deleterious effect of $[Cl^-]$ on the overall fatigue life of pre-corroded specimens of C465-H950, and (4) quantitatively assess crack formation, small crack growth and long crack growth in the context of Condition 4 S-N behavior to identify the corrosion fatigue regime(s) most severely affected by $[Cl^-]$.

3.1 Goal 1: Pitting Characteristics under Various Conditions

A pitting study was performed to better understand this behavior and to inform pre-fatigue corrosion protocols for Phase II testing. It was hypothesized that pitting processes in C465-H950 would be similar to those outlined in various steels, such as pit formation via MnS dissolution. These pits are of significance to the fatigue life because pit formation may directly impact crack nucleation, making pit formation time an important metric in fatigue life predictions. Despite being classified as a stainless steel, C465 is susceptible to corrosion attack

in aggressive environments and when subject to anodic polarizations, especially due to its low chromium content (12 wt%) relative to other stainless steels and its low PREN (14.3) [29, 60].

Two types of corrosion analysis were used to probe the pitting behavior and inform the exposure protocol to be used for the fatigue specimens. The first analysis of pitting behavior in C465 was to perform extended full immersion testing at the open circuit potential (OCP). Six polished pristine samples and six polished then lacquered samples were immersed in 2L of unbuffered, aerated 0.6M NaCl solution of pH=5.80. The samples were lacquered such that roughly 1cm² of one face was exposed; this was done to determine any crevice-like effects the lacquer may have generated. After 6 months, corrosion damage is not apparent by both visual and SEM inspection. After one year, extremely minimal pitting damage was visible via SEM and is shown in Figure 17. The corrosion damage shown is approximately 2μm wide. Similar damage is found across the metal, though the vast majority of the surface appears unaffected by immersion. Depth could not accurately be measured via SEM or interferometry. Similar results are reported by others using a 3.5% NaCl salt spray [30, 31].

The second type of corrosion analysis involved subjecting C465 to various anodic polarizations for various times in aerated NaCl solution. Coupons of C465 were soldered to a wire and embedded in epoxy exposing approximately 1cm². Each electrode was polished with 600 grit SiC grinding paper prior to electrochemical testing. Stop off lacquer was used to conceal the metal-epoxy interface from solution to avoid complications from crevice corrosion. Electrodes were immersed in a 0.6M solution and polarized to -200, 50, 100, and 150mV_{SCE} for up to 36 hours. Less aggressive polarizations (-200, 50, and 100mV_{SCE}) resulted in no pitting. A surface from most aggressive condition, 150mV_{SCE} for 36 hours, is shown in Figure 18. This surface shows numerous pits forming predominantly along polishing grooves. Pit density is approximately 30,000 pits/cm², calculated by counting pits in several, discrete 100μm² surface images. The pits are extremely small, less than 1μm in depth or width, though some polarizations rarely produced larger, irregularly shaped pits on the order of a few micrometers deep and up to 20μm in diameter. Microstructure characterization by Pioszak [115] reveals that C465 contains small islands of retained austenite, impurity inclusions (As-P-S), and NiAl-based precipitates randomly dispersed throughout the matrix. These features measure on the same order as the observed pit density and speculatively correspond to pit formation sites. However, the exact

origin of this type of damage is unclear (e.g. inclusion dissolution), and further investigation is outside the scope of this work.

The high pitting resistance is interesting due to the very low chromium (and general low alloy) content of C465. Higher chromium composition is associated with greater corrosion resistance, hence the stainless nature of stainless steel, and C465 barely qualifies as stainless with its 12% chromium composition. C465 has a PREN of 14.37, much lower than that of other stainless steels. By this metric, the pitting resistance of C465 should be markedly lower than other similar steels. There are a few possible explanations for this pitting resistance, and is likely a combination of factors. It is known that chromium and molybdenum work symbiotically to improve corrosion resistance. Although C465 has both of these alloying elements, they account for a smaller fraction of the material than similar steels like 13-8Mo, 15-5, Custom 450, Custom 455, and MLX17. Though nickel functions primarily to form strengthening precipitate phases, nickel additions generally improve corrosion resistance of stainless steels a variety of conditions [133]. Titanium has also been shown to improve pitting resistance and sequester sulfur in stainless steels [26]. Though the alloying effects of nickel and titanium have not been explicitly studied in C465, it is reasonable to consider similar improvements in corrosion properties. There are also very few deleterious elements, such as sulfur and phosphorous, which are almost entirely eliminated during the VIM-VAR manufacturing process. This high purity alloy prevents damaging inclusions from forming that would otherwise be prone to corrosion.

Despite this corrosion resistance, visual inspection and post-failure SEM fractography of Phase I fracture surfaces revealed that 3 specimens tested in 1.5 and 3.0M [Cl⁻] environments contained pitting damage on the order of 10 μ m within the notch. This suggests that *in situ* corrosion mechanisms may be enhanced by active loading and significant for fatigue life modeling. A major focus of Phase II experimentation is to understand how corrosion damage and the environment affect crack nucleation behavior. Based on preliminary studies, it is clear that measures would have to be taken to accelerate the pitting process. Therefore, four different pre-fatigue corrosion conditions each dedicated to a particular degree of corrosion damage were employed, the procedures of which are detailed previously. A series of experiments were conducted to develop repeatable, accelerated corrosion protocols capable of imparting reasonably consistent pitting damage to multiple fatigue specimens in a short time. One critical

caveat is that these pitting results cannot inform fatigue models incorporating the effect of fatigue loading concurrent with an aggressive environment as pits may form more readily under cyclic strain [134-136]. While the exposure conditions used in this study are by no means comprehensive, they shed light on the corrosion susceptibility of C465 in addition to ideally serving as crack-nucleating features reflective of those found in service conditions.

3.1.2 Corrosion Exposure Protocol Development

The results of the corrosion study described above served to inform the exposure conditions to be investigated in this research. For Condition 1, fatigue testing was performed on specimens polished with 600 grit SiC paper (the pristine condition) and fatigued in humid N₂ free of any additional corrosion damage. As in Phase I, this humid N₂ testing ideally serves as a baseline to which other tests subject to corrosion may be compared. The only real surface features are grooves imparted by the polishing process which run vertically up and down the specimen with a peak-valley maximum of approximately 500nm. A profile of this polish can be found in Figure 19.

Conditions 2 and 3 were exposed to corrosive conditions prior to the onset of fatigue loading via potentiostatic polarization. For Condition 2, the specimen was installed in a corrosion cell, loaded into the hydraulic frame, and immersed in the NaCl solution prescribed to that particular test (0.6, 1.5, 3.0M). The specimen was polarized to $-200\text{mV}_{\text{SCE}}$ for 24 hours prior to fatigue, after which fatigue loading immediately commenced. This approach allows for direct comparison to Phase I polarization characteristics and provides a baseline to see if cyclic loading will enhance the local pit formation since little damage is expected during the pre-fatigue exposure.

Condition 3 is identical to Condition 2 except that the specimen is polarized to $100\text{-}150\text{mV}_{\text{SCE}}$ for various times from 15 minutes to 48 hours prior to fatigue loading. Condition 3 produced a dense distribution of sub-micrometer pits littered across the surface. Rarely, an unusual, irregularly-shaped larger flaw (“rouge” flaw) was observed, measuring no more than $20\mu\text{m}$ in diameter and a few micrometers at most in depth. White light profilometry characterizing a typical, large flaw can be found in Figure 20. Despite evidence of corrosion damage, it is not clear that such small damage will be capable of forming a crack. Therefore, an

additional, more aggressive corrosion condition is desired to better understand the effect of corrosion damage on fatigue behavior.

Condition 4 corrosion damage is markedly different than that in previous conditions. This condition was designed to study a more severe corrosion state than in previous exposures, allowing for a detailed quantification of corrosion damage specific to this alloy. In order to simulate a more advanced corrosion state, four designer pits were galvanostatically (i.e. constant current) imparted into each specimen pre-fatigue to simulate existing corrosion pits that may arise from service conditions. Each pit was individually produced and any unique or aggressive chemistry forming inside the pit during galvanostatic pit growth is not present during cycling. However, these designer pits are similar in morphology and size to crack-initiating pits reported in limited literature ([67, 137]) and serve as a good starting point for understanding the interaction between existing corrosion damage and various NaCl environments in UHSS. Figure 21 shows some dissolution byproducts observed via SEM and energy-dispersive spectroscopy (EDS) prior to cleaning and fatigue. These byproducts are predominantly chromium-oxides, but nickel- and iron-based oxides are also expected as metal dissolution is uniform and the metal matrix is homogeneous on the scale of these pits.

Each pit was produced using identical electrochemical parameters and procedure. All pits were characterized pre-fatigue via white light interferometry. SEM was used to characterize some corroded surfaces (pits) pre-fatigue. Microscopy and white light profilometry shows that while each pit is similar, there are small differences in shape, size, and surface morphology. Figure 22 shows a typical pit from the fracture surface. These galvanostatic pits are reasonably smooth, which is similar to findings in literature [54, 138, 139]; such similarities are critical to ensure the relevance of this work since high current densities used during pitting could potentially skew the morphology to a smoother geometry. However, the regular shape of the pit is expected, unlike the pitting morphology associated with a rolled, heavily anisotropic aluminum alloys that contain clusters/stringers of constituent particles that govern the pitting process [72, 129, 140].

3.2 Goal 2: Effect of Various Exposure Conditions on Fatigue Life

This investigation of fatigue life of C465 in various conditions begins by analyzing the macro effect of exposure condition on fatigue life. Complete fatigue life versus $[Cl^-]$ based on

pre-corrosion condition are plotted in Figure 23. On average at a given $[Cl^-]$, Condition 4 appears to be the most damaging pre-fatigue condition, though other exposures often demonstrate only slightly better fatigue life performance. Fatigue life generally varies inversely with $[Cl^-]$ regardless of pre-exposure condition. Condition 4 tests demonstrate a strong dependence that fatigue life could decrease by an order of magnitude or greater as $[Cl^-]$ increased from 0.0006M to 3.0M, consistent with findings on other martensitic precipitation hardened stainless steel [6, 7, 32, 33]. These trends will be explained in the following sections. More qualitatively, each exposure condition produces markedly different fracture surface morphologies associated with nucleation and growth which may in turn play a significant role in overall fatigue performance.

3.2.1 Condition 1

Five dog-bone specimens were fatigued in a humid N_2 environment to failure. Exact initiation sites were difficult to pinpoint because neither marker bands nor river bands show on intergranular fatigue facets that were observed within roughly the first 50-500 μm of the formation site. Fatigue life behavior is very erratic and varied by a factor of three despite identical testing parameters; such behavior is consistent with high levels of variability often observed in the fatigue behavior in pristine specimens where microstructure features govern crack formation. Furthermore, every test experienced nearly identical initiation characteristics. No specific metallurgical initiation feature was observed in any test. SEM of the fracture surface proximate to the initiation site shows mixed transgranular and intergranular cleavage. Figure 24 shows some examples of the fracture surface at the initiation site. It appears that initiation occurs at the edge of a grain flush to the surface, which is sheared as the crack grows. Once the crack front has passed through the first grain, intergranular fracture dominates, though some transgranular behavior persists. This mixed-mode intergranular-dominated cracking continues for the next 300-600 μm , at which point transgranular quasi-cleavage accounts for 100% of crack growth up to failure. The environmental effects leading to IG based crack formation and small crack growth (<600 μm) in humid N_2 environments is poorly understood. It is unclear why this brittle IG fracture mode is more prevalent in humid N_2 environments where lower levels of H-embrittlement would be expected. While this finding is interesting, mechanistic investigation and interpretation of this behavior is outside of the scope of this project.

3.2.2 Condition 2/3

As detailed above Condition 2 a protocol was used where a section within the gauge was exposed to various $[Cl^-]$ concentrations and polarized to $-200mV_{SCE}$. The study above suggested that either no pitting or very small scale pitting would occur under these conditions; as such Condition 2 will investigate the effect of such pits on the fatigue crack formation and overall fatigue life. Condition 2 was applied to 5 dog-bone specimen 24 hours prior to fatigue in aqueous 0.6, 1.5 and 3.0M NaCl. Post-test analysis of the exposed surface demonstrated that the corrosion damage formed during the Condition 2 exposure process was non-existent. The dominant crack initiation features present in Condition 2 specimens were cube-like titanium carbide (TiC) intermetallic inclusions with edge lengths spanning 6-20 μm with an average edge length of 9 μm . Figure 25 shows the morphology and composition of these particles gathered via secondary electron imaging, backscatter electron imaging, and electron dispersive spectroscopy (EDS) in a FEI Quanta650 SEM. Spectroscopy is shown in Figure 26. Each initiating inclusion was sheared in two. Further investigation revealed that TiC inclusions are not uncommon, as there are many visible on fracture surfaces where transgranular fracture is the dominant mechanism. Figure 27 characterizes these inclusions in more detail.

More severe corrosion conditions were used for Condition 3; specifically, a section of the gauge was exposed to various $[Cl^-]$ and polarized to more aggressive conditions (100-150 mV_{SCE}) to try to investigate the effect of the unusual damage that was sporadically observed in the corrosion study under these conditions (Figure 20). Figure 28 shows an example of current corresponding to pre-fatigue and fatigue potential holds associated with Condition 3. Note the current shift in the cathodic direction at the conclusion of the pre-fatigue polarization. The crack will nucleate at the most detrimental, localized damage so investigating the effect of these rogue flaws is critical. All specimens subject to the Condition 3 pre-fatigue corrosion exposure (except for in 3M NaCl polarized to 100 mV_{SCE}) initiated on the same types of features as Condition 2 specimens. TiC inclusions were the primary microstructural initiation feature, dominant to the sub-5 μm corrosion damage imparted by the pre-fatigue exposure, described in depth earlier. No test initiated at a small, corrosion pit imparted via potentiostatic polarization. These findings demonstrate that despite a high density of <5 μm pits, inclusions, intergranular features, or other non-descript microstructural features dominate crack nucleation location. The TiC inclusions,

typically 8-12 μ m in depth, served as the crack formation site in 53% of initiations in Condition 2 and 3 tests.

A single anomalous test subject to this condition initiated on non-specific microstructural feature. SEM of the fracture surface reveals purely intergranular fracture morphology at the initiation site extending 200 μ m into the material at which point, transgranular cleavage mechanisms took over. However, portions of intergranular facets are prominent in the fracture surface for the remainder of the test. Unlike in humid N₂ testing, there is no transgranular fracture prior to the onset of intergranular cleavage, shown in Figure 29. The cause of this formation feature morphology is unclear, but may be associated with intergranular attack during the corrosion process that then served as severe site for crack formation during fatigue loading.

Of the six TiC inclusion sites, increasing inclusion size moderately correlates with decreasing fatigue life. Figure 30 plots this data and shows that R² for linear regressions between fatigue life and TiC size and area are 0.163 and 0.128 respectively. A closer inspection of inclusion initiation characteristics, however, reveals shows that fatigue life may be highly dependent on the shape and orientation of the TiC particle. The initiating TiC in four of these tests (red triangles in Figure 30) were cube-like with one edge protruding directly into the sample. These four tests also represent the four shortest fatigue lives of the 6 tests nucleating cracks at a TiC inclusion. Tests designated by blue circles also feature TiC particles initiating surface cracks, but these inclusions are very blunt and rounded compared to inclusions 1-4. Figure 31 shows micrographs of both sharp and blunt inclusions. The rounded TiC are of similar size, but their geometry and orientation within the specimens appear to significantly delay initiation, thereby extending N_f, suggesting that the geometry of an initiation inclusion has a strong influence on fatigue life. This shows that the geometry of the initiation inclusion may strongly influence the local plastic damage accumulation that leads to crack formation as a sharper inclusion will serve as a more acute stress intensity concentrator than a blunt inclusion.

Though TiC particles were the most prevalent initiation inclusion, a few other non-TiC inclusions did form cracks. Two 3.0M NaCl Condition 3 tests initiated a crack at non-TiC inclusions underneath the stop-off lacquer, completely isolated from the solution and electrochemical effects. These two tests also exhibited remarkable fatigue performance and will

be discussed in greater detail later. One initiated a crack at a very large silicon inclusion ($36\mu\text{m}$ deep x $57.9\mu\text{m}$ in radius), and the other at a small molybdenum/titanium sulfide inclusion ($5.5\mu\text{m}$ deep x $4.5\mu\text{m}$ in radius), shown in Figure 32 and Figure 33 respectively. Isolation from the aqueous chloride environment and pre-fatigue polarizations likely contributed to the long fatigue lives. However, it is unusual that a crack would not have initiated a crack in the metal exposed to solution and polarization, as observed in other tests. While the causes for these results remain unknown, it is important to note the presence of other inclusions in C465 and their potential to nucleate fatigue cracks.

The difference in fatigue life between Condition 2 and 3 is counterintuitive. Generally, specimens subject to a more severe pre-fatigue corrosion condition (Condition 3) experience longer fatigue lives than those subject to a less severe pre-fatigue corrosion condition (Condition 2). However, corrosion damage produced by each exposure is so minimal that other microstructural features and inclusions were the dominant crack nucleation sites. Independence from exposure condition is especially apparent in the case of TiC initiation tests in which the orientation of the particle seems to strongly affect fatigue life. Thus, given a greater sample size, fatigue lives of Condition 2 and 3 specimens would likely be more similar. *In toto*, the SN data and initiation feature analysis for Condition 2/3 show that neither (1) the size and smooth geometry of the pit, nor (2) the local material embrittlement proximate to the pit perimeter due to possible H charging during the dissolution process, were sufficiently severe to lead to crack formation. Rather, crack formation was governed by various microstructural features.

3.2.3 Condition 4

Due to the high pitting resistance in [Cl⁻] environments and the small/smooth nature of pitting in Conditions 2/3, it is necessary to artificially impart larger pits to study the pit-to-crack transition behavior. Condition 4 specimens (each with 4 pits) were fatigued in various chloride concentrations (0.0006-3.0M) and in humid N₂. In all but one specimen, the crack that led to failure formed at a corrosion pit. The lone exception was failure in humid N₂ that initiated a crack from an edge, which produced initiation and fracture characteristics identical to those observed in Condition 1 specimens. In general, the corrosion morphology produced by Condition 4 is in most cases sufficiently severe to drive crack formation to these pits rather than the microstructural features.

It is useful to quantitatively analyze the characteristics and features that lead to crack formation from the corrosion damage. Of the 56 total pits, 45% initiated a crack prior to failure which suggests that even though these relatively large smooth pits are sufficiently severe to shift crack formation away from microstructural features, they are still not sufficiently severe to always form a crack after a low number of fatigue cycles. The largest of the four pits on the specimen was the first to initiate a crack in only 29% of specimens. At 0.006M [Cl⁻] and above, the proportion of the 4 pits transitioning into cracks (22 of 40 or 55%) is significantly greater than that in 0.0006M and humid N₂ (3 of 16 or 19%). This data is limited but it suggests that the higher the [Cl⁻], the more likely a pit is to initiate a crack. Higher magnification fractography (4000-6000x, Figure 34) does not reveal any particular microstructural differences about the first marker band suggesting that initiation morphology is not directly related to environmental [Cl⁻] and subsequent hydrogen embrittlement.

3.2.3.1 Characterization of the Crack Formation Location within the Pit

Exact initiation locations and characteristics were collected via SEM imaging of both the corroded and fracture surfaces post-fatigue. Comparing the fracture and corroded surfaces allowed for the identification of the exact initiation location within the pit; detailed analysis of the white light interferometry images (Figure 15) and local stress analysis can then be determined. This process is shown in detail in Figure 35.

Each initiation location is plotted on an idealized corrosion pit in Figure 36. The graph is not an exact representation of every pit as each pit is slightly different, but it serves as a comparative tool. Of critical importance is that there was generally no prominent micro-feature within the macro-pit that was consistently observed at the crack formation location. Rather, the macro-pit features were more prominently correlated with the crack formation location. Crack initiation tends to occur closer to the equator of the pit perpendicular to the loading axis; specifically, 89% initiate within 40 μ m of the equator. This is expected as FEA models by Burns and Horner/Turnbull (Figure 37) predict the highest local stresses at the centerline across pits of various macro-scale dimensions; albeit for slightly different pit geometries [72, 137]. Burns models significantly larger hemispherical and semi-ellipsoidal pits with depths and widths on the order of hundreds of micrometers. Among the various models employed by Horner and Turnbull, the hemispherical pit with a radius of 100 μ m model most closely resembles Condition 4 pits.

Regarding the longitudinal location of pit formation, 72% of cracks initiated on the walls of the pit closer to the mouth than the base. This is consistent with FEA modeling efforts by Horner and Turnbull showing that certain regular pit geometries experience the greatest stress concentration on the pit walls moving from the base to the mouth along the pit centerline [137]. This finding also suggests that the variations in H-uptake about the pit surface are secondary, specifically during the pre-pitting process the pit chemistry and dissolution rates, thus H production rates, are likely the most severe at the pit base. Since no preferential crack formation occurred at the base of the pit, it suggests that such potential variations in the H concentration profile proximate the corrosion damage is of secondary importance. Also, since high hydrostatic stresses are known to attract interstitial H, it is possible that once loading commences that the loading frequency is sufficiently slow to allow the redistribution of these original H concentration profiles to align with the local stress fields. Regardless, this strong influence of the macro-pit stress concentration field on the crack formation location is consistent with similar findings by Turnbull for crack nucleation from smooth pits in a 12% Cr steel. Current findings are distinct from prior work on Al alloys where corrosion damage morphology was highly tortuous and crack formation was dominated by the local features on the pit surface rather than the global stress concentration field.

The green circles in Figure 36 show three instances in which the crack formed in a pit unusually far from the regions of highest stress. In each case, an inclusion was observed along the surface of the pit and formed a crack. These inclusions further increase the local stress/strain condition above that is associated with the macro-pit. When compared with other Condition 4 tests, overall fatigue behavior aligns with general trends suggesting that the severity of the local micro-features is balanced by the lower macro-scale stress location, yielding similar fatigue lives. Whether this interaction manifests itself in the crack formation regime or in the small crack growth regime is unknown and outside the scope of this work. Regardless, crack formation from severe micro-features is consistent with previous work on aluminum alloys showing that the crack nucleation site depends more on local inclusions than the macro stress state caused by the pit. It also highlights that the differences in corrosion morphology lead to different pit-to-crack transition behavior for steel and aluminum.

Analysis of pit initiation location as a function of [Cl⁻] has been performed to see if any trends are related to bulk environment composition. Figure 38 displays every initiation location as a function of the testing environment. It shows that chloride concentration is not a strong indicator of crack initiation location. Pits subjected to less aggressive environments are slightly more likely to initiate closer to the equator and the base of the pit than pits in more aggressive environments. This may also be explained by Horner and Turnbull's models of strains inside a pit. Increased lattice strain is detrimental to the continuity of the passive layer in the pit. This may not be a prominent factor in low [Cl⁻] test as the environment may not be aggressive enough to either destabilize the passive film or even in the event of passive layer breakdown/rupture to cause significant damage to the base material. However, in more aggressive environments, active corrosion may destabilize the film and more quickly damage the base material upon exposure. This local discontinuity may elevate the local strain areas along the walls of the pit (further from the base), and would be a more active mechanism for high [Cl⁻] fatigue tests. Regardless, the correlation between [Cl⁻] and pit formation location is tenuous and generally suggests that there is not a strong role of bulk [Cl⁻] on the crack formation location within the pit.

3.2.3.2 Macro-scale Pit Characteristics

In general, fracture mechanics-based approaches to crack formation predictions will consider the size (depth or area) of the initiating feature as the primary metric to define the severity of the crack formation features [72, 129, 141, 142]. While this approach was found to not be generally rigorous for 7xxx-series aluminum alloys with highly tortuous corrosion morphologies [126], the smoother nature of the designer pits suggests that such an assumption may be justified for the current results. As such, it is worthwhile to analyze and discuss characteristics of initiation features; specifically, (1) depth to which the deepest part of the initiation feature protrudes into the specimen perpendicular to the surface and (2) the area of the 2D feature that is observed on the fracture surface.

For Condition 4 specimens, the pit depth and cross-sectional area versus the fatigue life are plotted in Figure 39, excluding the pits where nucleation formed from an inclusion on the pit surface. Larger flaw sizes and higher chloride concentrations are expected to correlate with markedly lower fatigue lives. Pit depth and area weakly correlate to fatigue life ($R^2 = 0.251$ and 0.48 respectively), however, the result is counterintuitive in that larger pits correlate with longer

fatigue lives. This does not align with mechanistic intuition dictating that larger flaws will produce a larger region of increased stress (i.e. the red region in Figure 37-a) than will smaller flaws. Increasing the region of maximum stress increases the odds that a crack-nucleating microstructural feature falls within this region. By this reasoning, a larger flaw should correlate with a lower fatigue life. The observed trend may be a result of specific pit geometry. Much like the differences between sharp and blunt TiC particles, smaller pits may act as more favorable nucleation features on account of pit geometry (e.g. steeper pit walls) than larger pits. Additionally, these smaller pits may be more prone to passive film breakdown, leading to a decrease in fatigue life unrelated to the actual size of the pit.

To go one step further, Figure 39 also graphs the fatigue life against the cross-sectional area of the initiating feature since some researchers have suggested a stronger correlation with this areas parameter and crack formation life [141]. Again, there is a counter-intuitive trend showing that larger pit sizes result in longer fatigue lives. This does not explain any of the fatigue life trends observed with respect to either [CI] or initiation feature character.

Of note is that each of these comparisons includes testing from all of the different [CI]. Figure 40 plots the Condition 4 specimen lives and indicate the [CI] associated with each of the data points. If the correlation between the pit depth/area and the cycles to failure was being obfuscated by differences in [CI] then it would be expected that the smaller cracks with shorter lives would all correlate to high [CI] and the larger cracks with longer lives would correlate to low [CI]. This trend is not clearly evident, suggesting that the analysis above is not negated by the testing environment. *In toto*, these data show that there is not a strong correlation between fatigue life and pit dimensions. This is likely attributable to the fact that the pits do not greatly differ in size or geometry. While the graphs in Figure 39 show a distribution of pit depths and cross-sectional areas, the fine length/area scales on the y-axes serve to highlight only minor differences in pit dimensions that exert minimal influence on fatigue life.

It is also useful to compare fatigue life data between pits and inclusions as shown in Figure 41. Despite the designer pits being approximately an order of magnitude larger in depth (over two orders larger in area) than the inclusion features, the detrimental effects of the initiation feature is much less pronounced. In 0.6M NaCl environments, data show that Condition 4 fatigue life is 2-3-fold less than that demonstrated by specimens initiating on a blunt

inclusion. In the same environment, fatigue lives associated with sharp inclusions can be as low and no more than 2-fold greater than those of Condition 4 pits (green box). This suggests that the smooth nature of the pit limits its severity, similar to the less damaging orientation of the blunted inclusion compared to the sharp inclusion geometry.

3.3 Goal 3: Quantitatively Assess the Influence of [Cl⁻] on Fatigue Life

The prior sections have established the influence of [Cl⁻] on the development of the corrosion damage and discussed the aspects of the resulting corrosion morphology that are important to the crack formation process. The pitting studies indicate that the pitting life, or the life required to form a pit capable of nucleating a crack, can be extremely long (e.g. no pits were formed during OCP exposure after 1 year). Corrosion damage from natural and anodic conditions in a static environment will not form a crack at the timescales associated with the 2Hz loading frequency performed in this research. Additionally, small anodic polarizations near OCP (-200mV_{SCE}) during fatigue loading failed to produce corrosion damage sufficient to nucleate a fatigue crack. Other microstructural features played a more prominent role in crack initiation, making the term N_{pit} irrelevant in this study since the fatigue crack formation life was not dictated at all by natural pitting processes. Though the N_{pit} term is not relevant for the conditions investigated in this study, this term cannot be ignored in future modeling efforts, particularly when the loading frequency is low and concurrent with exposure to an aggressive environment. This research does not deeply investigate the effect of mechanical damage on pitting characteristics as most pitting damage was performed on an unstressed sample or specimen. However, researchers have suggested that an applied load may influence the pitting process [134-136, 143]; N_{pit} therefore is highly dependent not only on environment but also stress state. Regardless, for this work, the N_{pit} behavior is not observed to be a controlling factor of N_f , thus the remaining work will focus on the effect of [Cl⁻] on the fatigue behavior of Condition 4 pre-corroded specimens.

This section will quantitatively discuss the fatigue life trends associated with varying [Cl⁻] for a single constant pre-corrosion conditions (Condition 4). Figure 23 (blue circles) presents the fatigue life data from Condition 4 as a function of [Cl⁻] and suggests that there is a significant increase in fatigue life with decreasing chloride concentration. Specifically, as the [Cl⁻] decreases from 3.0M to 0.0006M, a 4-9-fold increase in the fatigue life is observed despite

similar initiation feature morphologies. This is significant as literature studies often will attribute the effect of chloride concentration on the fatigue life to the development of corrosion damage to serve as crack nucleation sites. While the trend of increasing life with decreasing $[Cl^-]$ is clear for the aqueous solutions, it is not clear why the Condition 4 humid N_2 testing resulted in fatigue lives that were relatively low compared to the Condition 4 0.006M and 0.0006 M NaCl results. Fracture surface morphology in Condition 4 specimens in low $[Cl^-]$ is purely transgranular emanating from the pit (Figure 22). This morphology differs greatly from that observed in Condition 1 which showed simultaneous transgranular and intergranular fracture heavily favoring the latter mode (Figure 42). While a full discussion of this behavior is outside the scope of this work, the fracture morphology associated with the humid N_2 Condition 1 and 4 exposures suggests a distinct environmental mechanism that favors intergranular decohesion for seemingly more inert environments.

3.4 Goal 4: Establish Relative Influence of $[Cl^-]$ on Different Fatigue Regimes

The S-N data for Condition 4 reported in Figure 23 must be unpacked to determine which corrosion fatigue regime (N_i , $N_{p\text{-small}}$, N_p) detailed in Equation 1 account for this trend. While the trend of increasing life with decreasing $[Cl^-]$ has often been observed in literature, it does little to extend our knowledge of low chromium UHSSS environmental fatigue processes. However, the current detailed experimental approach and characterization allows for precise quantification of corrosion damage, crack formation, small crack growth, and long crack mechanics which will help explain exactly how fatigue life of corroded specimens is a strong function of $[Cl^-]$ and what environmental fatigue mechanisms are prominent failure criteria of this low chromium UHSSS.

The discussion will first present results from standard SEN long crack testing to inform and establish the standard continuum environmental growth rates in the absence of chemical and mechanical small crack complexities. These complexities will be characterized by analysis of marker band data of the fracture surfaces from each $[Cl^-]$. Finally, an analysis of the crack formation life will be presented. This analysis will establish the dependence of each cracking regime on $[Cl^-]$, and in turn will elucidate which regime(s) dictate the environmental dependence observed in overall fatigue life.

3.4.1 Crack Propagation

Researchers have put forth various superposition models to try to decouple mechanical and environmental effects on fatigue crack growth [144]. This work will contextualize results in the environmental fatigue framework of the following equation, based on a model developed by Wei [79, 145]:

$$\frac{da}{dN} = (1) \frac{da}{dN_{Vac}} + (2) \frac{da}{dN_{CF}} + (3) \frac{da}{dN_{SCC}} \quad (4)$$

This theory states that the observed crack growth rate is the sum of three superpositioned driving forces: (1) inert environment cracking driven purely by mechanical damage, (2) aggressive environment cracking due to hydrogen production at the crack tip and interaction with cyclic damage accumulation, and (3) aggressive environment monotonic load cracking due to portions of the loading cycle exceeding the K_{ISCC} . In this research, humid N_2 testing replaces the inert environment contribution. Though the humidity will undoubtedly have some effect on da/dN , it proves to be the most inert environment in the scope of this research and serves as a sufficient baseline for comparing crack growth kinetics. Additionally, monotonic loading and subsequent investigations into the pure SCC contribution to da/dN is outside the scope of this work, however, a parallel study conducted by Pioszak and Gangloff was conducted to shed light on this mode of crack growth [115]. Long crack fatigue testing provides sufficient information to further analyze the remaining corrosion fatigue driving force.

3.4.1.1 Long Crack Growth

Phase I experimentation provides excellent insight into environmental effects on fatigue crack growth and determining fatigue phenomenology. Though the data presented in this section was not generated by Condition 4 tests, it can still be applied to the fatigue life model (Equation 1) since long crack growth kinetics are expected to conform to fracture mechanics-based similitude once ΔK values fall within the Paris regime. Specifically, once the crack depth reaches a sufficient length, it is assumed that crack tip occlusion will create a consistent and aggressive crack tip environment. While the exact crack length value is unknown, Brown suggested that after 1mm of crack growth in a CT specimen that the chemistry reached a near constant condition for high strength steels [107].

The effects of [Cl⁻] on long crack growth regime (N_p) with respect to ΔK are reported and analyzed. Tests were conducted in environments outlined in the experimental section. Each specimen was subject to two loading regimes: (1) increasing ΔK and K_{max} maintaining a stress ratio $R=0.5$ from $K_{max}= 27.5-55 \text{ MPa}\sqrt{\text{m}}$, and (2) constant K_{max} and decreasing ΔK . These two regimes are visually represented in Figure 10. The first regime establishes long crack growth rates over a wide range of ΔK at a constant stress ratio. The second set establishes crack growth rates across a wide range of stress ratios and provide insight into fatigue cracking thresholds characteristic of this material at low ΔK . In addition to establishing fatigue crack growth rates for future modeling efforts, a number of secondary trends are observed that help elucidate electrochemical and mechanical phenomena occurring at the crack tip. The results are presented below followed by an analysis to better quantify the effect of [Cl⁻] on long crack growth.

3.4.1.1.1 Increasing K

Increasing $K/\Delta K$ data for all tests is presented in Figure 43. All specimens were fatigued at a nominal stress of 300MPa in order to initiate a crack. Two tests lack da/dN data at ΔK below about $16\text{MPa}\sqrt{\text{m}}$. This data is intentionally truncated because these tests did not initiate after the first million cycles, so the initial stress had to be significantly increased to induce initiation, invalidating data near initiation. The increased stress values associated with these tests are reported in the legend. Though a constant potential of -200mV_{SCE} was applied to each specimen for the duration of each test, one test was intentionally performed at -550mV_{SCE} and another was unintentionally performed at a variable potential falling in a window between $-200/-300\text{mV}_{SCE}$. Fractography reveals transgranular cleavage as the fracture mechanism, as shown in Figure 44 as cracks likely propagate through grains along and through martensite laths.

A humid N_2 test was performed first to serve as a baseline for environmental da/dN comparison. This da/dN is lower than that of all immersion testing at every ΔK with the exception of the early stages of one 0.06M test and a brief dip in da/dN for one 3.0M test. All tests considered, crack growth rates vary by a factor of 1.67-2.8x from humid N_2 across 0.0006M-3.0M [Cl⁻]. Plateaus occurred from initiation ($\Delta K \approx 10\text{MPa}\sqrt{\text{m}}$) to a $\Delta K=15.5\text{MPa}\sqrt{\text{m}}$ in 3.0M [Cl⁻] solution and to $\Delta K=12.8\text{MPa}\sqrt{\text{m}}$ in 0.6M [Cl⁻] polarized to -550mV_{SCE} during increasing-K testing. This plateau is attributed to the superposition of SCC and is fully detailed in Appendix A. Also of interest is that above roughly $16\text{MPa}\sqrt{\text{m}}$, the experiment conducted in DI

water showed crack growth rates higher than those observed for the $[Cl^-]$ environments. While not fully understood, such behavior has been previously reported in the literature [146, 147] and discussed further in Appendix B.

3.4.1.1.2 Decreasing K

Decreasing-K data showing crack growth rates as a function of ΔK is presented in Figure 45. Crack growth rates from the increasing- ΔK testing strongly agree with these crack growth rates despite different loading protocol. Again, the humid N_2 test again serves as a baseline reference point. Humid N_2 environment da/dN is slower than all immersion testing at every ΔK except for the two tests conducted in 0.006M NaCl at $\Delta K \leq 12.6 \text{MPa}\sqrt{\text{m}}$. Below this ΔK , crack growth rates from humid N_2 and 0.006M $[Cl^-]$ environments are essentially identical. However, da/dN data collected from fatigue tests where $[Cl^-]$ was 0.0006, 0.006, 0.06M showed little variation. For these low $[Cl^-]$ tests and the humid N_2 test, the K_{TH} ranges from 3.8-4.5 $\text{MPa}\sqrt{\text{m}}$. The slightly lower values for the low $[Cl^-]$ environments compared to humid N_2 is likely attributed to typical scatter.

Distinctly different decreasing-K crack growth behavior is observed for the DI water test, for higher $[Cl^-]$ tests ($< 0.6\text{M}$), and for the cathodically polarized test in 0.6M NaCl. Crack growth rates in each of the high $[Cl^-]$ tests show agreement with those from lower $[Cl^-]$ tests at higher ΔK . As each test progressed, each of these tests deviated from the expected relationship between ΔK and da/dN at different, specific ΔK values. These deviations were characterized by a plateau in which da/dN remained relatively constant seemingly independent of ΔK to the conclusion of the test. Specific ΔK values and their respective environments are detailed in Table 6. These accelerated rates continued well past the $\approx 4 \text{MPa}\sqrt{\text{m}}$ threshold established by lower $[Cl^-]$ tests and continued until the conclusion of the tests. Deviations from the expected trend coincide with drastic morphological changes on the fracture surface; specifically a transition from transgranular cracking at higher ΔK to intergranular cracking in the plateau region. This behavior is attributed to the onset of cyclically-induced SCC well below the K_{ISCC} of the material under purely monotonic loading. The current discussion is focused on understanding the $[Cl^-]$ behavior observed for Condition 4. In these tests, no intergranular failure was observed, suggesting that the cyclically-induced SCC behavior is not active. A full description of the plateau behavior will be addressed in Appendix A.

3.4.1.1.3 Corrosion Fatigue

Purely corrosion fatigue effects are generally noted in specimens subject to a lower $[Cl^-]$ environment and at ΔK greater than approximately $10\text{MPa}\sqrt{\text{m}}$, exceeding the minimum ΔK necessary for crack growth. Most crack growth data gathered in the increasing-K regime from environments of $[Cl^-]$ between 0.0006M and 1.5M are well aligned and show similar trends. In early stages of the tests at low ΔK ($\approx 10\text{MPa}\sqrt{\text{m}}$), there is little difference between da/dN collected from tests in humid N_2 and in chloride containing solutions. By about a $\Delta K=11.5\text{MPa}\sqrt{\text{m}}$, da/dN collected from immersion testing consistently increase and separate entirely from the humid N_2 baseline test. Once this separation occurred, aqueous crack growth rates remained greater than humid N_2 rates for the remainder of the test. Figure 46 contains an abridged collection of increasing-K data to more easily visualize these trends. The crack growth rate data are reported for crack length values greater than 1.0mm , which is 0.5mm past the notch. This could be indicative of the onset of crack tip occlusion occurring at a crack length of approximately 1.4mm which corresponds to a ΔK of approximately $12.1\text{MPa}\sqrt{\text{m}}$, which is marked in Figure 43 with a black line. Specifically, at small crack depths (ΔK below the black line), crack growth rates for aqueous chloride and humid N_2 environments were similar because the chemistry at the crack tip is likely easily mixing with the bulk environment, preventing formation of an aggressive environment. At a certain crack length, the crack tip may have been sufficiently occluded from the bulk solution, becoming more aggressive and accelerating crack growth. The crack tip may remain occluded for the duration of the test provided that mass transport from the side is slow enough to maintain an occluded chemistry. Transport from the side represents a smaller diffusional distance than that down the length of the crack, thus, these diffusion kinetics will define crack tip chemistry once the crack length exceeds half the specimen width.

Similar results are found in decreasing-K tests where $[Cl^-]<0.6\text{M}$ as seen in Figure 47; specifically corrosion fatigue effects are evident though relatively small. Crack growth rates steadily declined with decreasing ΔK from $30\text{MPa}\sqrt{\text{m}}$ down to $4\text{MPa}\sqrt{\text{m}}$. $4\text{MPa}\sqrt{\text{m}}$ represents the fatigue crack growth threshold as crack growth rates drop precipitously at this ΔK , effectively representing crack growth arrest. Low $[Cl^-]$ tests of 0.0006 , 0.006 , and 0.06M show agreement in that they all exhibit similar, slightly higher da/dN than the humid N_2 at all ΔK with the one exception noted above. There is little variability in both the crack growth rates and the

threshold value, indicating that the [Cl⁻] does not play a major role on fatigue crack growth and threshold behavior at these low concentrations.

To investigate how the observed changes in [Cl⁻] would influence the overall fatigue life of a bar, LEFM fatigue life prediction software (AFGROW) was used to predict total fatigue life using these corrosion fatigue crack growth rates. A simulation was performed specifying a 100 μ m semi-elliptical surface crack, R=0.5, and $\sigma_{\max} = 50\% \sigma_{ys}$, and crack growth rates from the 1.5M NaCl and humid N₂ environments (Figure 43). These simulations report only a 1.5-fold decrease in the predicted fatigue life based on the faster crack growth rates from the 1.5M NaCl environment. This result suggest that chloride-containing environments will cause faster growth rates but the difference in rates and their net implication on fatigue life in C465 is rather small. As such, it is necessary to further examine the small crack propagation behavior and the crack formation behavior.

3.4.1.2 Small Crack Growth

The fatigue behavior of small cracks is often significantly different than that of long cracks and do not conform to LEFM models. In many cases, short cracks propagate at unusually high rates, resulting in non-conservative lifetime models. This research quantifies small crack growth rates to determine how they are influenced by [Cl⁻]. The interactions of crack tip acidification and mechanical loading will play a role in small crack growth kinetics. While a detailed analysis of the crack tip environment and calculation of the microstructure scale crack tip driving forces is outside the scope of this research, this section will present data regarding how the rates at which cracks progress from the pitting damage induced in Condition 4.

Small crack growth rates (da/dN) are calculated by measuring the distance between discrete marker bands and dividing by a known number of cycles. Figure 48 provides a visual representation of the marker banding identification process. The figure shows both short range marker bands proximate to the crack and long range marker bands highlighting a continuous crack front. Higher magnifications are required for accurate quantification of marker bands near the crack. After a couple hundred micrometers of crack growth, marker band morphology is visible at lower magnification which also allows measurement of the final marker band, the dimensions of which are input into AFGROW for residual life modeling. Together, these low and high magnification micrographs fully capture all marker band data.

Small crack growth rates are normalized as much as possible by measuring marker bands along a single trajectory perpendicular to the initiation site surface. In this single trajectory approach it is possible to observe the influence of microstructural features on crack growth. Prior work clearly demonstrated that the source of these oscillations in the data are likely due to crack front interactions with grain boundaries [126, 148]. Crack growth rates are plotted against the measured distance from the formation feature (a) instead of against the conventional ΔK . Creating a valid plot using ΔK would require a K-solution analysis for each test which is outside the scope of this work. While this approach will clearly induce errors associated with comparing growth rates propagating by different mechanical driving forces, this is ameliorated by the similarity of the macro-pit sizes and the generally homogenous nature of crack formation locations observed in Figure 36. As such, while the comparison of the growth rates is not full rigorous, useful trends can be observed in the context of Goal 3. Additionally, specimens failing due to intergranular fracture mechanisms did not produce reliable marker bands, preventing collection of crack growth data. This data loss occurred in all humid N_2 tests and a limited number of immersion tests as detailed above.

Small crack growth rates were collected for Condition 4 and plotted in Figure 49. Crack growth rates generally increase with increasing distance from the initiation point, though not in a predictable or linear manner, especially close to the initiation site. Many cracks have fluctuating growth rates, and consecutive measurements of da/dN often do not represent an increase. Bulk [Cl] appears to have little effect on small crack growth rates.

3.4.1.2.1 Variability in Growth Rates

The crack growth rates in Figure 49 are consistent with the expected strong variability in the early stages of small crack growth; specifically the highest measured crack growth rates are up to 7 times greater than the lowest. This is not unexpected as cracking proximate to the initiation site is highly subject to the stress field of the initiation feature, local grain structure, and crack geometry [126, 149]. As the crack advances, non-environmental factors such as crack tip shielding, enhanced plasticity, and crack shape remain major factors determining growth kinetics. Short cracks only span one to a several grains at once, thus crack growth is highly subject to local microstructural effects. Some tests even show decelerating da/dN in the early stages of crack growth. As the crack grows, it assumes a more hemispherical shape, intersecting

many grains simultaneously, effectively transitioning from microstructure scale cracking to a continuum crack that represents the aggregate material response rather than that of a single or a few grains along the crack front.

3.4.1.2.2 Effect of [Cl⁻] on Small Crack Growth

Figure 49 shows the effects of bulk [Cl⁻] from 0.0006-3.0M on the small crack growth from Condition 4 pits. This graph only presents data collected from pitted specimens, as the initiation features are approximately identical and pits are the only corrosion feature to be successfully tested over a wide range of [Cl⁻] values. In general, it seems that lower [Cl⁻] environments produce a slightly slower growth rate than higher [Cl⁻] environments, but there is not enough data or appropriate analysis to draw a definitive conclusion. It is expected that higher [Cl⁻] tests exhibit faster crack growth, however, the highest growth rates in this regime are observed in a 0.06M [Cl⁻] test. This suggests that bulk [Cl⁻] does not strongly correlate to crack propagation rates in the microstructurally small crack region.

Fracture morphology (and thus mechanism) shows some dependence on environmental conditions and bulk [Cl⁻]. Though fracture morphology is generally purely transgranular for [Cl⁻] of 1.5M and below, Figure 50 shows a typical transgranular to intergranular morphology characteristic of tests conducted in 3.0M NaCl. The transition at a crack length of about 200 μ m indicates that the environment plays some role in fracture mechanism, but growth rates between mechanisms cannot be compared as crack growth rates could not be collected from intergranular fracture surfaces. Measureable crack growth rates vary little with [Cl⁻] from 0.0006M-1.5M, suggesting that the largely environmentally-independent small crack growth is not a major factor in the environmentally-dependent total fatigue life.

In toto, the analysis of the crack propagation behavior has demonstrated that neither the long nor short crack growth behavior exhibits dependence on bulk [Cl⁻] that is significant enough to account for the observed 4-9 fold increase in fatigue life as [Cl⁻] decreased from 3.0M to 0.0006M. This suggests that the crack formation life from the Condition 4 corrosion damage must be the controlling regime.

3.4.2 Crack Formation Life

Crack initiation is a result of complex interactions of the initiation feature, bulk environment composition, corrosion damage and microstructure. Section 3.2 identified microstructure and corrosion damage features that were critical in determining where the crack formation would occur, however, merely identify those features is insufficient to inform and validate efforts to model the crack formation life. The crack formation life is calculated for each of the Condition 4 experiments enabling analysis of N_i with respect to the bulk chloride concentration. Fractographs of an individual marker band and a marker band series are included in Figure 48. Crack propagation life from the first to the last resolvable marker band is easily calculated from the fatigue loading protocol. Past $\approx 500\mu\text{m}$, marker bands less clearly marked the fracture surface. As such, the faint fracture surface marks were augmented and validated with LEFM-based fatigue life prediction software (AFGROW) that calculated the expected crack progression in the region where fracture surface markers were difficult to identify. This approach is justified based on the applicability and rigor of such continuum fracture mechanics predictions for cracks of this size scale and at ΔK values that are within the Paris regime. Modeling employed a semi-elliptical surface crack of dimensions equal to the depth and width of the last marker band in conjunction with loading parameters and crack growth rates derived from Phase I. The quantitative fractography was coupled with LEFM estimates of the incremental crack advance associated with a given number of cycles to provide reliable values of the remaining fatigue life from the last clear marker band to specimen failure. By leveraging the LEFM prediction capabilities and the fracture surface marker-banding technique, an accurate calculation of initiation life to a crack depth of $<5\mu\text{m}$ is achieved.

3.4.2.1 Effect of Chloride Concentration on Initiation Life

Figure 51 plots the total fatigue life, the initiation life to $25\mu\text{m}$, and the initiation life to $5\mu\text{m}$ for Condition 4 specimens in various aqueous $[\text{Cl}^-]$. Humid N_2 test data is limited due to the intergranular fracture character. At high $[\text{Cl}^-]$ of 1.5 and 3.0M, 75% of primary pits initiated a fatigue crack within the first 1,000 cycles. $N_{i,25}$ and fatigue life is also consistent at these high $[\text{Cl}^-]$. As $[\text{Cl}^-]$ decreases to 0.6M and 0.06M, N_i becomes more delayed, in some cases reaching close to 10,000 cycles before a crack is initiated. As $[\text{Cl}^-]$ decreases further to 0.006M and 0.0006M, the shortest crack initiation life is approximately 20,000 cycles and the longest is well over 100,000. In short, as $[\text{Cl}^-]$ decreases from 3.0M to 0.0006M, N_i significantly increases by as

much as two orders of magnitude. This is similar to the relationship reported in literature between $[Cl^-]$ and N_f , indicating that N_i is potentially the controlling factor in determining N_f .

It is reasonable to assume that pit chemistry will remain fairly static as pits will not experience significant active dissolution, as evidenced by the former pitting study results and Condition 2 corrosion morphology. Because these pits are produced prior to fatigue testing and have no special pit chemistry, the $[Cl^-]$ in the pit will be that of the bulk. The stability of the passive film diminishes as environmental $[Cl^-]$ increases, leading to accelerated breakdown of the passive film at higher $[Cl^-]$, exposing the base metal to solution and promoting hydrogen uptake or additional localized corrosion damage. Applied cyclic stresses will accelerate this process, mechanically assisting the breakdown of the passive film due to local strain effects, which will be further amplified by the morphology of the pit relative to the smooth, polished surface. Thus it is reasonable to expect shorter fatigue life in higher $[Cl^-]$ environments. Fatigue life in humid N_2 is greater than that observed in most aqueous chloride environments, though both tests conducted in 0.006M NaCl exhibit longer fatigue lives. As previously noted, the intergranular nature of the fracture surface suggests that a different environmentally induced corrosion fatigue mechanism is at play. Unfortunately, initiation life data was lost for these humid N_2 tests, precluding comparisons between the initiation life characteristics between humid N_2 and aqueous chloride environments.

The propagation life (cycles from the first marker band to failure) can be analyzed with respect to $[Cl^-]$ to observe any macro trends between $[Cl^-]$ and propagation life that may exist. Figure 52 shows the total crack propagation life for Condition 4 specimens in their respective environments. Crack propagation life increases slightly with decreasing $[Cl^-]$, there is no more than a two-fold variation between the data at 0.0006M and 3.0M. This slight decrease in crack propagation life with increasing $[Cl^-]$ is fully consistent with the observed long crack trends (Figure 43) and small crack trends (Figure 49). However, differences in environmental crack propagation life are of secondary importance when compared against the 1-2 orders of magnitude differences in initiation life over the same $[Cl^-]$ range, further suggesting that N_i is the dominant factor in fatigue life.

These findings are critically important to structural applications and related modeling efforts. Lifetime predictions for structural components are calculated via LEFM models that

often assume that the observed pit size is the initial flaw or crack size. LEFM models cannot be applied to initiation features below a critical size because a crack spanning few grains does not represent the continuum crack model applicable to the Paris relationship between ΔK and crack growth rates. Additionally, these models ignore the time required to form a crack from a pit by assuming that fatigue cracks are propagating throughout the simulation provided K_{TH} is exceeded by the applied stress level. The research suggests that this assumption is erroneous as the initiation life to $5\mu\text{m}$, and more importantly $25\mu\text{m}$, constitutes a significant proportion of the total fatigue life, resulting in highly over conservative fatigue life predictions. This highlights the importance of accurately modeling the crack formation life; such work could significantly improve the fidelity of structural integrity modeling.

4 Conclusions

The goal of this work was to evaluate the environmental dependence of different stages of corrosion fatigue crack nucleation and growth to elucidate specific factors responsible for the deleterious effects of chloride concentration on fatigue life in a precipitation-hardened martensitic UHSSS. The total fatigue life was broken into its four components so that the effect of environmental $[\text{Cl}^-]$ on each could be independently studied. Over the course of this research, pitting characteristics of C465 were studied and reproduced to evaluate the effect of corrosion damage on fatigue behavior. Crack nucleation behavior and its dependency on corrosion damage were characterized. The overall effects of $[\text{Cl}^-]$ on fatigue life were gathered, and further analysis into determining which corrosion fatigue regimes are most accountable for these trends was conducted. Conclusions are framed in the context of the four goals of this research:

Goal 1: Study pitting characteristics of C465-H950 at open circuit and anodic polarizations to develop controlled, repeatable pitting protocols. These protocols are then used in tests to evaluate the effect of corrosion damage on fatigue behavior.

- Custom 465-H950 exhibited a strong resistance to corrosion for various levels of aqueous chloride exposure
 - o After 1 year of full immersion in 0.6M NaCl at OCP, a low density of pits less than $2\mu\text{m}$ in width and no appreciable depth were observed.

- Custom465-H950 is resistant to pitting at significant anodic overpotentials. After 36 hours in 0.6M NaCl at a 350mV overpotential, a dense, uniform distribution of sub-micron pits had formed.
- Based on these findings, four pre-fatigue corrosion conditions were developed for use to achieve Goal 2.

Goal 2: Characterize fatigue crack formation location with respect to various corrosion-induced initiation features and investigate links between surface morphology, crack nucleation behavior, and fatigue life.

- Crack nucleation for Condition 1 (pristine specimens in humid air) was governed by microstructure features. Interspersed intergranular and transgranular facets were observed on the fracture surface, suggesting an environmental influence despite the relatively inert moist air environment. Detailed investigation of this behavior was outside the scope of this work.
- Conditions 2 and 3 (broad surface exposure at various $[Cl^-]$ and polarizations) failed to produce sufficient pitting damage and/or subsequent local material embrittlement due to possible hydrogen charging to initiate a fatigue crack. Instead, cracks nucleated from inclusions (primarily TiC) and other non-specific microstructural features, making the N_{pit} life irrelevant in this study.
 - The geometry and shape of crack-initiating TiC inclusions appear to be significant factors governing fatigue life.
 - Together, the high resistance to corrosion damage and the relatively smooth nature of pits makes this alloy highly resistant to corrosion-nucleated fatigue in aqueous chloride environments.
- Condition 4 pits were more detrimental to fatigue life than corrosion damage from any other exposure
 - Crack nucleation in large pits is more strongly influenced by macro-pit features and stresses than micro-features within the pit.
 - The majority of pit-nucleated cracks form along the pit equator on the pit walls, away from the base, consistent with the modeling efforts of others.
 - Chloride concentration does not dictate crack nucleation location within a pit.

Goal 3: Quantitatively assess the deleterious effect of [Cl⁻] on the overall fatigue life of pre-corroded specimens of C465-H950.

- As reported for similar metals, the fatigue life of C465-H950 is strongly influenced by bulk [Cl⁻].
- Condition 4 pits repeatedly demonstrate the shortest fatigue lives among all four conditions, though Condition 2/3 occasionally exhibited only slightly better performance.

Goal 4: Quantitatively assess crack formation, small crack growth and long crack growth in the context of S-N behavior of pre-corroded specimens to identify the corrosion fatigue regime(s) most severely affected by [Cl⁻].

- Fracture surface marking load protocols were developed and implemented to measure small crack growth and to quantify initiation life within 5 μ m of the initiation point.
- Neither the long nor short crack growth behavior exhibits dependence on bulk [Cl⁻] that is significant enough to account for the observed 4-9 fold increase in fatigue life as [Cl⁻] decreased from 3.0M to 0.0006M.
 - o Long crack growth rates do not vary greatly with [Cl⁻]. Based on LEFM lifetime predictions, variations in crack growth rates in [Cl⁻] produce only minor changes in fatigue life.
 - o Short crack growth rates and behavior are largely independent of [Cl⁻] except for at 3.0M where the fracture mechanism is markedly different than that at lower [Cl⁻].
- Initiation life is the main factor governing fatigue life in this study. For Condition 4 specimen, initiation life was shown to increase by as much as two orders of magnitude as [Cl⁻] was decreased from 3.0M to 0.0006M.

5 Tables and Figures

Table I. Compositions of Ultrahigh-Strength Steels Used in Aerospace Applications*

Alloy	C	Ni	Co	Cr	Mo	Mn	Cu	V	Si	Al	Ti
4340	0.40	1.8	—	0.85	0.25	0.7	—	—	0.2	—	—
300M	0.40	1.8	—	0.85	0.4	0.7	—	0.1	1.6	—	—
HP9-4-20	0.20	9	4	0.8	1	0.1–0.3	—	0.08	0.2 max	—	—
HP9-4-30	0.30	9	4	1	1	0.15–0.3	—	0.08	0.1 max	—	—
HY180	0.10	10	8	2	1	0.15	—	—	—	—	—
AF1410	0.16	10	14	2	1	—	—	—	—	—	—
15-5PH	0.04	4.6	—	15	—	0.25	3.3	—	0.4	—	—
PH13-8	0.04	8	—	13	2.2	—	—	—	—	1.1	—
C250	0.005	18	8	—	4.8	—	—	—	—	0.1	0.4

* The Mn and Si levels are normally kept as low as possible in PH13-8, AF1410 and C250. 15-5PH contains Nb + Ta in proportion to the carbon content. All values are given in wt.%.

Table 1: Compositions of UHSSS used in aerospace applications, reproduced from Garrison 1990 [17].

Table II. Mechanical Properties of Ultrahigh-Strength Steels Used in Aerospace Applications

Alloy	YS (MPa)	UTS (MPa)	K_{Ic} MPa \sqrt{m}	K_{Isc}^* MPa \sqrt{m}
4340	1,482	1,965	71	11-16
300M	1,689	1,965	71	11-16
HP9-4-20	1,276	1,344	192	121
HP9-4-30	1,413	1,586	121	—
HY180	1,276	1,344	203	45
AF1410	1,551	1,689	187	45,71
15-5PH (vacuum melt)	1,089	1,124	132	132
PH13-8	1,434	1,551	81	>69
C-250	1,689	1,724	110	33

* The K_{Isc} data are for 1,000 hours in 3.5% NaCl in water. The K_{Isc} of AF1410 was given as 45 MPa \sqrt{m} by Tromans²⁸ but the material tested was produced much earlier than that used by Nue who reports 71 MPa \sqrt{m} . Both tests were for 1,000 hours. The K_{Isc} reported by Tromans²⁸ for HY180 is the same as he reported for AF1410; the HY180 tested was not modified by lanthanum, while the AF1410 very likely was.

Table 2: Mechanical properties of UHSSS used in aerospace applications, reproduced from Garrison 1990 [17].

Custom 465 Composition					
<i>Cr</i>	<i>Ni</i>	<i>Mo</i>	<i>Ti</i>	<i>C</i>	<i>Fe</i>
11.7	11.0	1.0	1.6	0.004	Balance

Table 3: Composition of Custom 465 as reported by Carpenter [30].

Custom 465 Typical Mechanical Properties					
σ_{ys} (MPa)	UTS (MPa)	R.A. (%)	E (GPa)	K_{IC} (MPa\sqrt{m})	Hardness (HRC)
1648	1765	57	193	95	49.5

Table 4: Mechanical properties of Custom 465-H950 reported by Carpenter [30].

Summary of Phase II Testing Parameters

<i>Test ID</i>	<i>Environment (ICF)</i>	<i>Exposure Condition</i>	<i>Pre-Fatigue Polarization (mV_{SCE})</i>	<i>Pre-Fatigue Polarization Time (hr)</i>	<i>Fatigue Polarization (mV_{SCE})</i>	<i>Note</i>
1	Humid N ₂	1	-	-	-	
2	-	1	-	-	-	No test
3	Humid N ₂	1	-	-	-	
4	Humid N ₂	1	-	-	-	
5	Humid N ₂	1	-	-	-	
6	Humid N ₂	1	-	-	-	
7	0.6	2	-200	24	-200	
8	0.6	2	-200	24	-200	
9	0.6	2	-200	24	-200	
10	1.5	2	-200	24	-200	
11	3	2	-200	24	-200	
12	0.6	2	150	0.25	-200	
13	0.6	3	150	36	-200	
14	-	-	-	-	-	No test
15	0.6	3	150	36	-200	
16	0.6	3	150	48	-200	
17	0.6	4	-	-	-200	
18	0.6	4	-	-	-200	
19	0.6	4	-	-	-200	
20	0.6	4	-	-	-200	
21	0.6	4	-	-	-200	
22	0.6	4	-	-	-200	
23	0.6	4	-	-	-200	
24	1.5	4	-	-	-200	
25	1.5	4	-	-	-200	
26	3	4	-	-	-200	
27	3	4	-	-	-200	
28	0.06	4	-	-	-200	
29	0.06	4	-	-	-200	
30	0.006	4	-	-	-200	
31	0.006	4	-	-	-200	
32	0.0006	4	-	-	-200	
33	0.0006	4	-	-	-200	
34	0.0001	4	-	-	-	
35	0.0001	4	-	-	-	
36	3	3	150	48(0.67)	-200	Adj. Pol.
37	3	3	150	48 (0.5)	-200	Adj. Pol.
38	3	2	-	0	-200	
39	3	3	150	12 (0.25)	-200	Adj. Pol.

Table 5: Phase II exposure condition and polarization parameters are listed here. “Adj. Pol.” denotes pre-fatigue polarizations that had to be truncated. Test 2 and 14 did not produce any data.

Deviations in Decreasing K Tests					
[Cl] (M)	E (mV)	ΔK (MPa\sqrt{m})	da/dN (mm/cycle)	Plateau da/dN (mm/cycle)	da/dt (mm/s)
0.6	-200	6.5	7.49E-05	7.45E-05	1.49E-04
0.6	-550	8.27	1.70E-05	3.32E-05	6.64E-05
0.6	-200	9.82	3.73E-05	7.49E-05	1.50E-04
1.5	-200	10.56	6.84E-05	7.08E-05	1.42E-04
0	-200	12.3	1.71E-04	1.21E-03	2.42E-03

Table 6: Conditions at which decreasing- ΔK da/dN deviates from linear behavior.

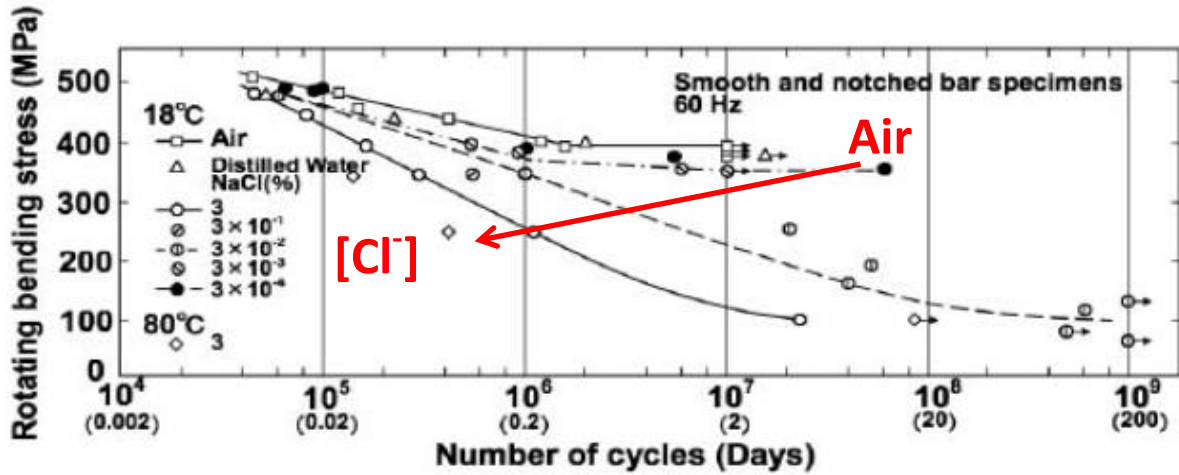


Figure 1: Research by Hata shows that UHSSS exposure to aqueous chloride environments may decrease fatigue life of UHSSS (in this case a 13%Cr SUS410JI). Reproduced from Hata 2008 [6].

Corrosion and Oxidation

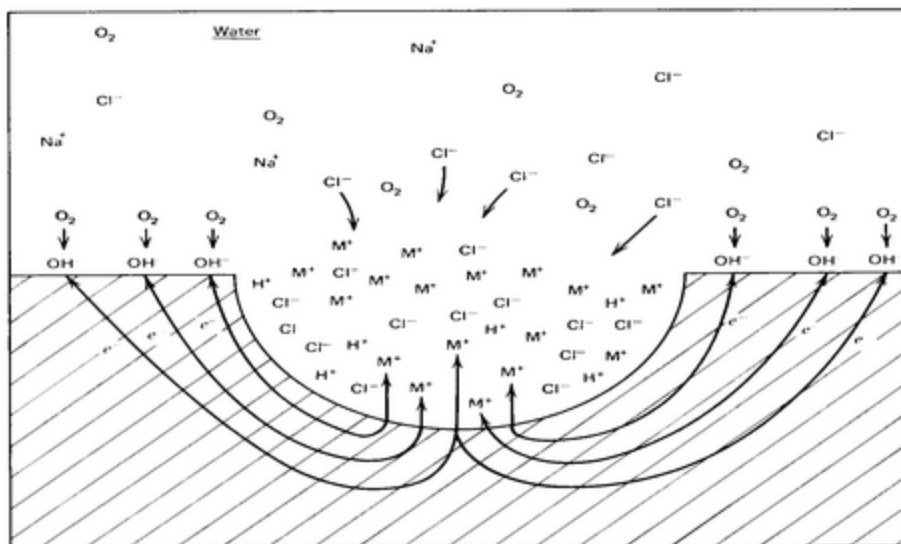


Figure 2: A typical representation of autocatalytic pit growth in a sodium chloride aqueous solution. Oxygen is depleted towards the base of the pit, and diffusion of oxygen through solution is too sluggish to maintain aeration of solution at the base of the pit. The tip of the pit acidifies as the base metal hydrolyzes to form metal hydroxides. Chloride anions migrate into the pit to neutralize the inorganic imbalance from the formation of positively charged metal hydroxides. Reproduced from Fontana, 2005 [150].

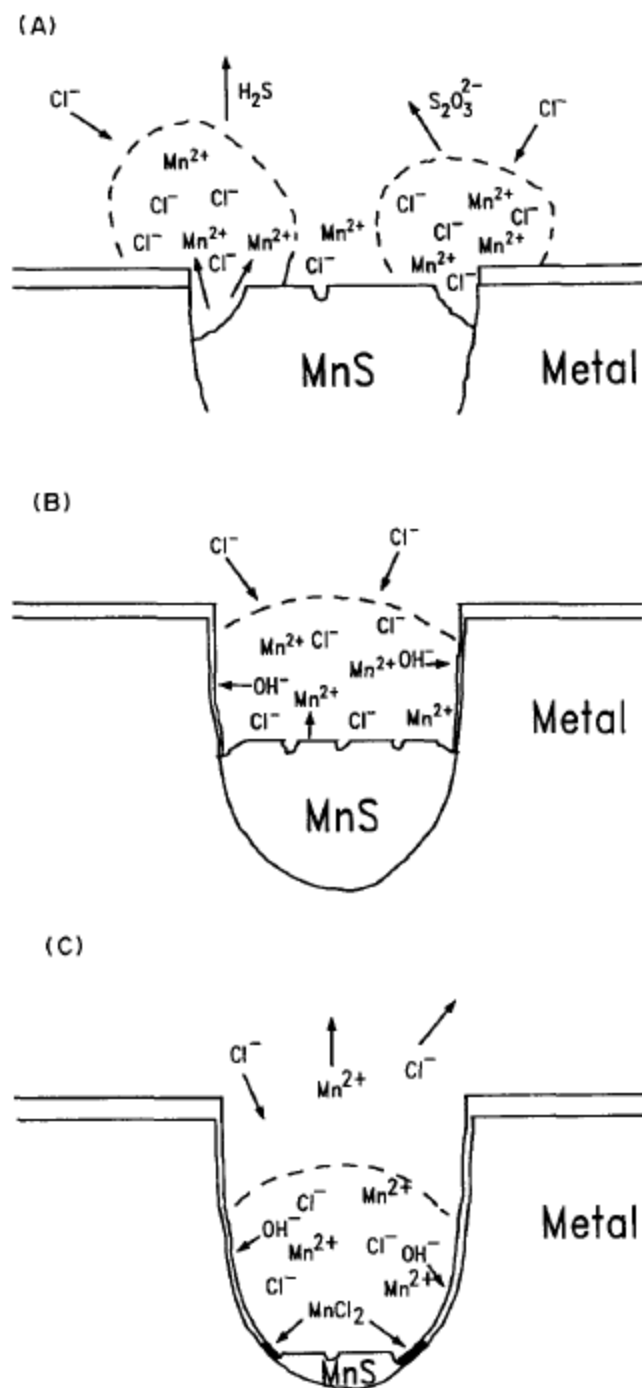


FIG. 10. A proposed model for pit initiati

Figure 3: Proposed mechanism of pitting at an MnS inclusion in steels. Reproduced from Baker 1993 [49].

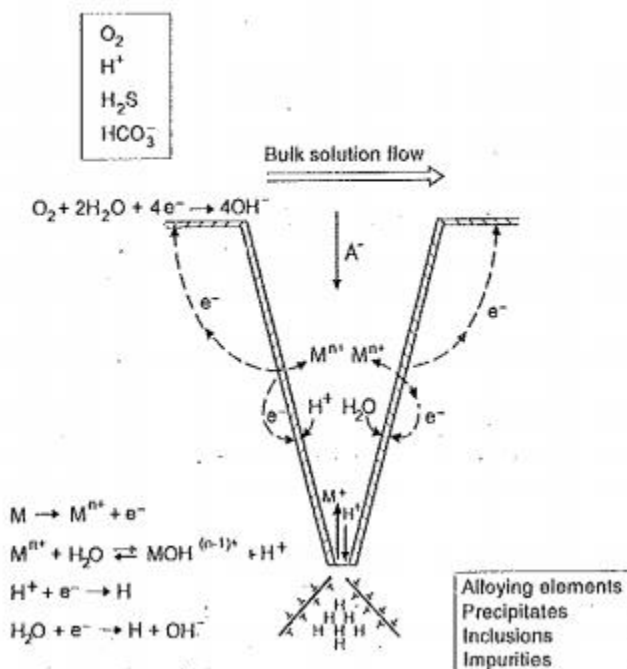


Figure 4: Electrochemical reactions in an immersed crack. Electrochemical reactions both at the crack tip and along the crack walls create an aggressive chemistry that may occlude the crack tip from the bulk solution. Figure reproduced from Turnbull 2001 [151].

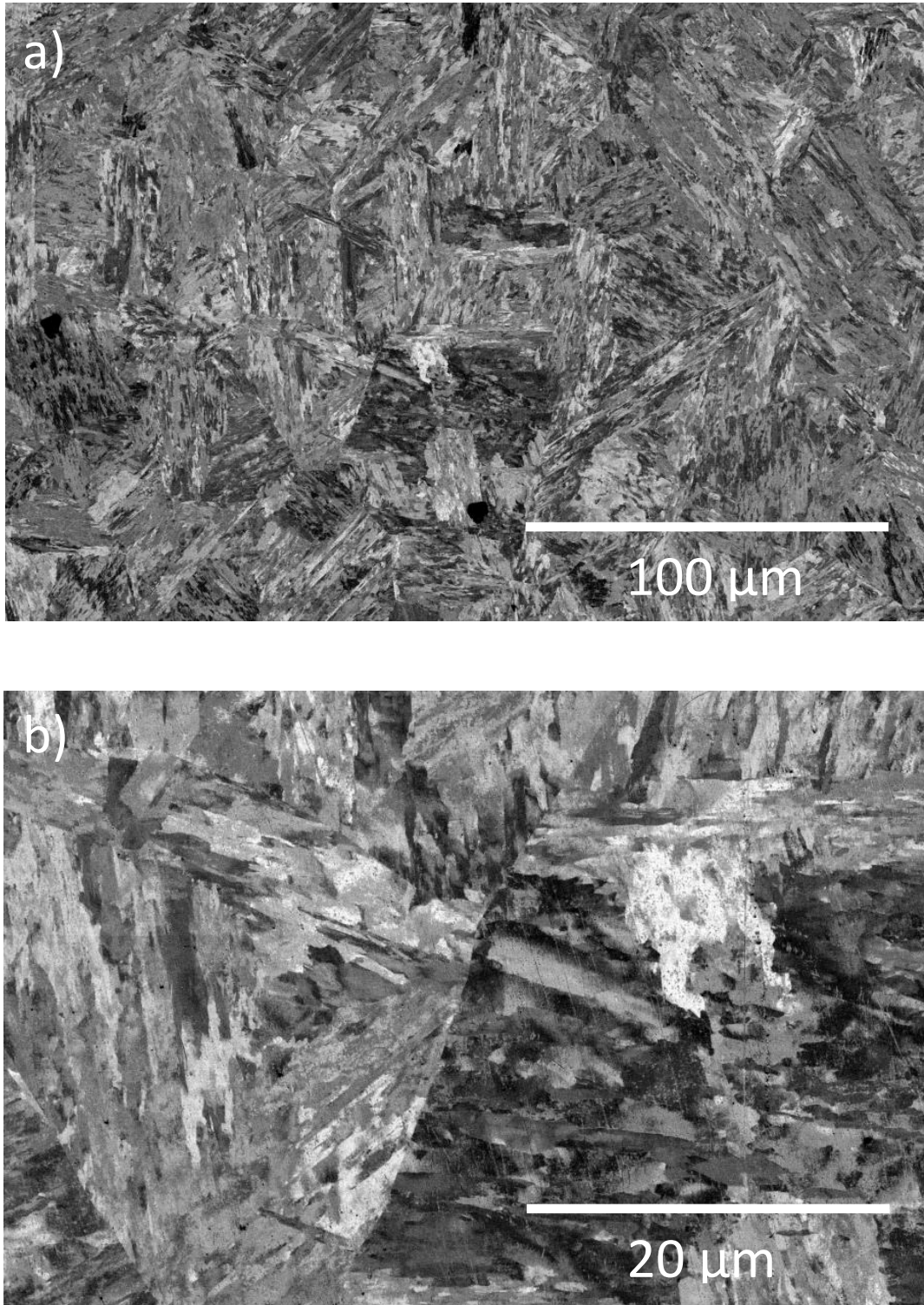


Figure 5: Low (a) and high (b) magnification SEM backscatter electron images of polished C465-H950 (working distance=1-2mm, positive stage bias).

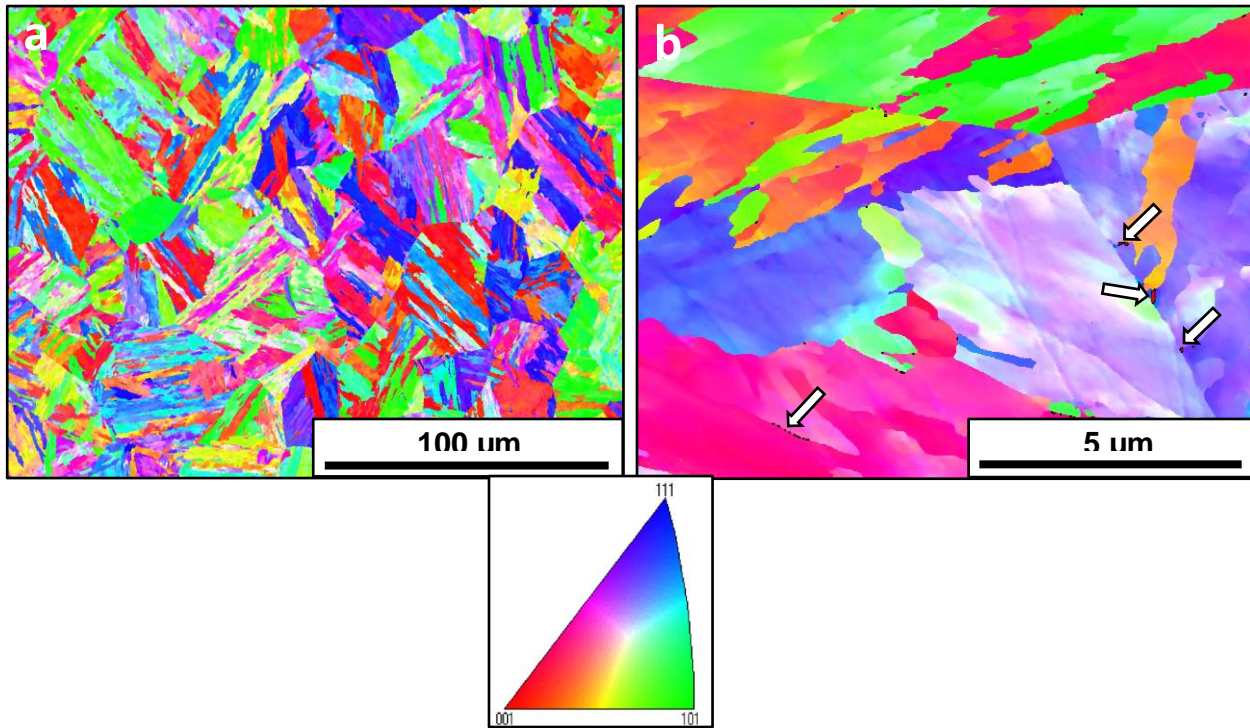


Figure 6: Electron backscatter diffraction (EBSD) orientation maps of Custom465. Small (50-250 nm) islands of retained austenite are denoted by white arrows. Low magnification maps (a) were obtained using a step size of 250 and 200 nm, respectively. High magnification maps (b) were obtained using a step size of 12 nm. Reproduced from Pioszazk 2013 [115].

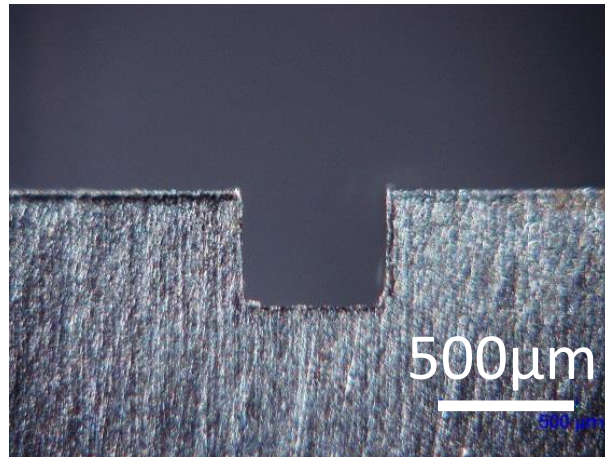


Figure 8: Optical micrograph side view of the square notch.

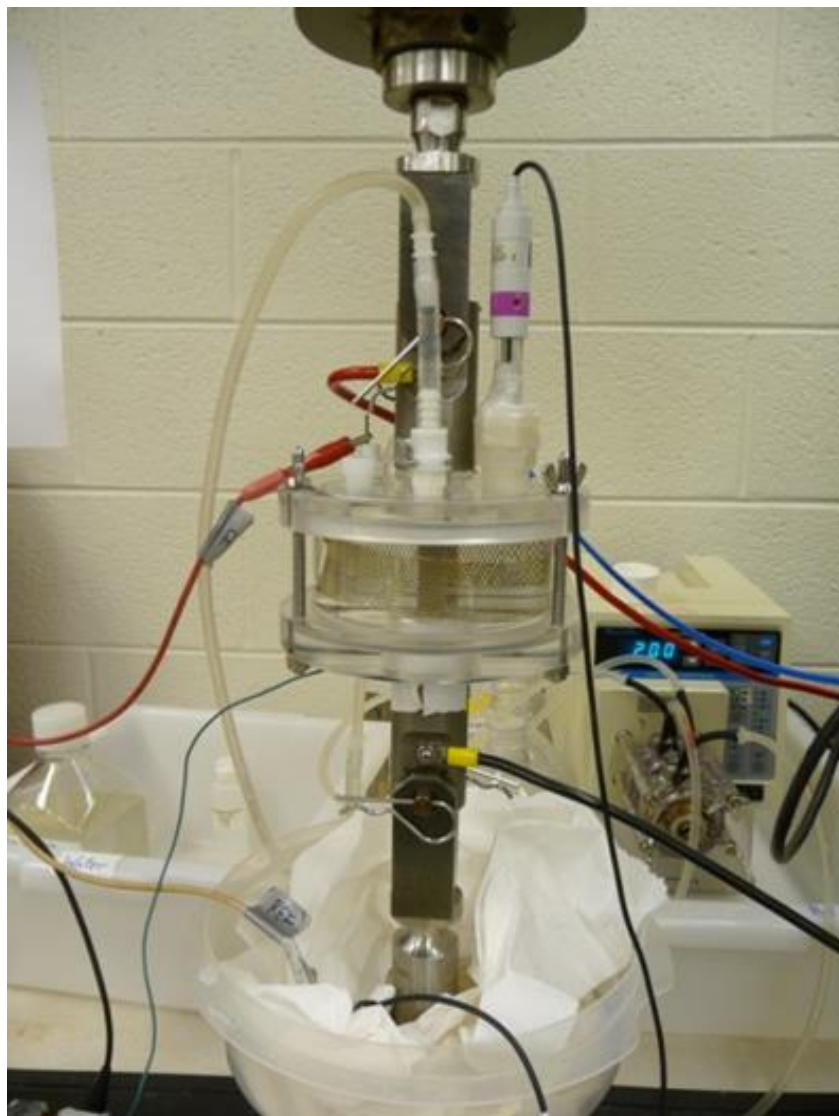


Figure 9: In Phase I, the specimen is loaded into a 360mL Plexiglas cell, loaded into a test frame and connected to a potentiostat.

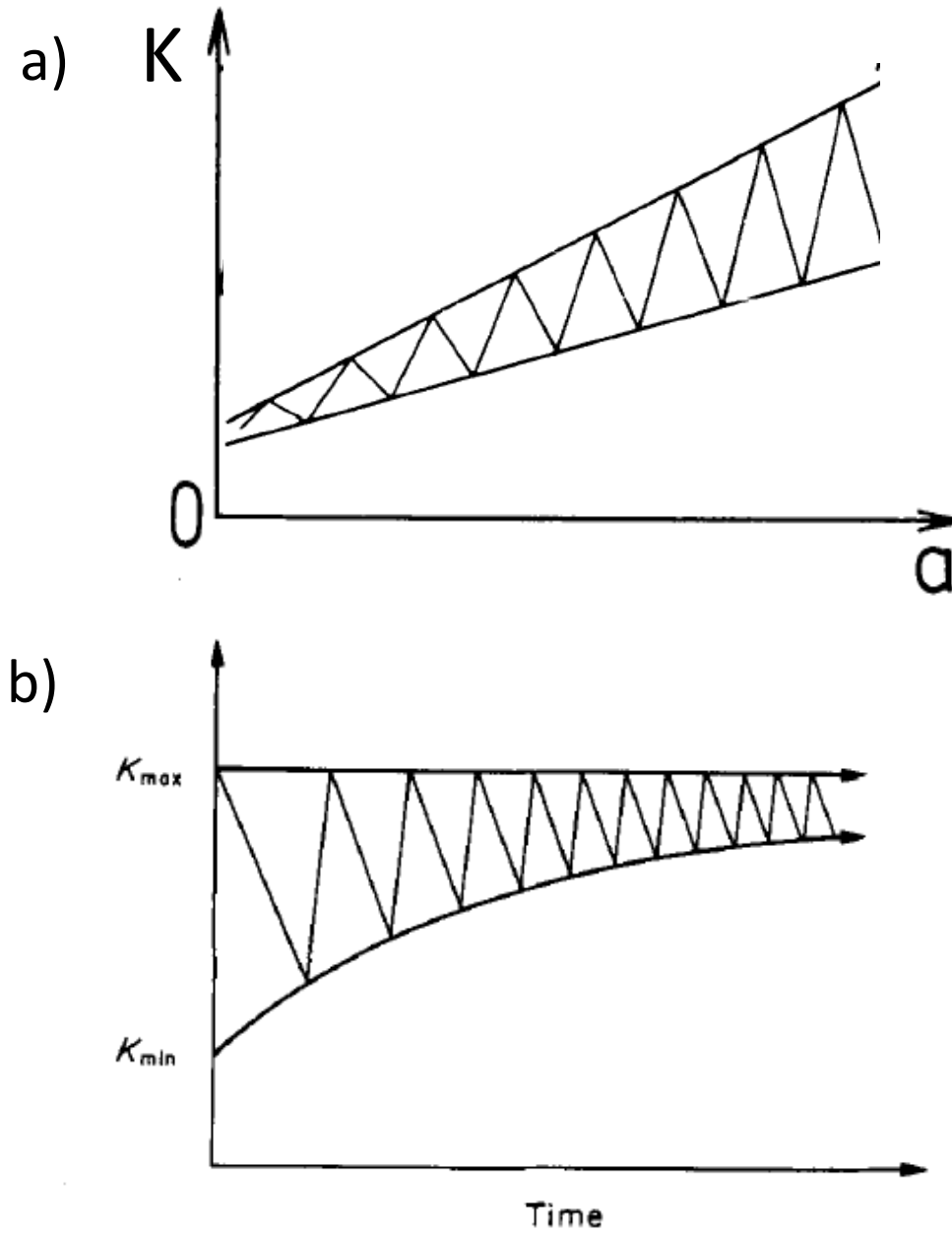


Figure 10: General representation of the wave forms used for the increasing- K (a) and decreasing- K (b) Phase I fatigue tests. Reproduced from Herman, 1988 [127].

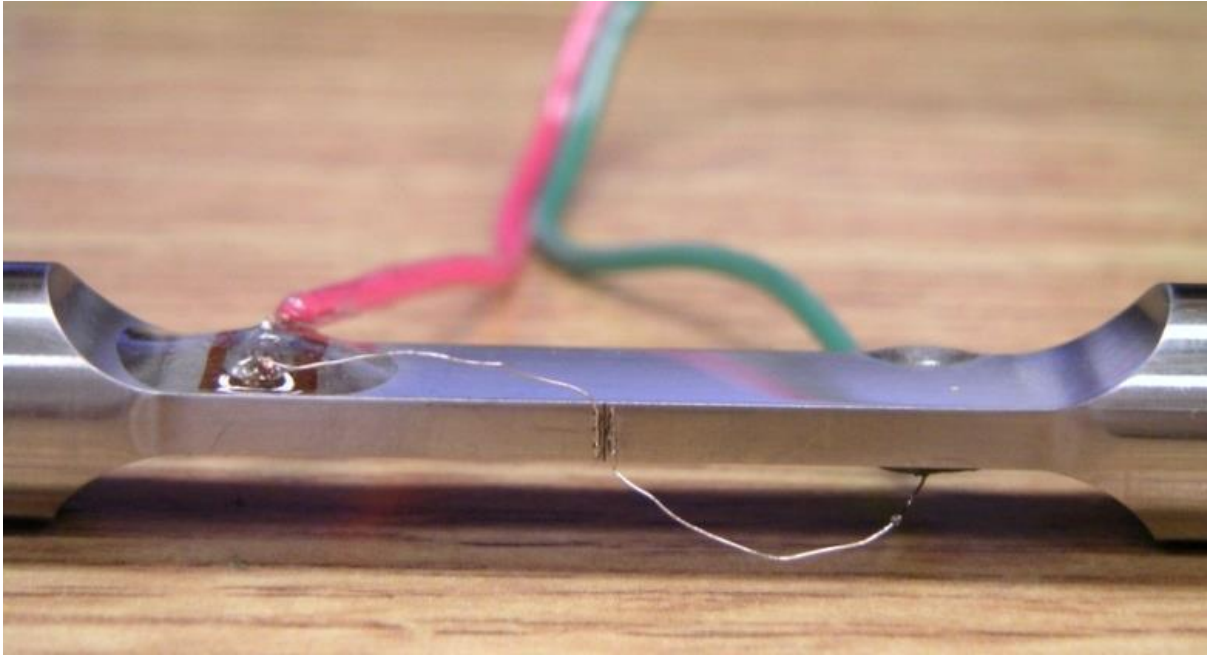


Figure 11: Wires are spot-welded close to the notch to collect dcPD measurements. Exposed sections of the wire were coated in stop off lacquer to prevent corrosion of the electrical leads.

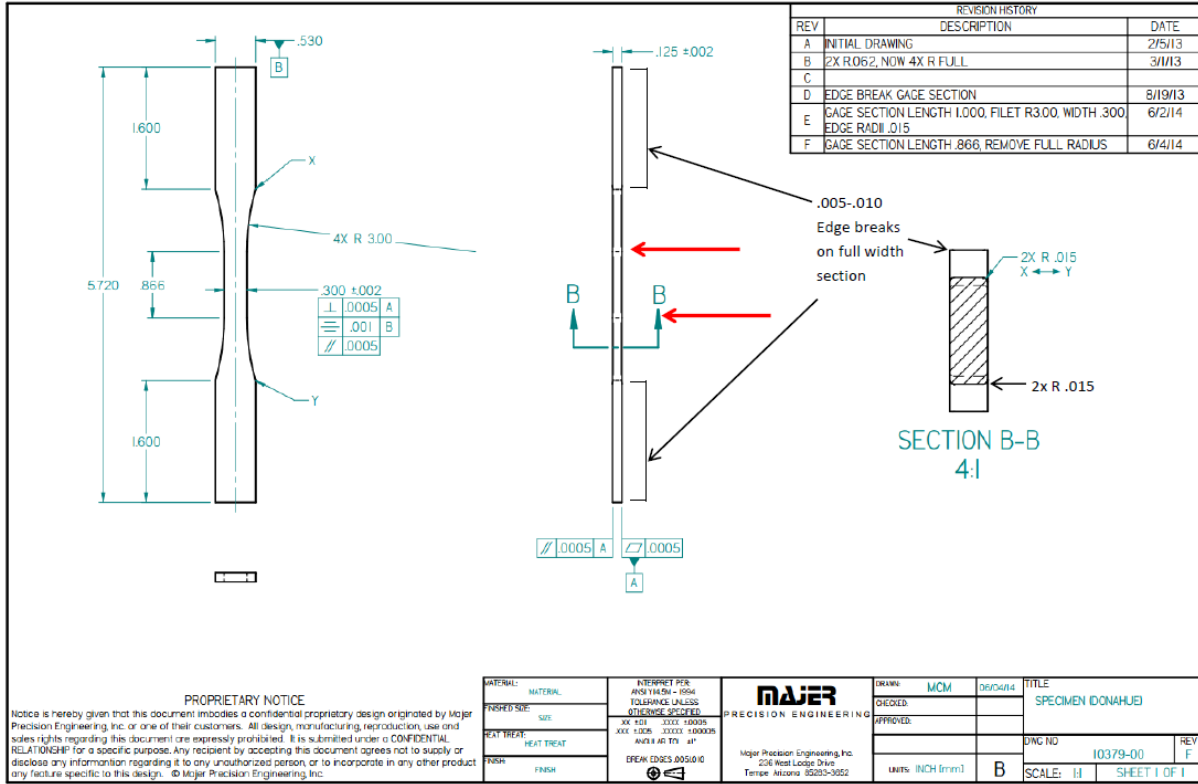


Figure 12: Schematic detailing the Phase II dog-bone specimen design.



Figure 13: In Phase II, the dog-bone specimen is loaded into a 500mL Plexiglas cell, loaded into a test frame and connected to a potentiostat.

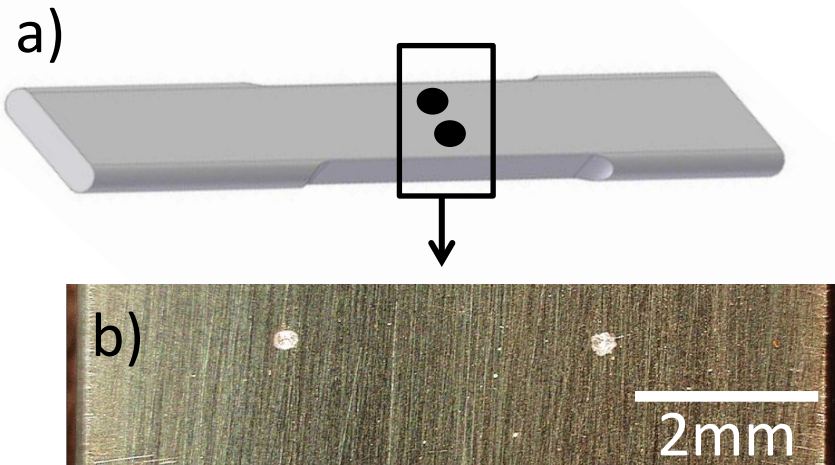
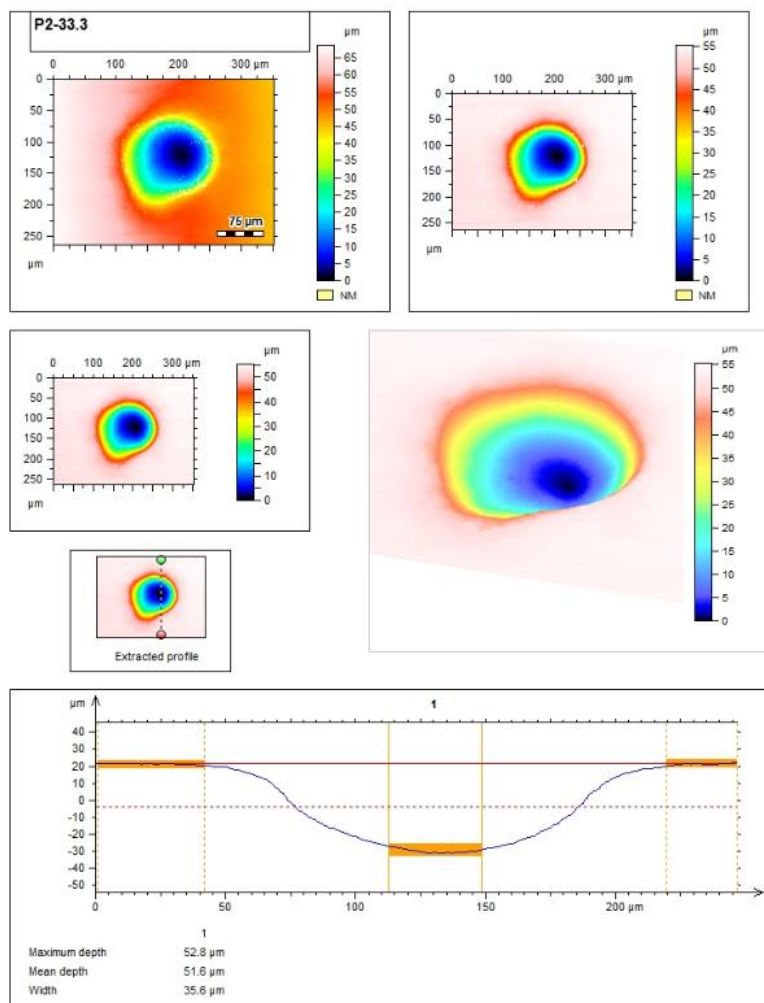


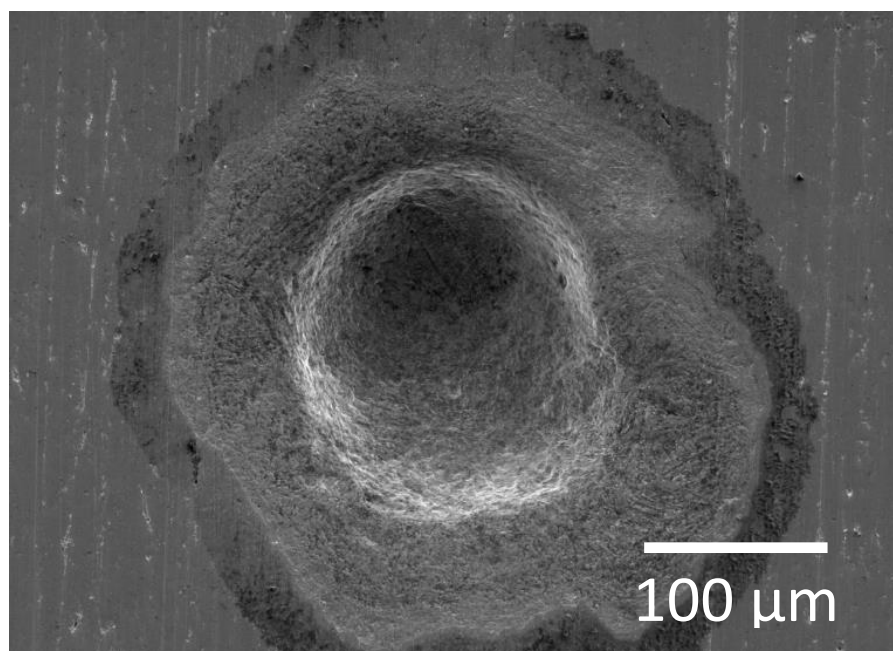
Figure 14: This figure explains the placement of Condition 4 pits on a Phase II fatigue specimen. (a) A basic rendering showing pit placement (black dots) on one side of a fatigue specimen. The hidden side has an identical arrangement of pits. (b) An optical image showing pit placement on an actual specimen.

a)

Figure 15: An overview of pre-fatigue pit characterization and analysis via white light interferometry is presented in (a). The operations shown are a fraction of potential analyses. (b) shows an SEM secondary electron image of the same pit.



b)



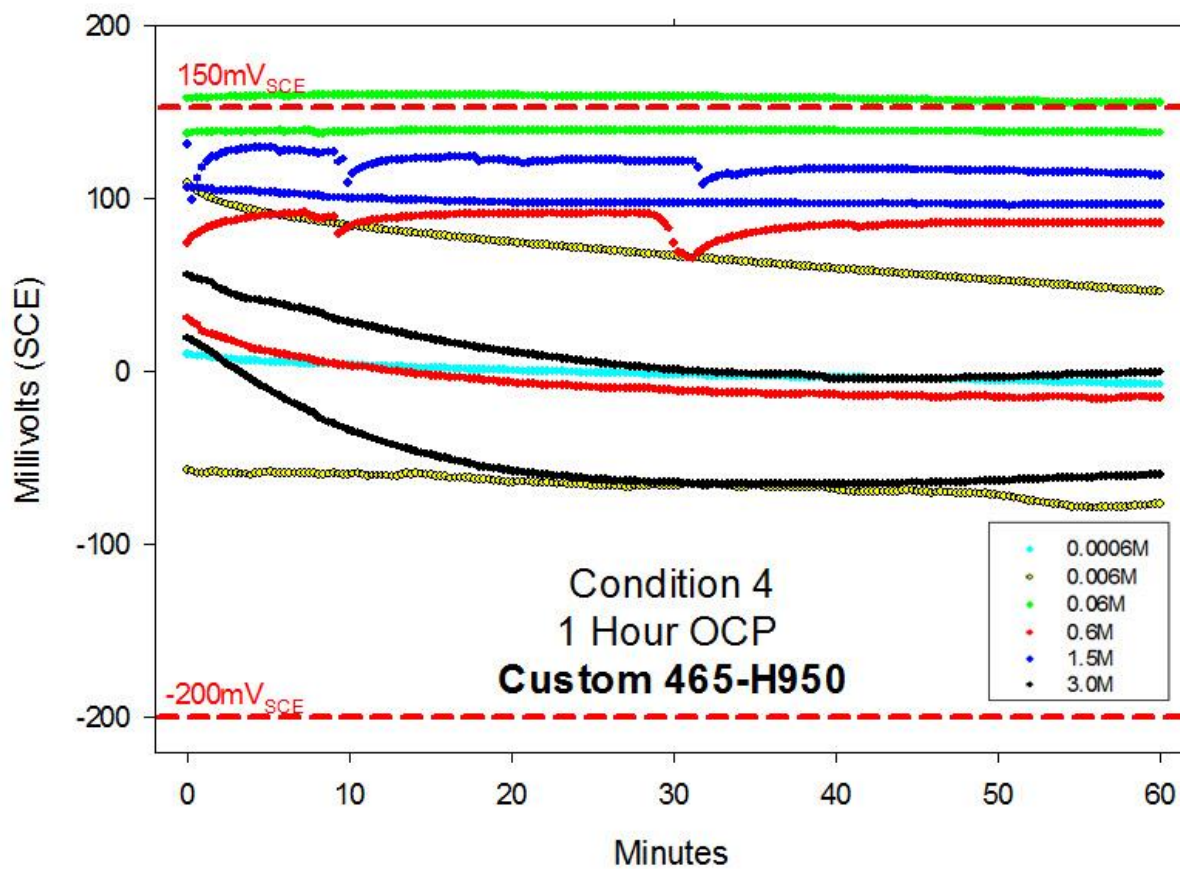


Figure 16: OCP measurements taken 1 hour prior to fatigue from Condition 4 specimens in various NaCl environments.

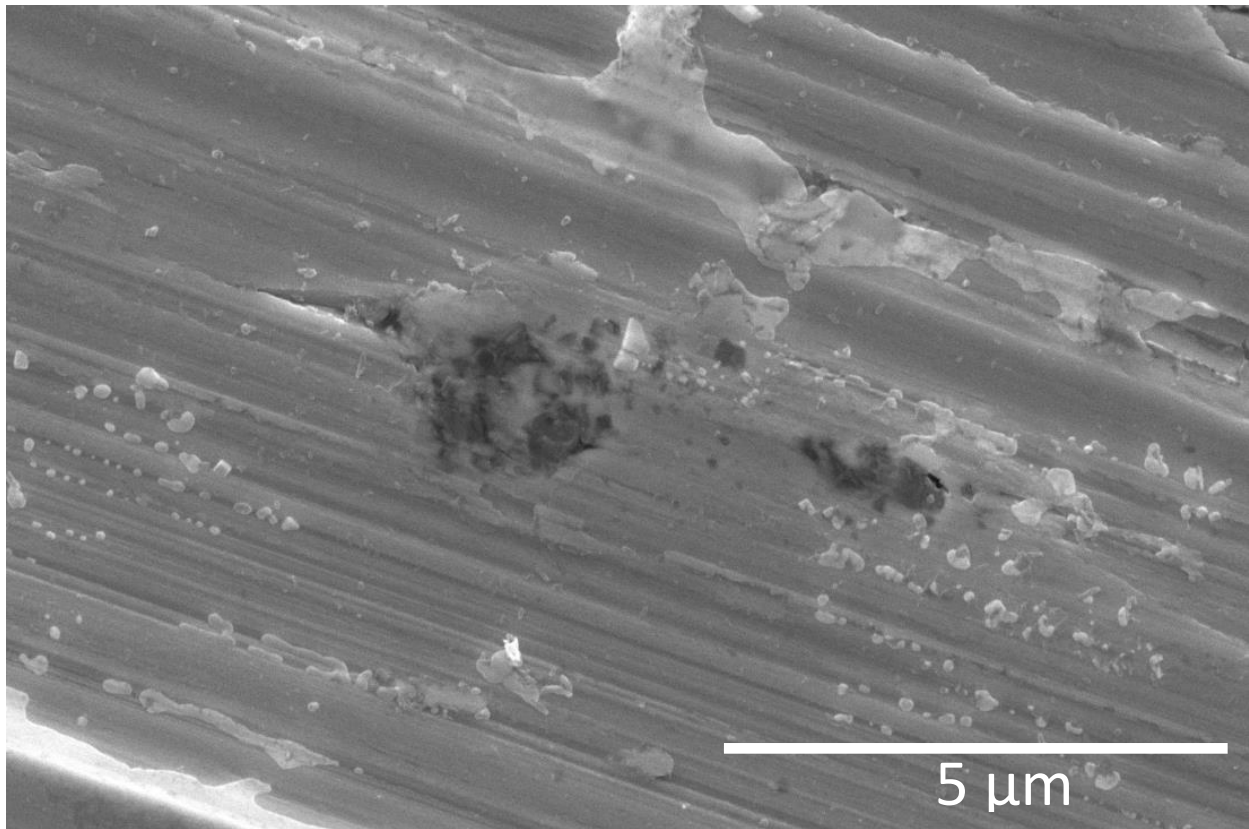


Figure 17: Example of corrosion damage in C465 after 1 year of full immersion in 0.6M NaCl. The feature shown is less than 2 μ m in diameter and lacks significant depth.

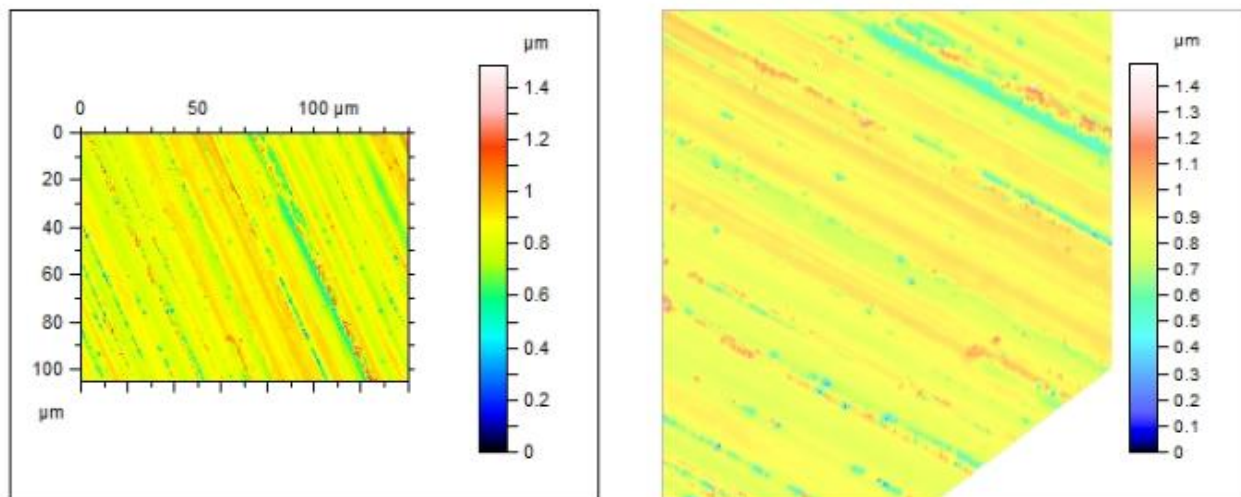


Figure 18: Polished C465 electrode after 36 hours of polarization at $150\text{mV}_{\text{SCE}}$ in a 0.6M NaCl solution. Pits litter the polished surface and measure less than $1\mu\text{m}$ in all dimensions.

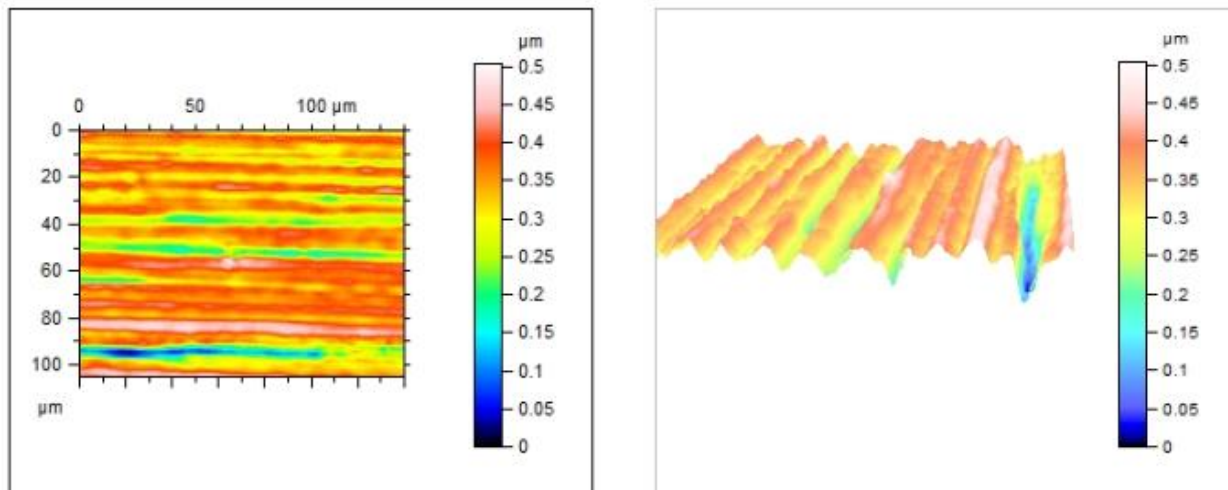


Figure 19: Profilometry of the surface of a C465-H950 electrode post-polish obtained via white light interferometry.

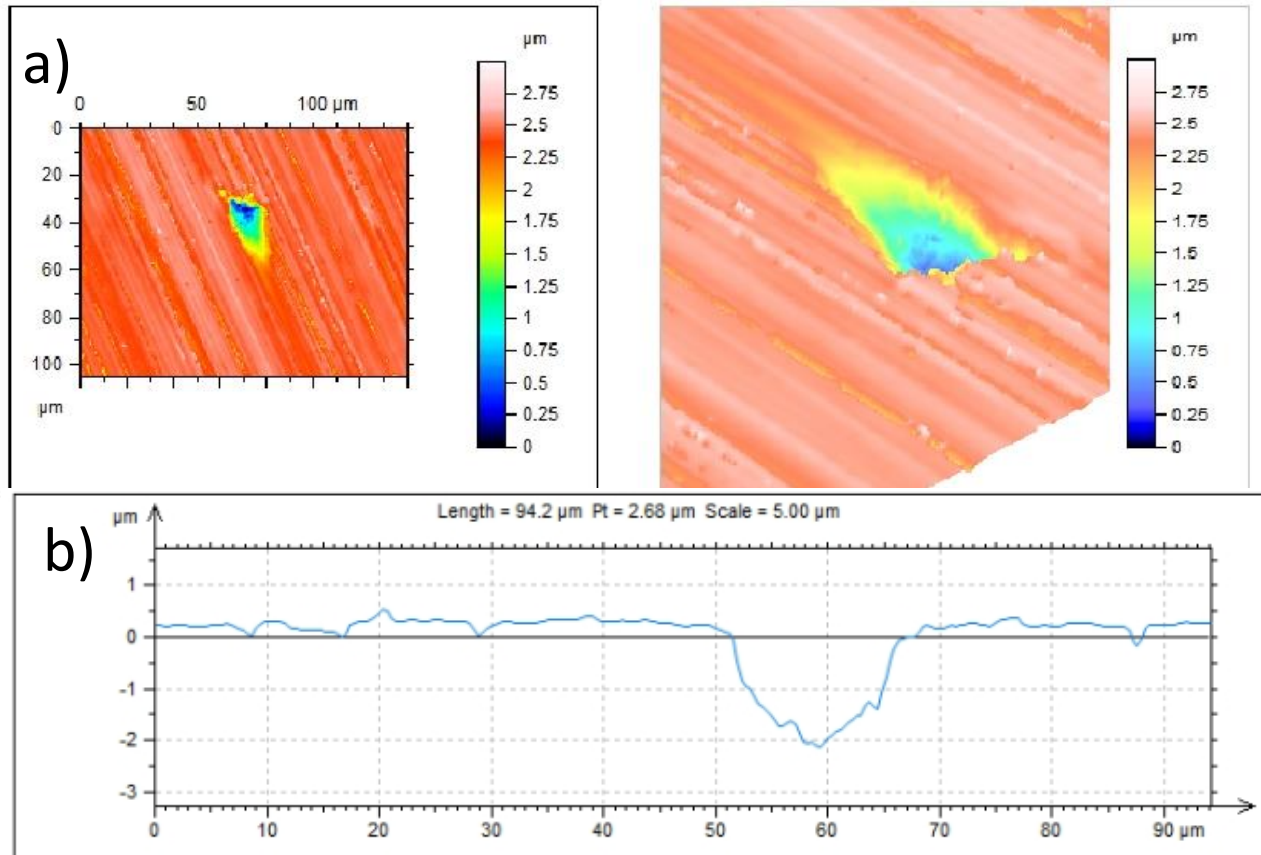


Figure 20: This is an example of a larger flaw generated by the Condition 3 exposure with a 3D rendering provided in (a) and a cross-sectional profile provided in (b).

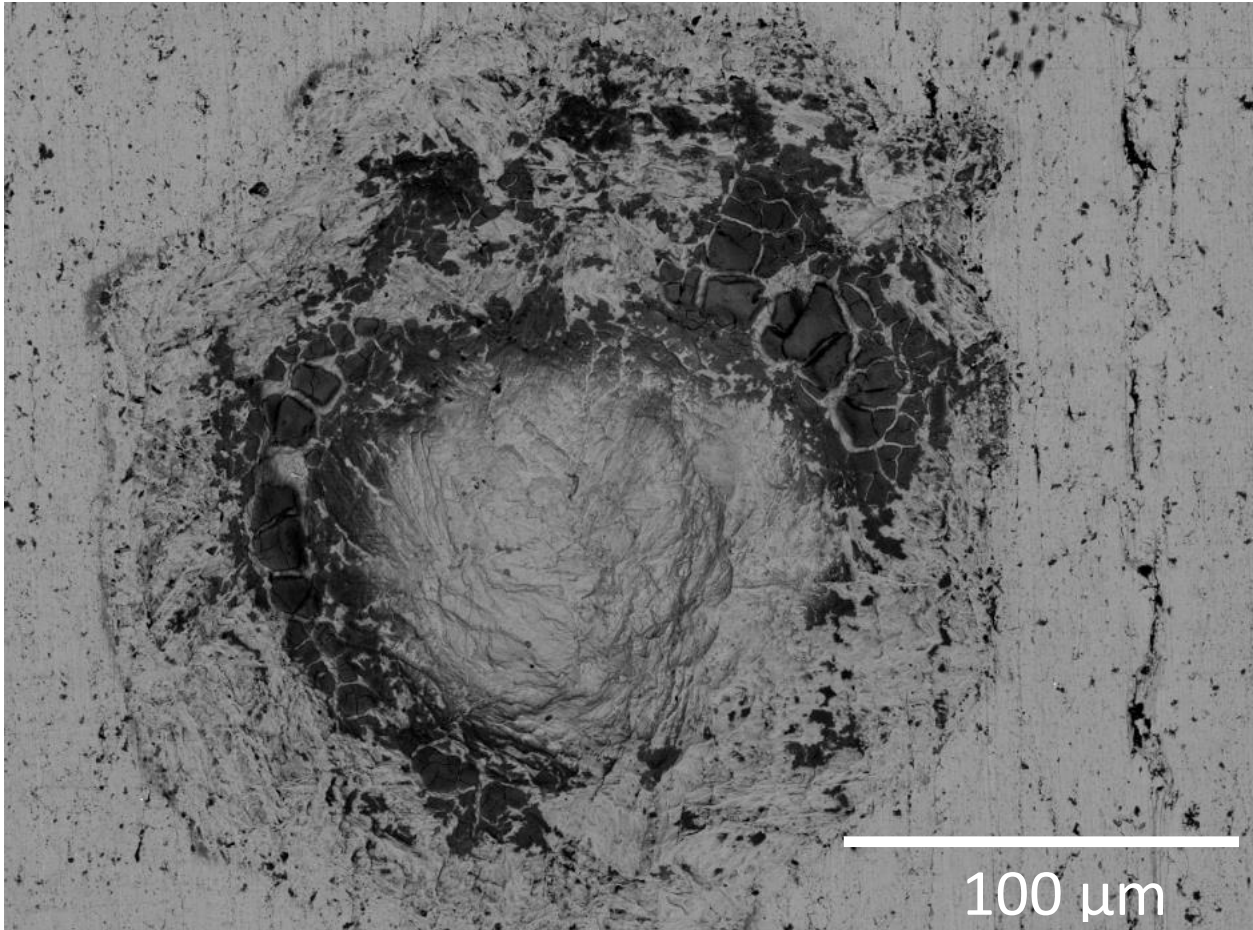


Figure 21: Backscatter electron image of a Condition 4 pit prior to cleaning. The dark phases are primarily chromium-oxides, validated by EDS.

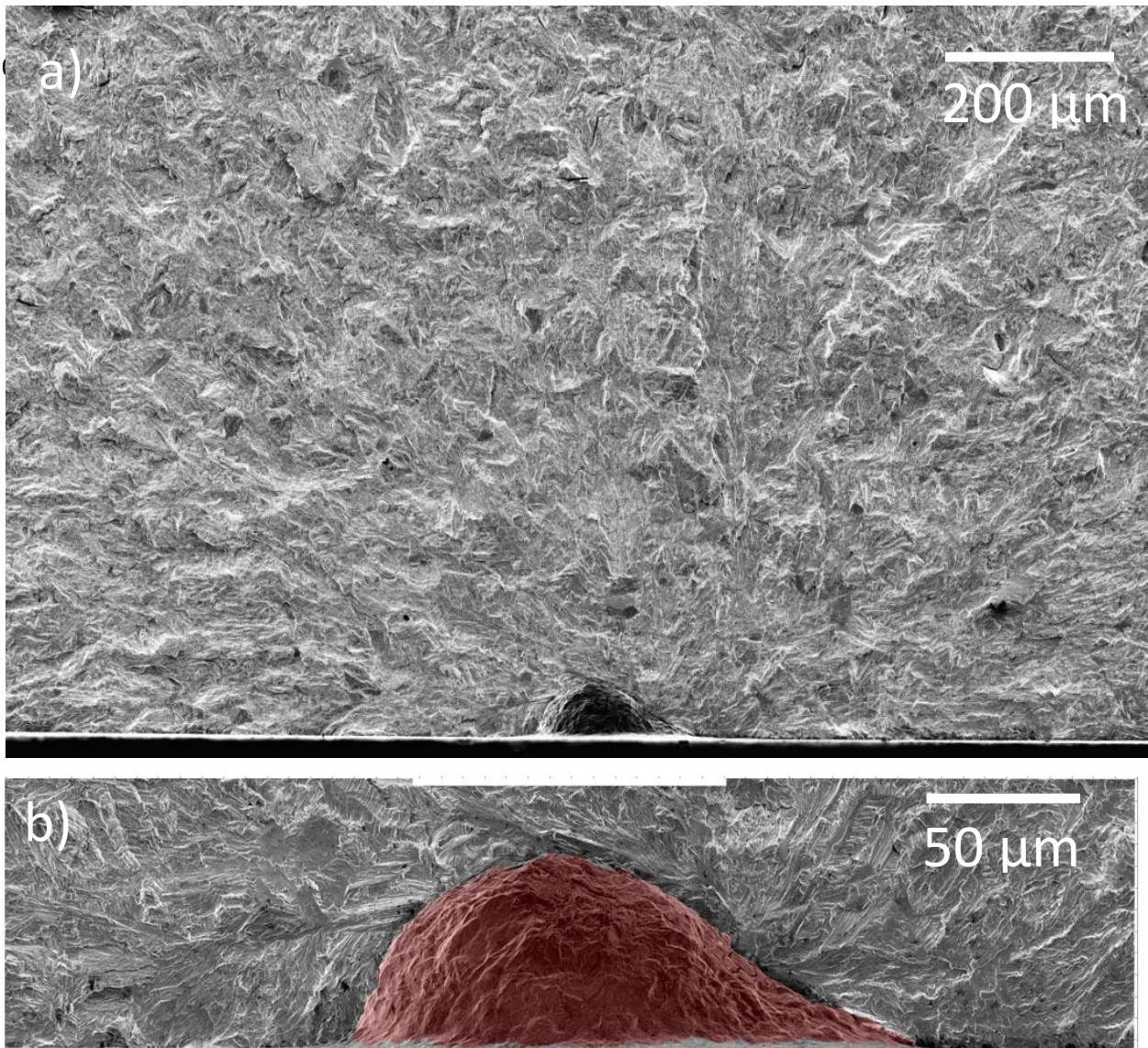


Figure 22: Low (a) and high (b) magnification images of the cross-section of a pit typical of the Condition 4 exposure. The red highlighting indicates the body of the pit.

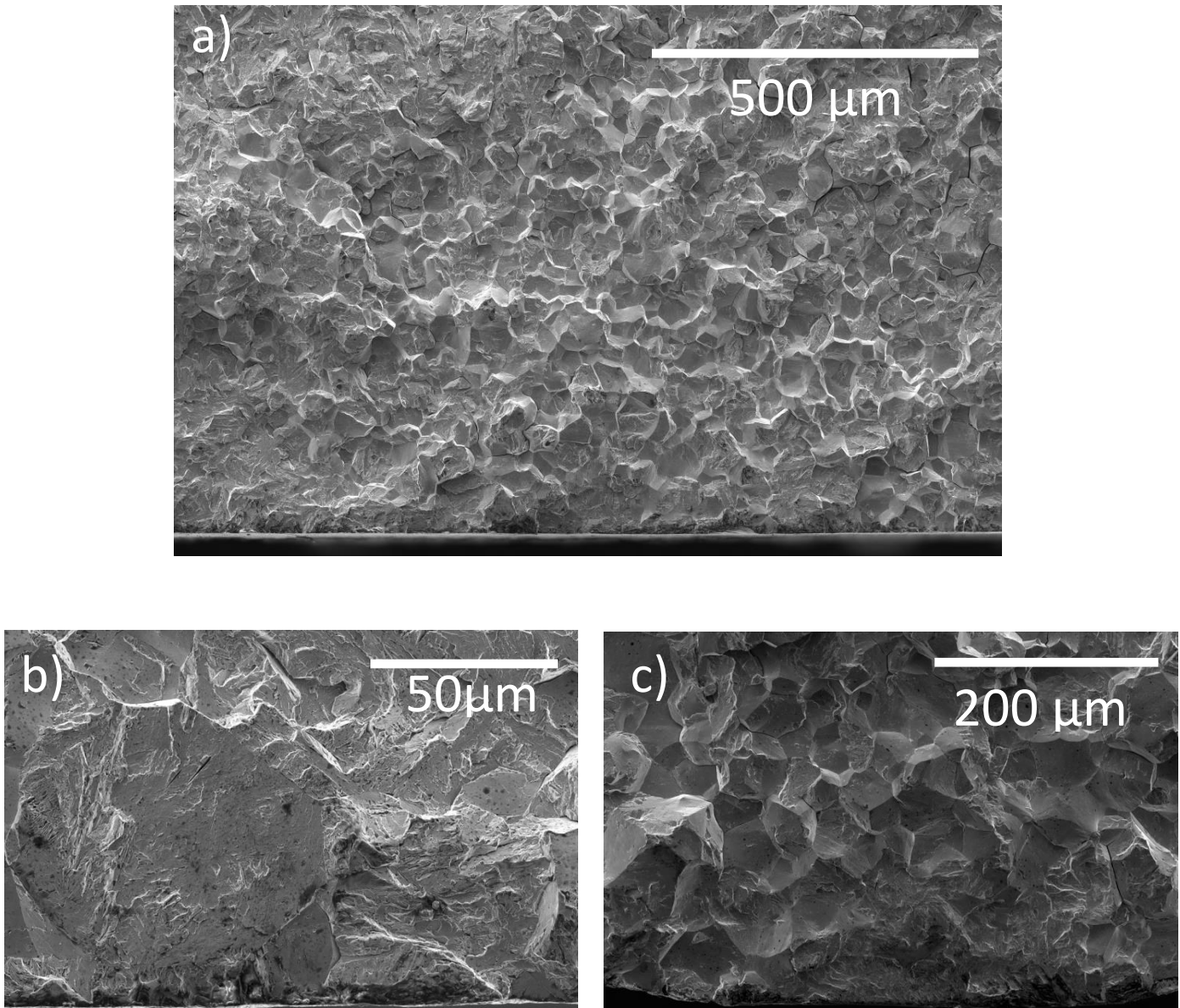


Figure 24: Micrographs of C465-H950 of polished dog-bone specimen fatigued in humid N_2 at an $R=0.5$, $f=2$, and a maximum stress of 1153MPa. (a) contains an overview micrograph of the fracture surface proximate to the initiation site of polished dog-bone specimens fatigued in humid N_2 . Grain(s) immediately about the initiation site are cleaved (b), but intergranular fracture dominates past this point and continues for several hundred micrometers (c).

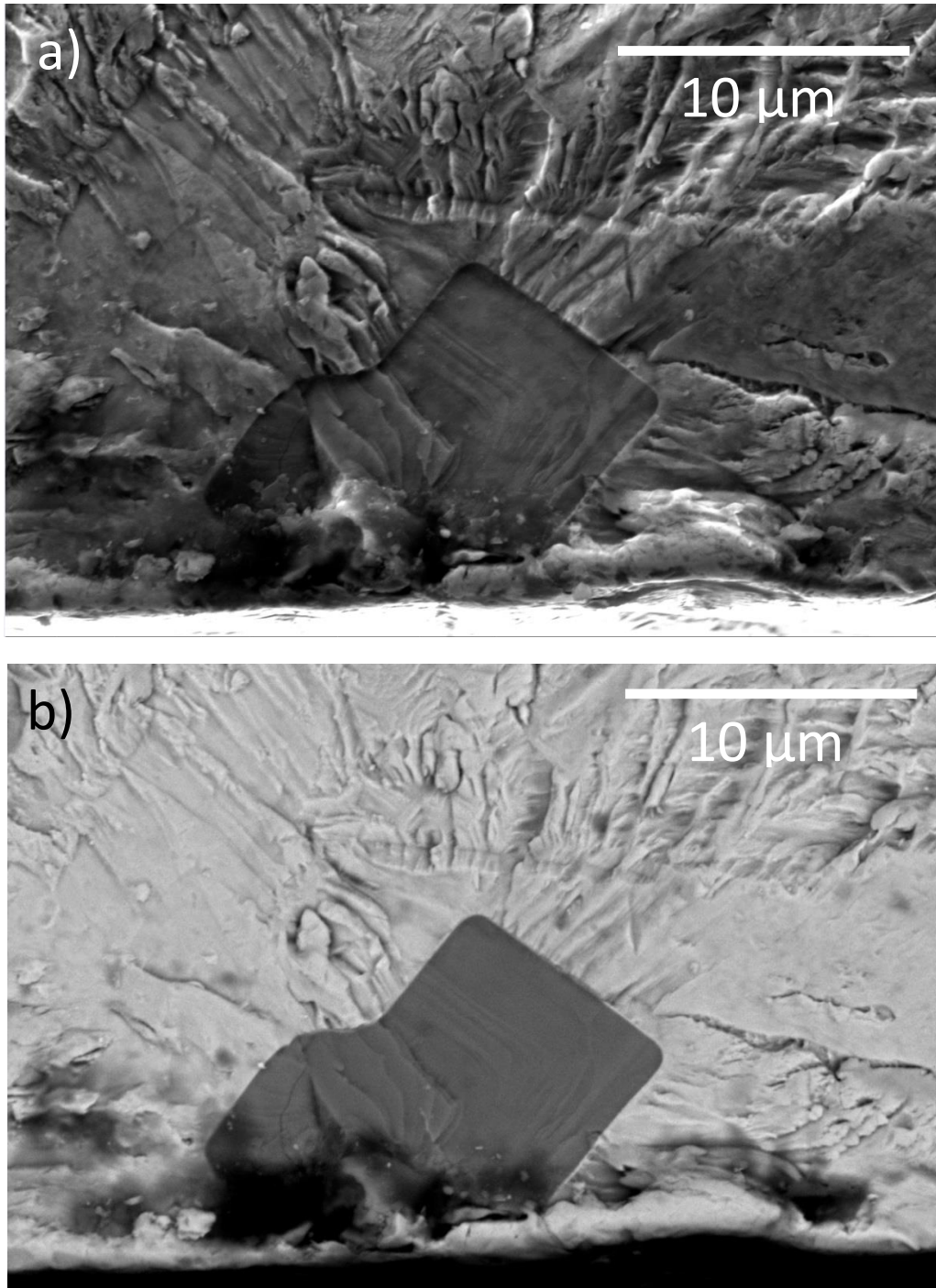


Figure 25: Initiation site of a Condition 2 dog-bone specimen polarized to $-200\text{mV}_{\text{SCE}}$ for 24 hours prior to fatigue. Fatigue was conducted at an $R=0.5$, $f=2$, and a maximum stress of 1153 MPa. Secondary electron (a) and backscatter electron (b) micrographs of a typical TiC inclusion responsible for crack nucleation.

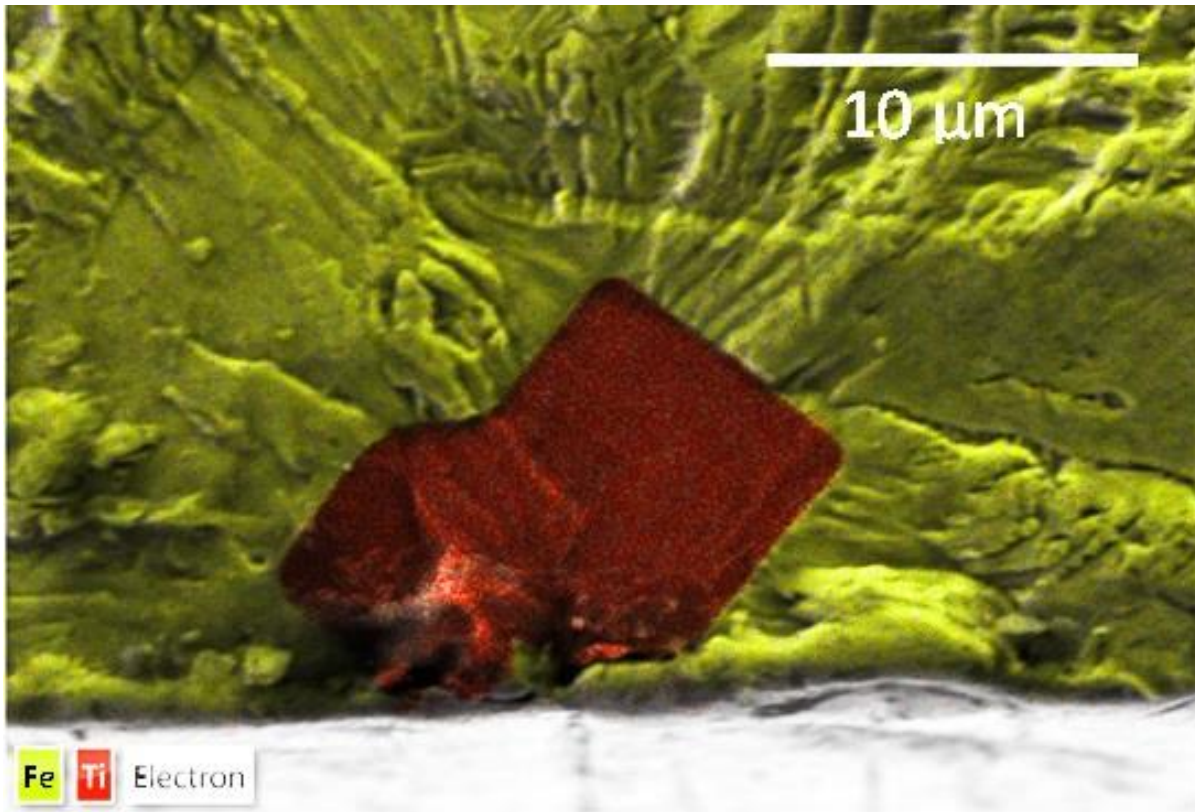
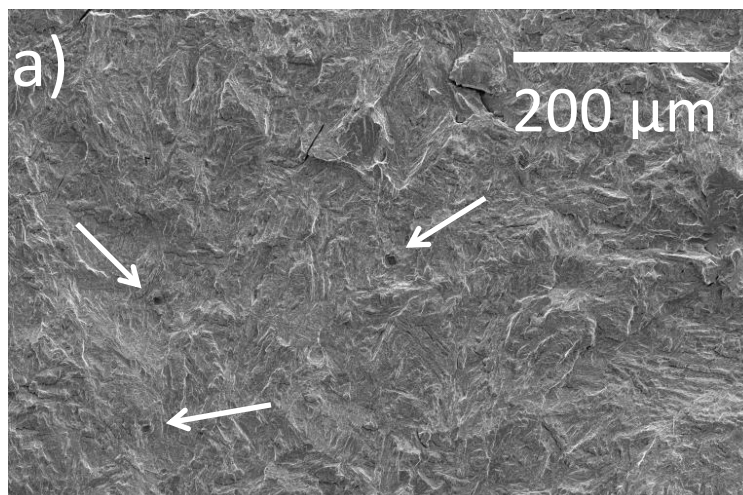


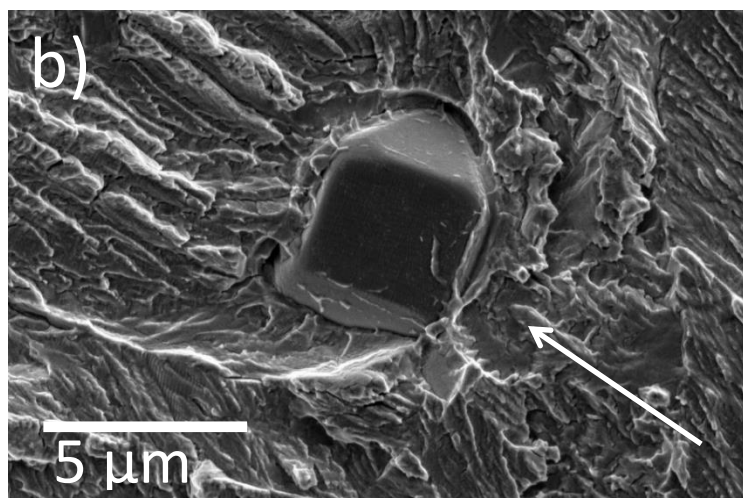
Figure 26: This EDS image of the TiC particle (red) shows that it is a secondary phase inclusion distinct from the matrix. This is the same inclusion as seen in Figure 25.

Figure 27: These secondary and backscatter electron micrographs exemplify titanium carbide inclusions observed in the path of the crack. This Condition 2 specimen was polarized to $-200\text{mV}_{\text{SCE}}$ for 24 hours prior to fatigue. Fatigue was conducted at an $R=0.5$, $f=2$, and a maximum stress of 1153 MPa.

a) A distribution of TiC on the fracture surface. Each white arrow marks a single carbide.

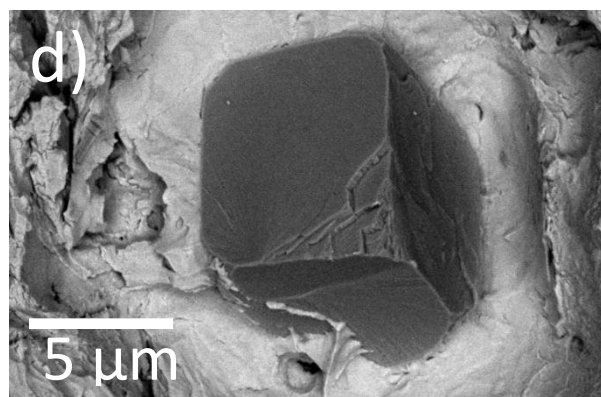
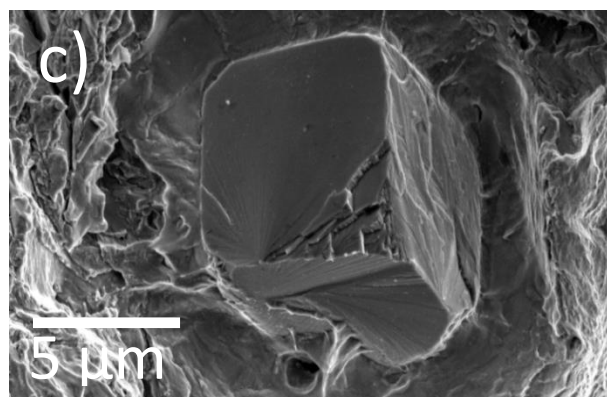


b) TiC found in the fracture surface are sometimes left intact, like the one pictured, or completely sheared in two in a brittle manner. The white arrow indicates the direction of crack growth.



c) Another mostly intact TiC particle protruding from the fracture surface.

d) Backscatter image of (c) clearly distinguishing the inclusion from the homogenous microstructure.



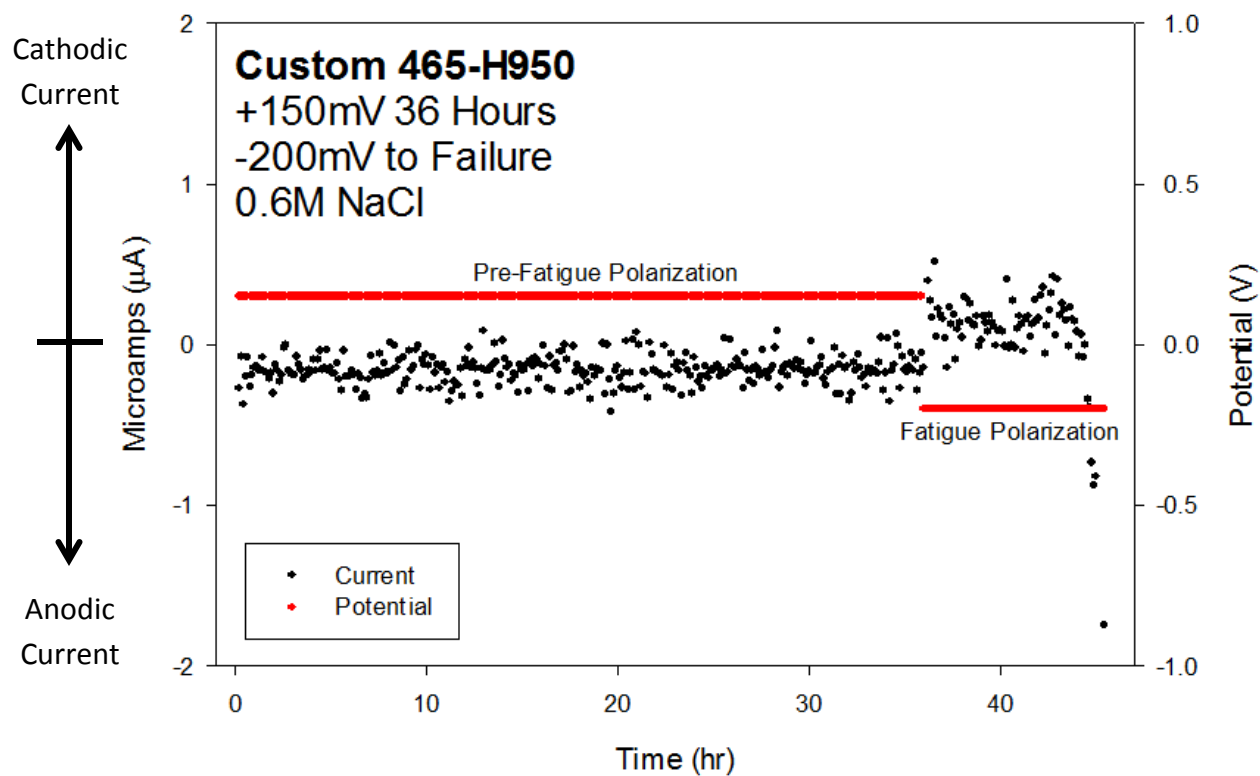


Figure 28: Typical current flow associated with pre-fatigue and fatigue polarizations of 150mV_{SCE} and -200mV_{SCE} respectively in 0.6M NaCl.

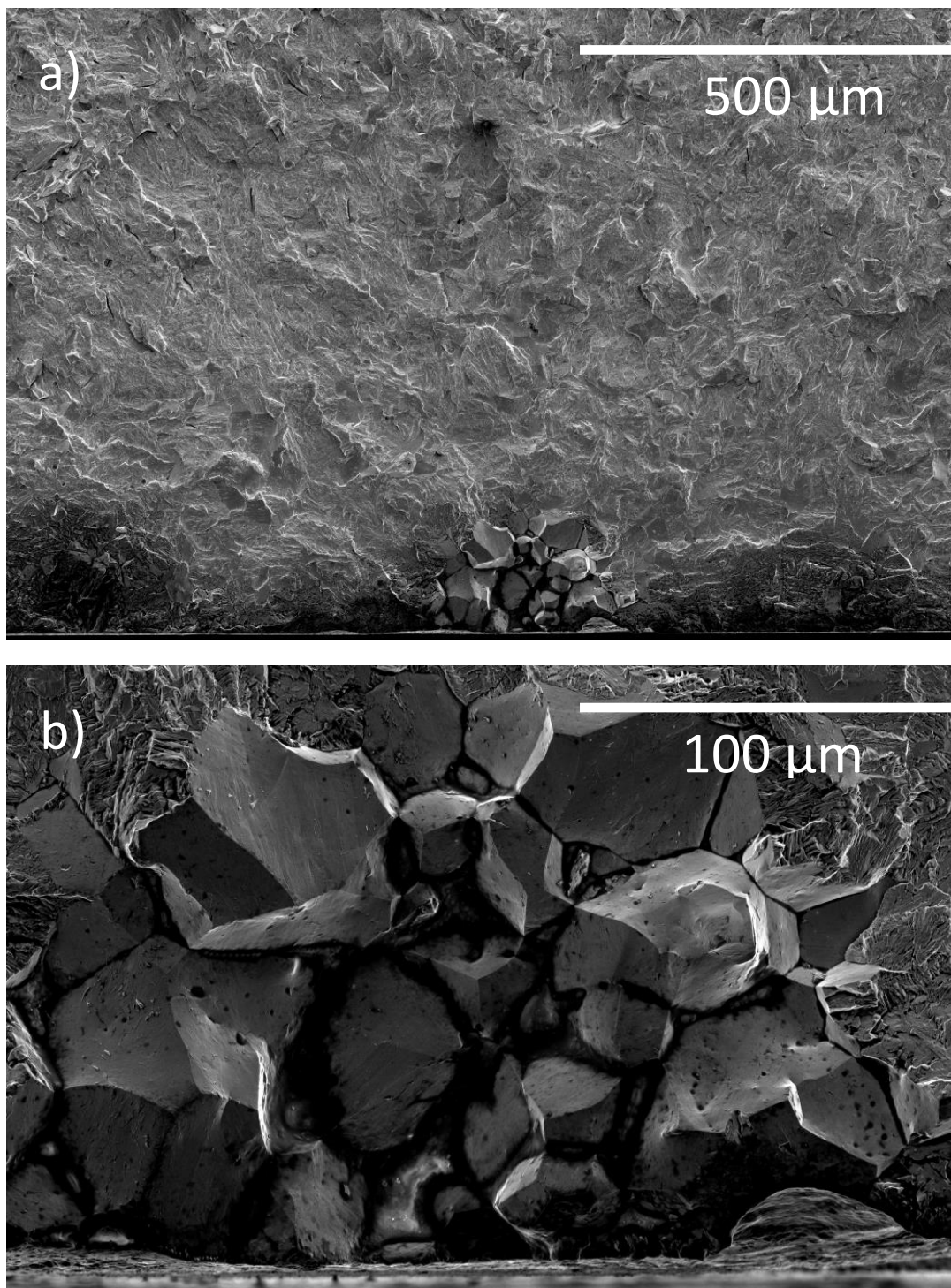


Figure 29: Low magnification (a) and high magnification (b) SEM image of a Condition 3 specimen polarized to $100\text{mV}_{\text{SCE}}$ for 15 minutes prior to fatigue. Fatigue was conducted at an $R=0.5$, $f=2$, and a maximum stress of 1153 MPa.

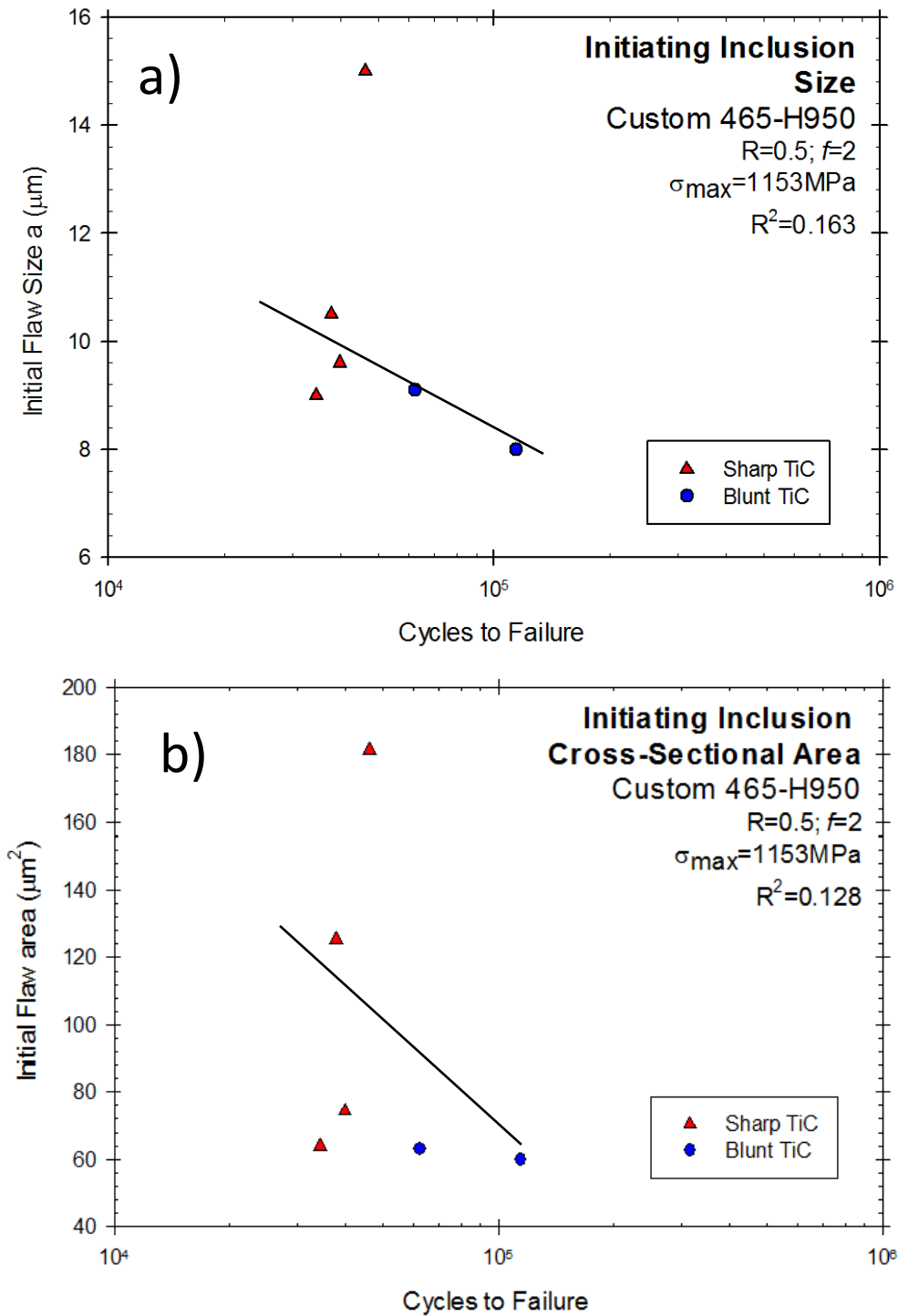


Figure 30: These plots contain all Condition 2 and 3 specimens initiating on a TiC particle. Fatigue was conducted at an $R=0.5$, $f=2$, and a maximum stress of 1153 MPa. Fatigue life is plotted against TiC depth into microstructure (a) and 2D cross-sectional area (b).

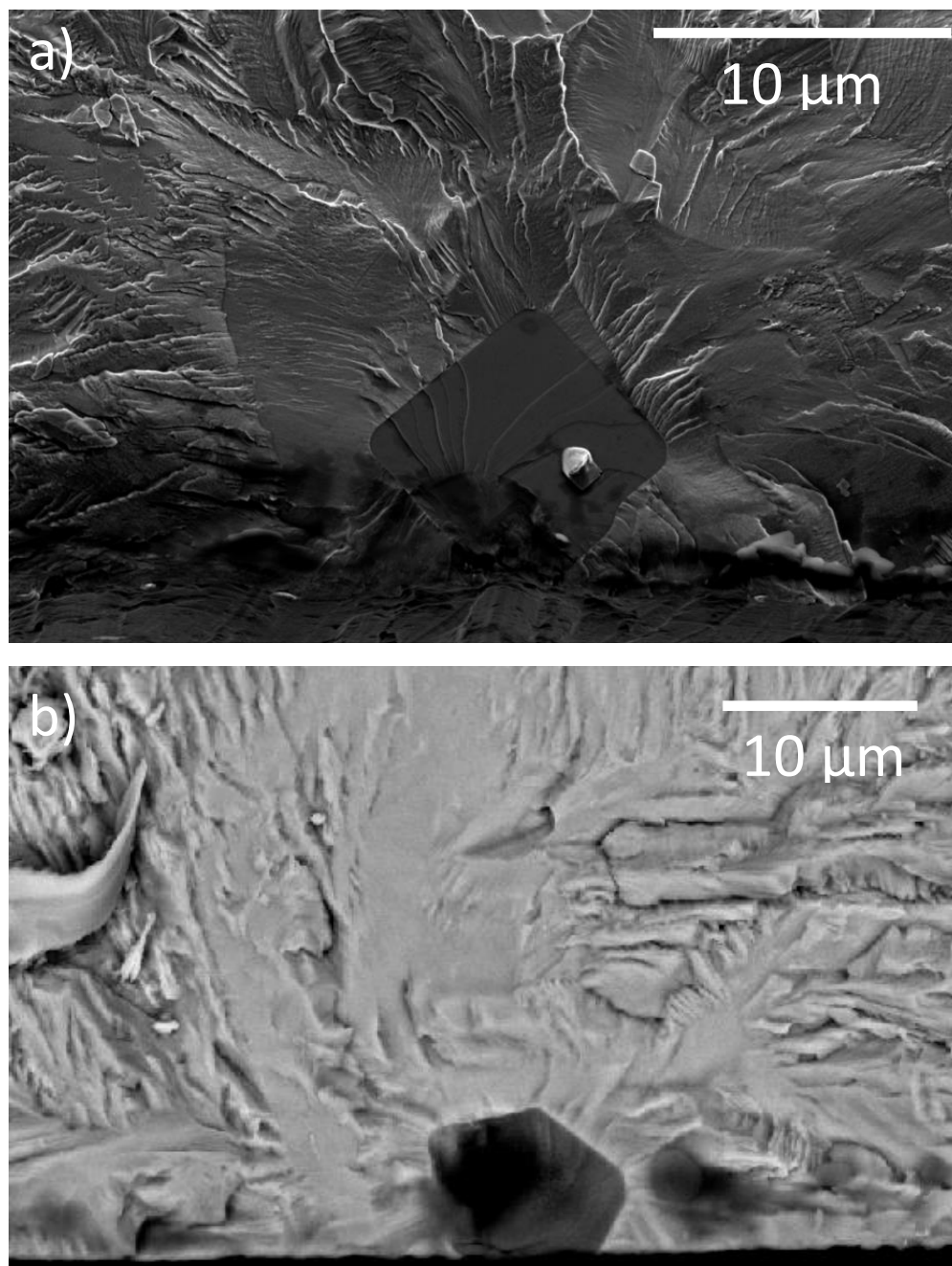


Figure 31: Micrograph of initiating TiC particles from a Condition 2 specimen polarized to $-200\text{mV}_{\text{SCE}}$ for 24 hours prior to fatigue. Fatigue was conducted at an $R=0.5$, $f=2$, and a maximum stress of 1153 MPa. A TiC inclusion with a sharp edge protruding into the matrix is seen in (a) and a more blunt TiC inclusion is seen in (b).

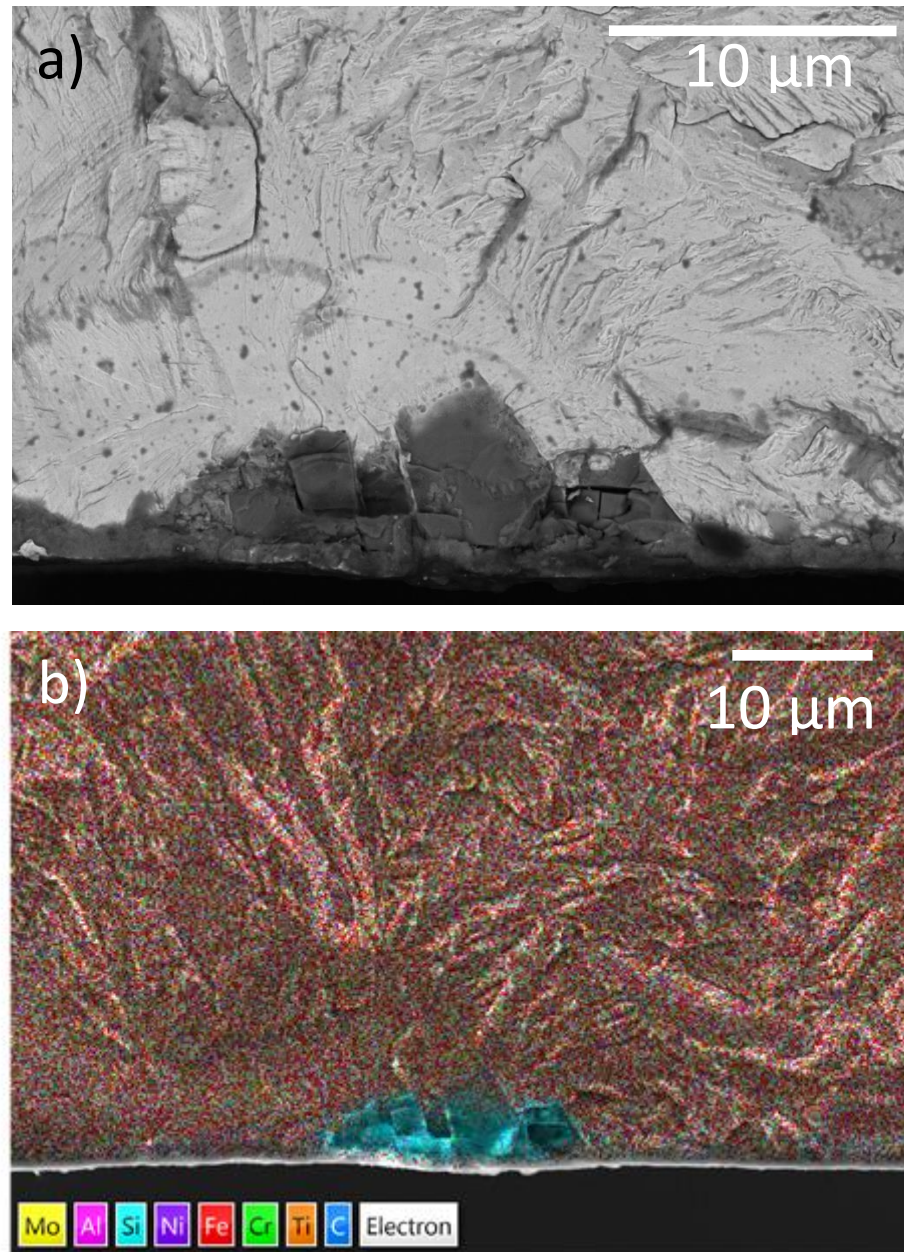


Figure 32: Initiation site of a Condition 2 specimen polarized to $-200\text{mV}_{\text{SCE}}$ for 24 hours prior to fatigue. Fatigue was conducted at an $R=0.5$, $f=2$, and a maximum stress of 1153 MPa. A backscatter electron image (a) and a corresponding EDS image (b) show the silicon inclusion initiating the crack. This initiating particle was located underneath stop off lacquer, unaffected by bulk environment.

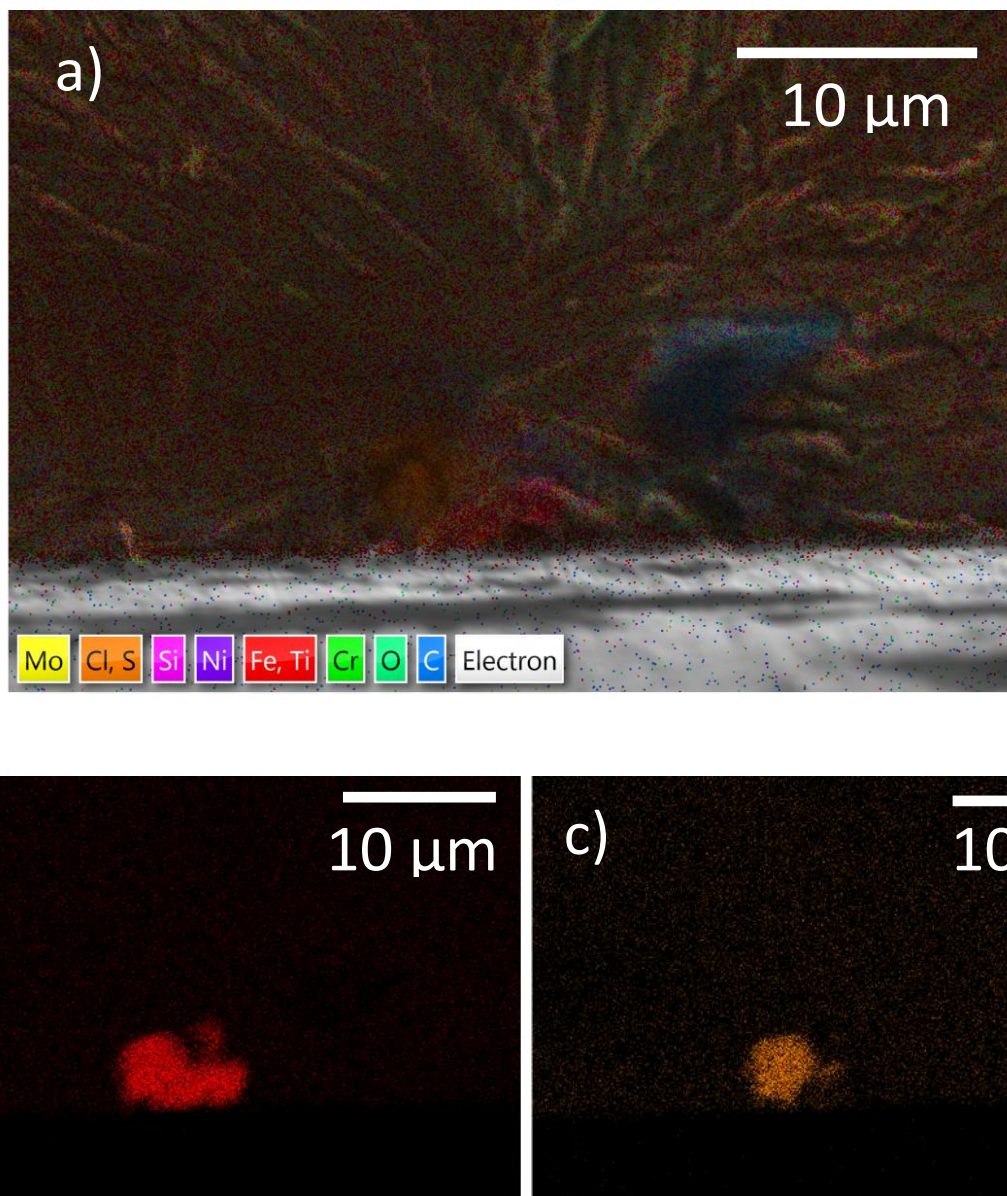


Figure 33: EDS from a Condition 3 specimen polarized to $150\text{mV}_{\text{SCE}}$ for 1 hour prior to fatigue. Fatigue was conducted at an $R=0.5$, $f=2$, and a maximum stress of 1153 MPa. This EDS shows the TiS inclusion responsible for one crack initiation underneath the lacquer. The overview, inclusive of all elements, is shown in (a). For clarity, individual profiles of titanium (b) and sulfur (c) are included.

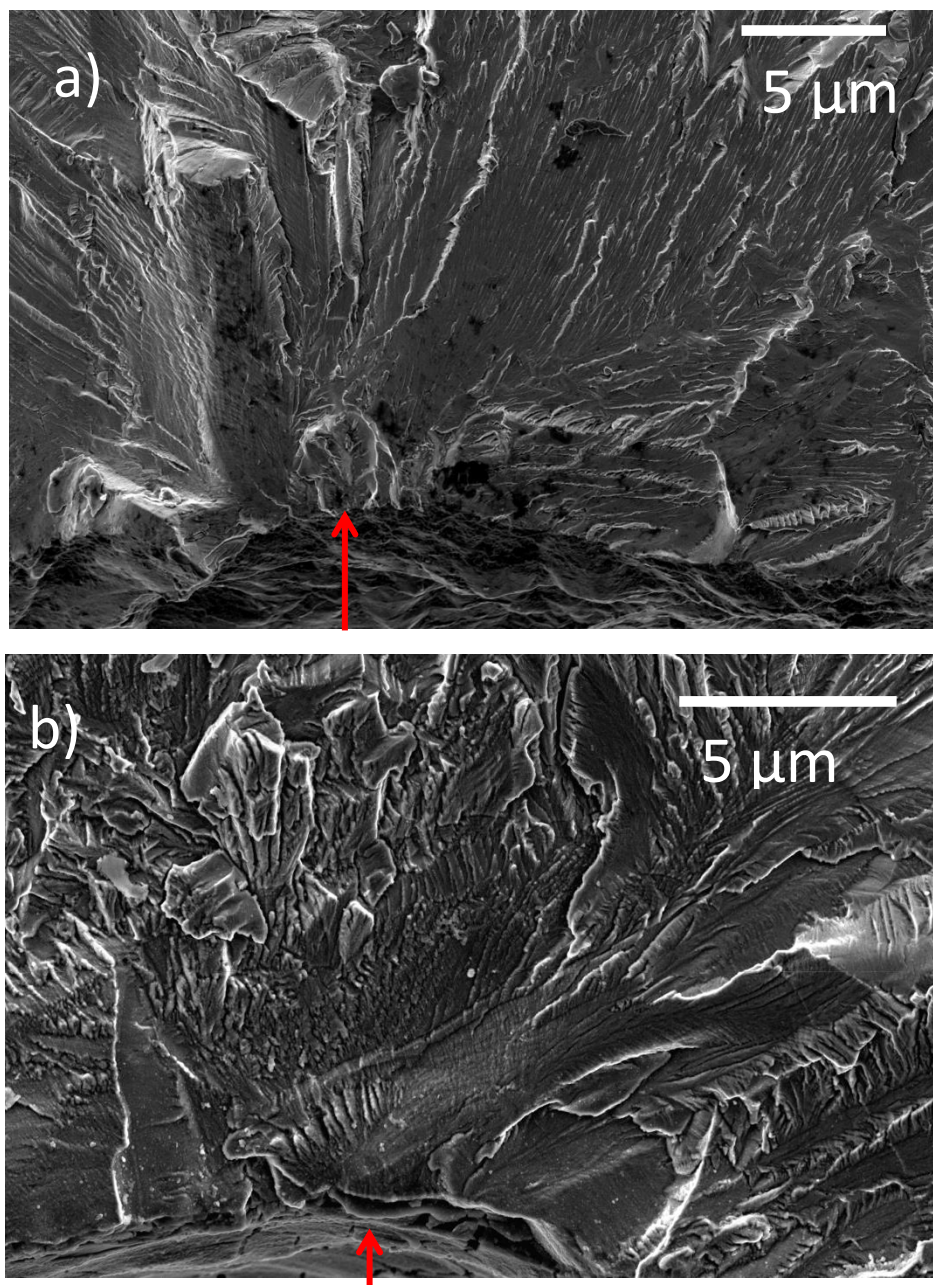


Figure 34: Close-up images of initiation point as indicated by the red arrow in (a) conducted in 0.06M [Cl⁻] and (b) conducted in 3.0M [Cl⁻].

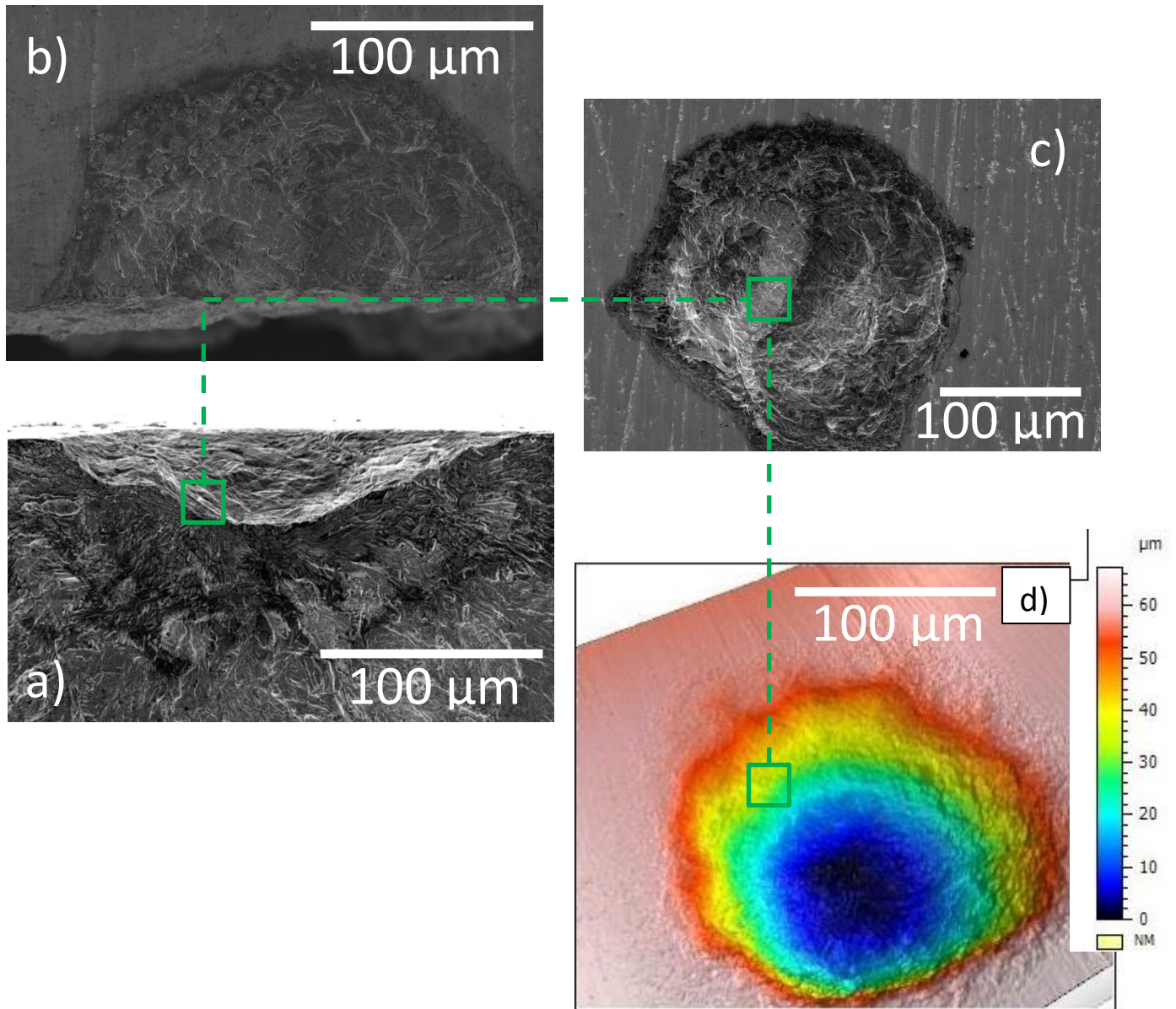


Figure 35: SEM and white light profilometry from a Condition 4 specimen fatigued at $R=0.5$, $f=2$, and a maximum stress of 1153 MPa. Initiation location (green box) can be easily determined on the fracture surface (a) via the marker band technique. Once the location has been identified on the fracture surface, it can also be found at the edge of a fractured pit on the corroded surface (b). The initiation location can be traced on an image of the pit pre-fatigue (c) and can be correlated to the height profile shown in (d). This provides exact metrics regarding crack initiation location. The relative height scale in (d) ranges from $0\mu\text{m}$ (black) to $60\mu\text{m}$ (pink).

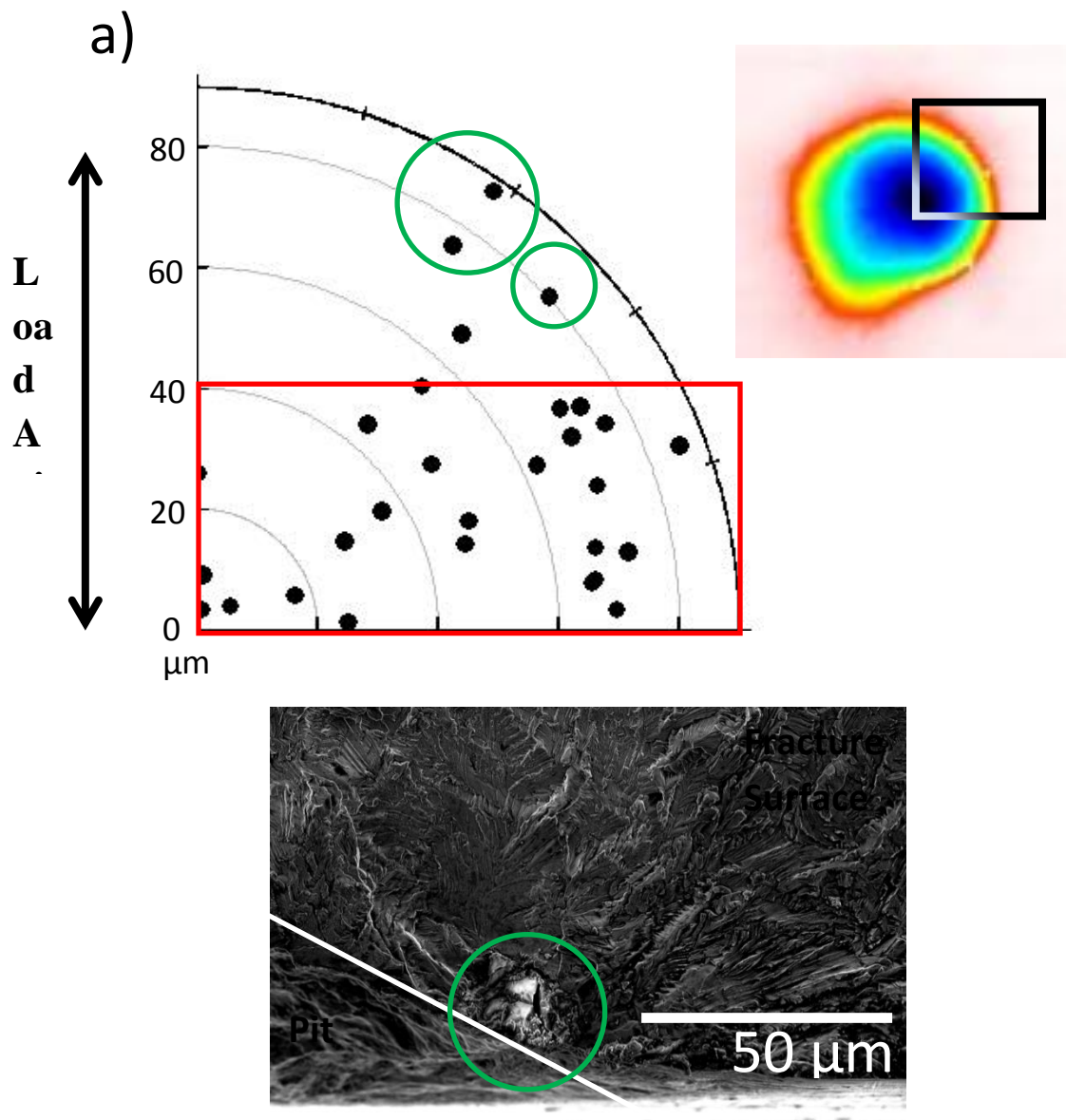


Figure 36: (a) Crack initiation locations for all Condition 4 specimens are plotted on a generic representation of a pit $175\mu\text{m}$ in diameter. Initiation locations are condensed into a single quadrant represented by the box on the colored pit image. The origin represents the exact center of the pit. The red box highlights the pit area within $40\mu\text{m}$ of the centerline. The green circles indicate crack initiation at an inclusion particle in (a). (b) shows a secondary electron image of a pit initiating a crack within a pit. The white line delineates the fracture surface from the pit. The inclusion is circled in green.

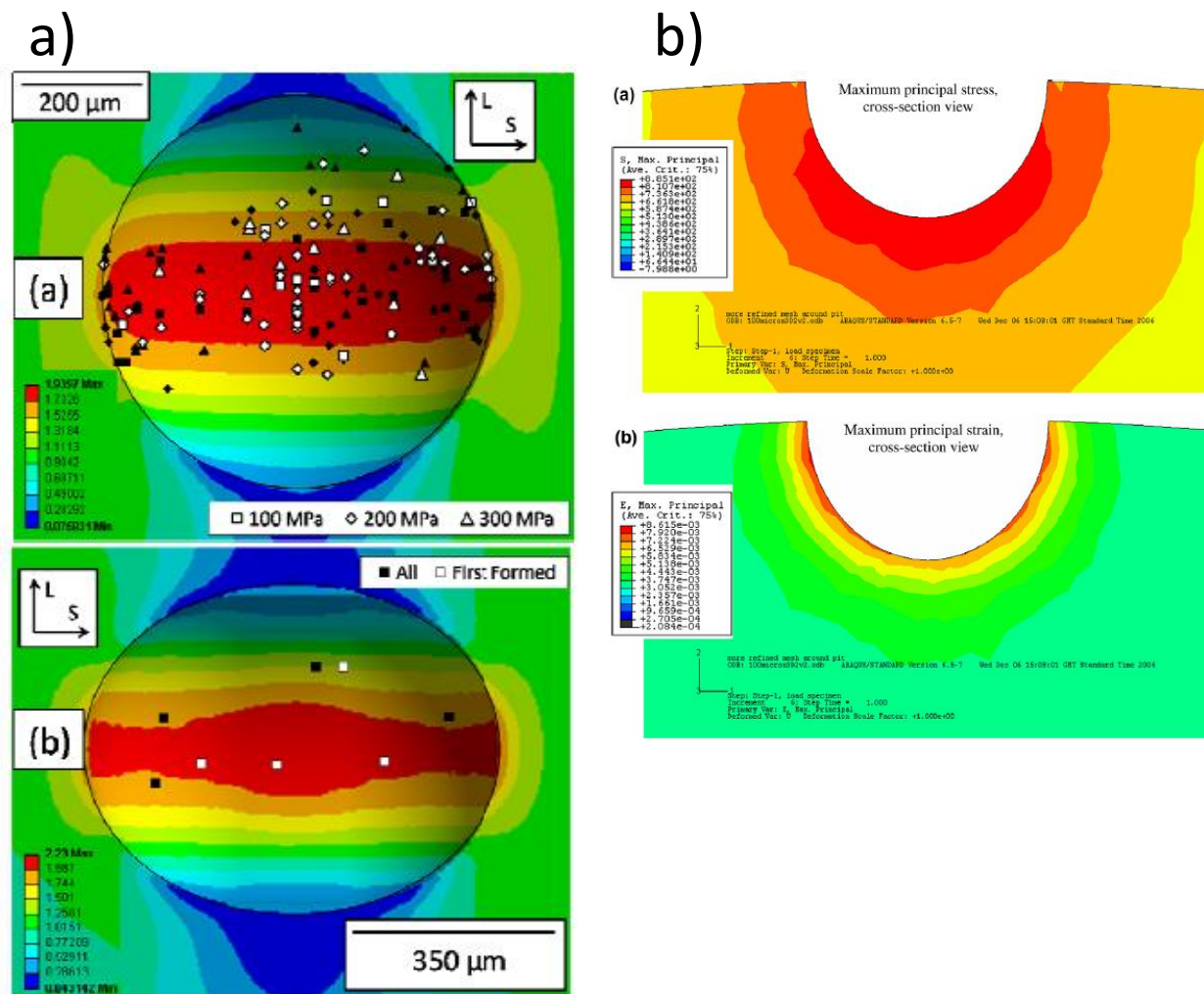


Figure 37: Modeling efforts by Burns [126] (a) and Horner/Turnbull [127] (b) showing stress and strain profiles in hemispherical pits.

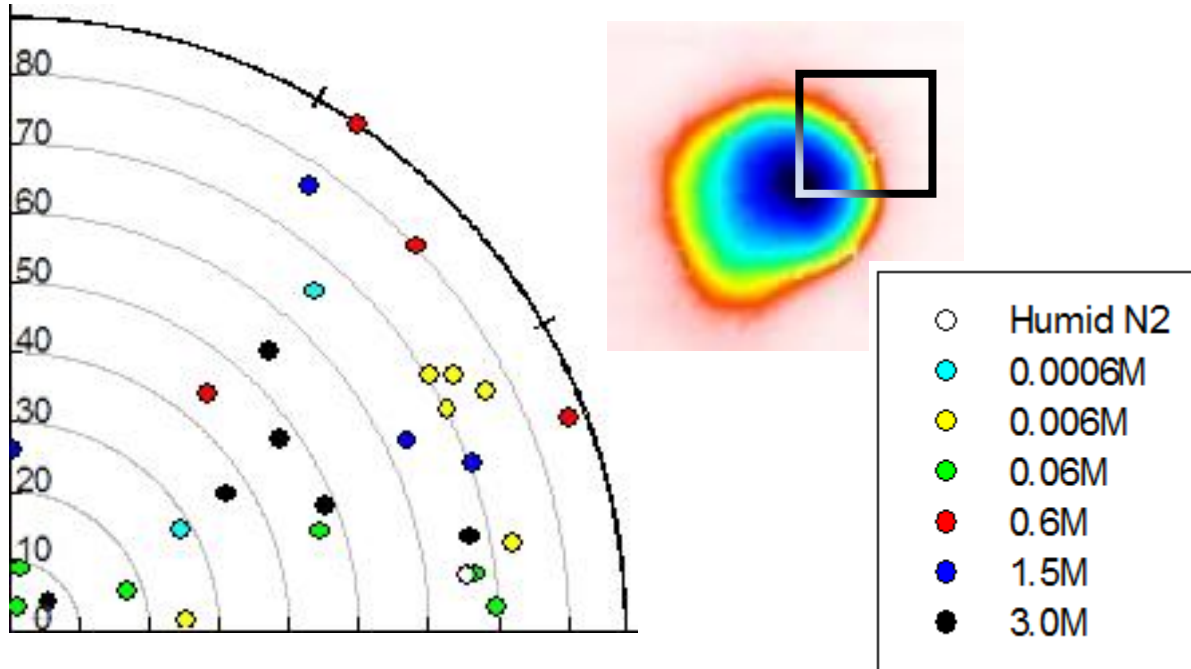


Figure 38: This graph shows pit initiation location as a function of chloride concentration. All data is taken from Condition 4 specimens polarized to $-200\text{mV}_{\text{SCE}}$ for the duration of fatigue. Fatigue was conducted at an $R=0.5$, $f=2$, and a maximum stress of 1153 MPa .

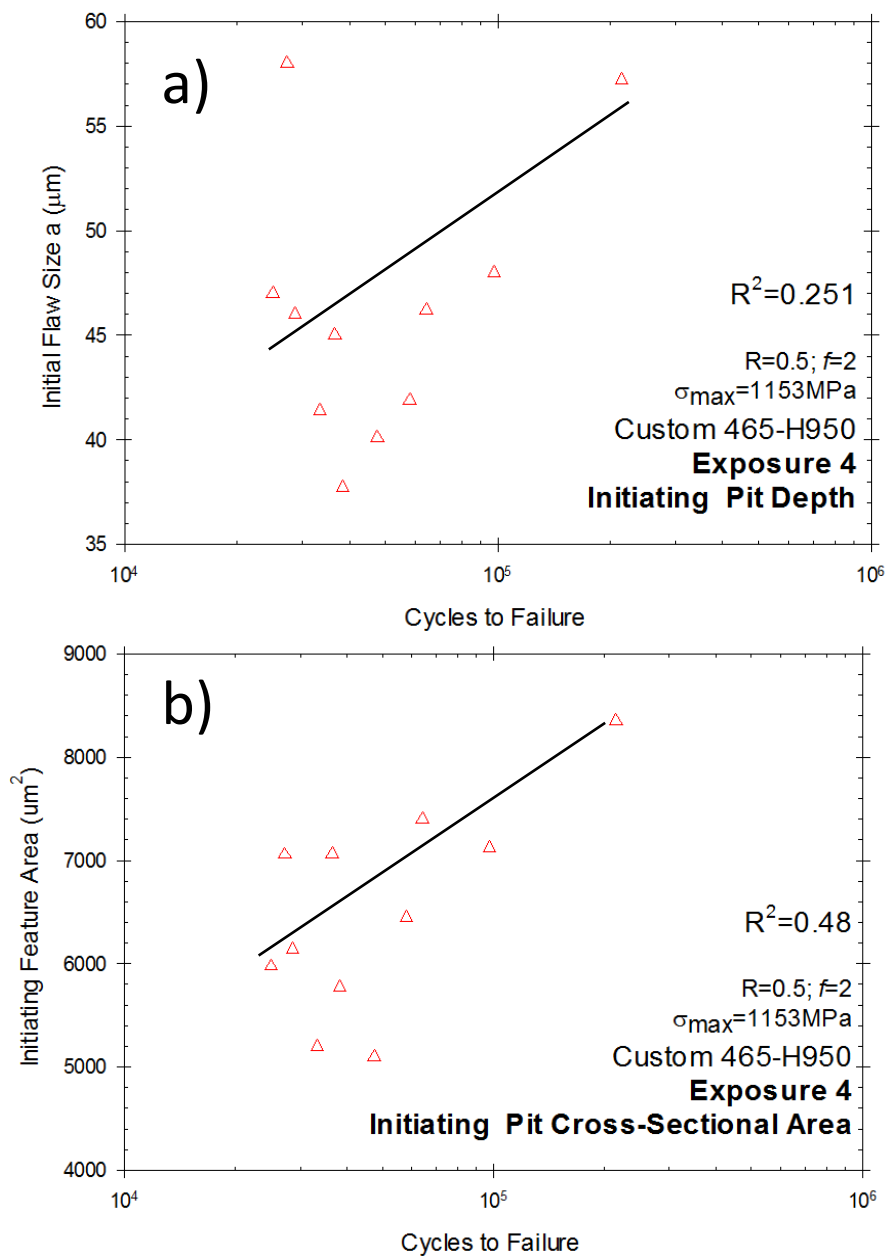


Figure 39: Fatigue life is plotted against pit size in (a) (depth into microstructure) and 2D cross-sectional area (b). All data is taken from Condition 4 specimens polarized to $-200\text{mV}_{\text{SCE}}$ for the duration of fatigue. Fatigue was conducted at an $R=0.5$, $f=2$, and a maximum stress of 1153MPa .

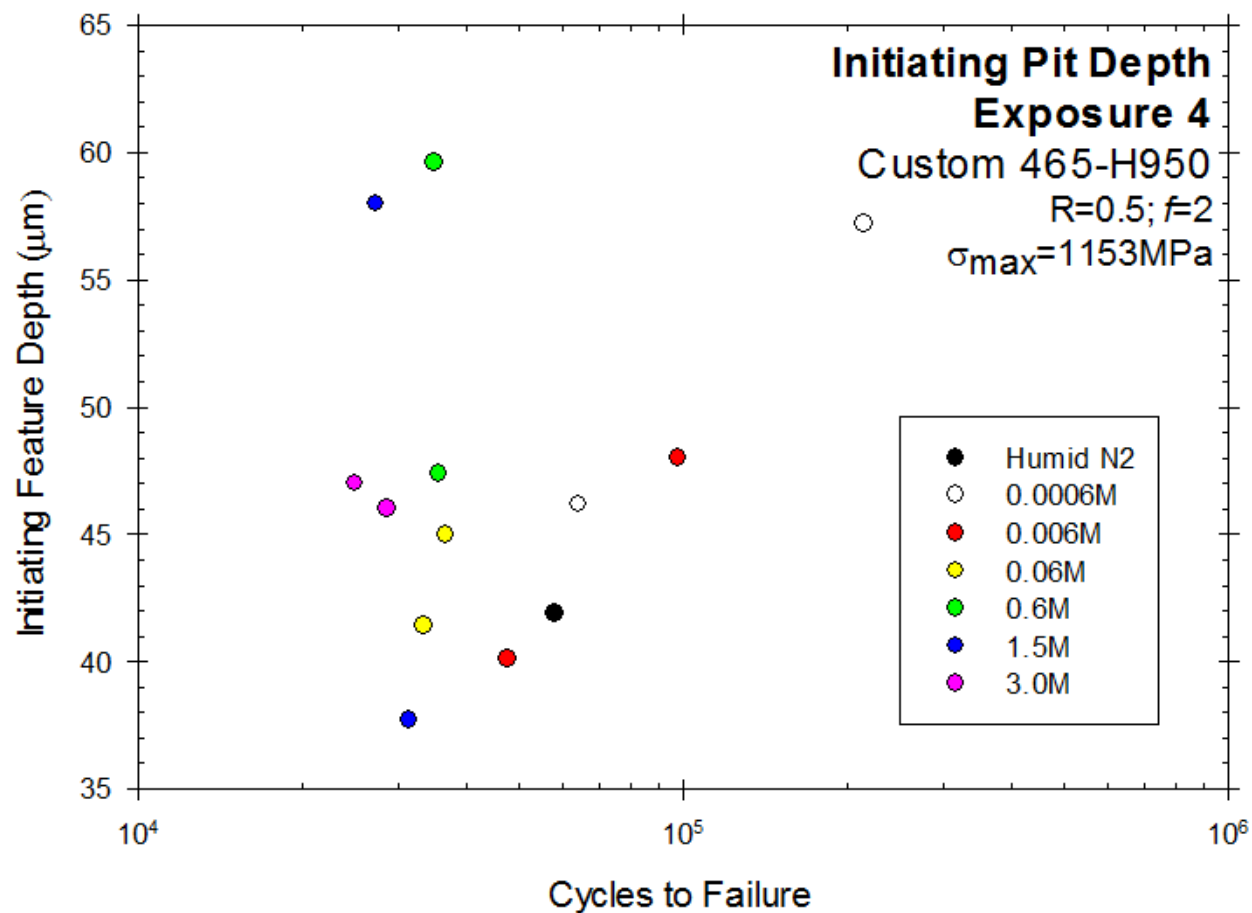


Figure 40: Identical to Figure 39 except this figure includes the [CI] of the environment. All data is taken from Condition 4 specimens polarized to -200mV_{SCE} for the duration of fatigue. Fatigue was conducted at an $R=0.5$, $f=2$, and a maximum stress of 1153 MPa.

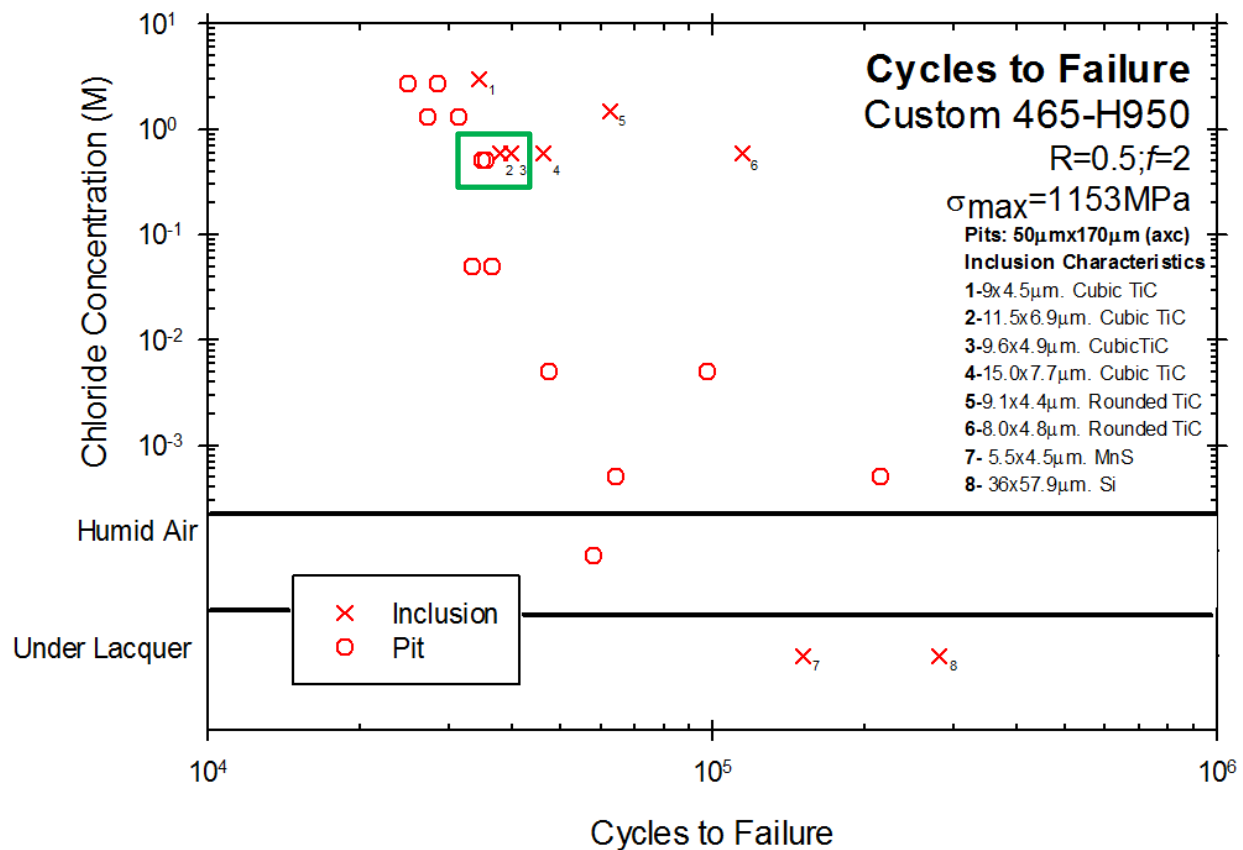


Figure 41: This plot includes all Condition 2 and 3 specimens initiating on a TiC inclusion and all Condition 4 specimens initiating from a pit. Fatigue was conducted at -200mV_{SCE} , an $R=0.5$, $f=2$, and a maximum stress of 1153 MPa. Initiating inclusion measurements are included for relevant Condition 2 and 3 specimens.

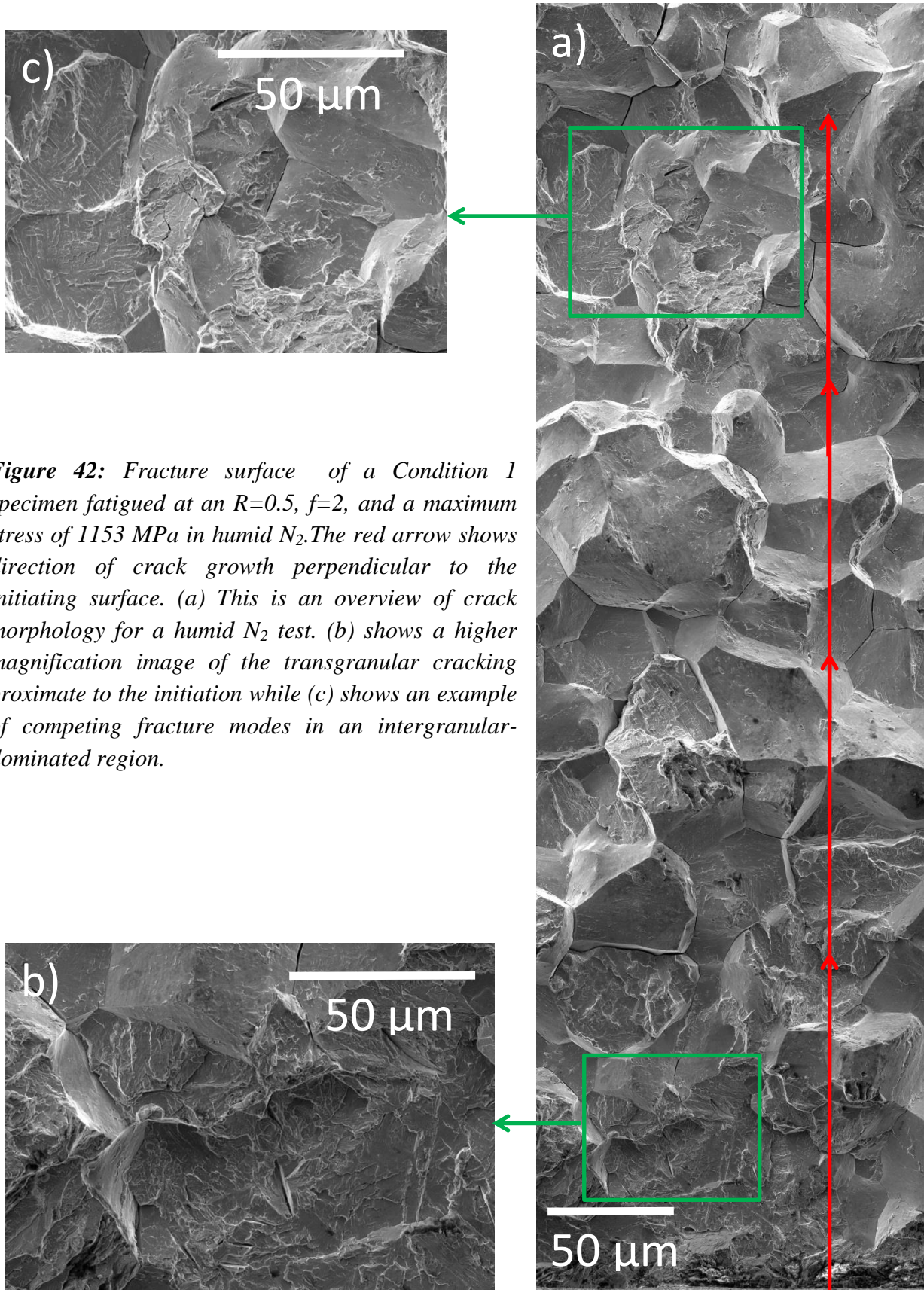


Figure 42: Fracture surface of a Condition 1 specimen fatigued at an $R=0.5$, $f=2$, and a maximum stress of 1153 MPa in humid N_2 . The red arrow shows direction of crack growth perpendicular to the initiating surface. (a) This is an overview of crack morphology for a humid N_2 test. (b) shows a higher magnification image of the transgranular cracking proximate to the initiation while (c) shows an example of competing fracture modes in an intergranular-dominated region.

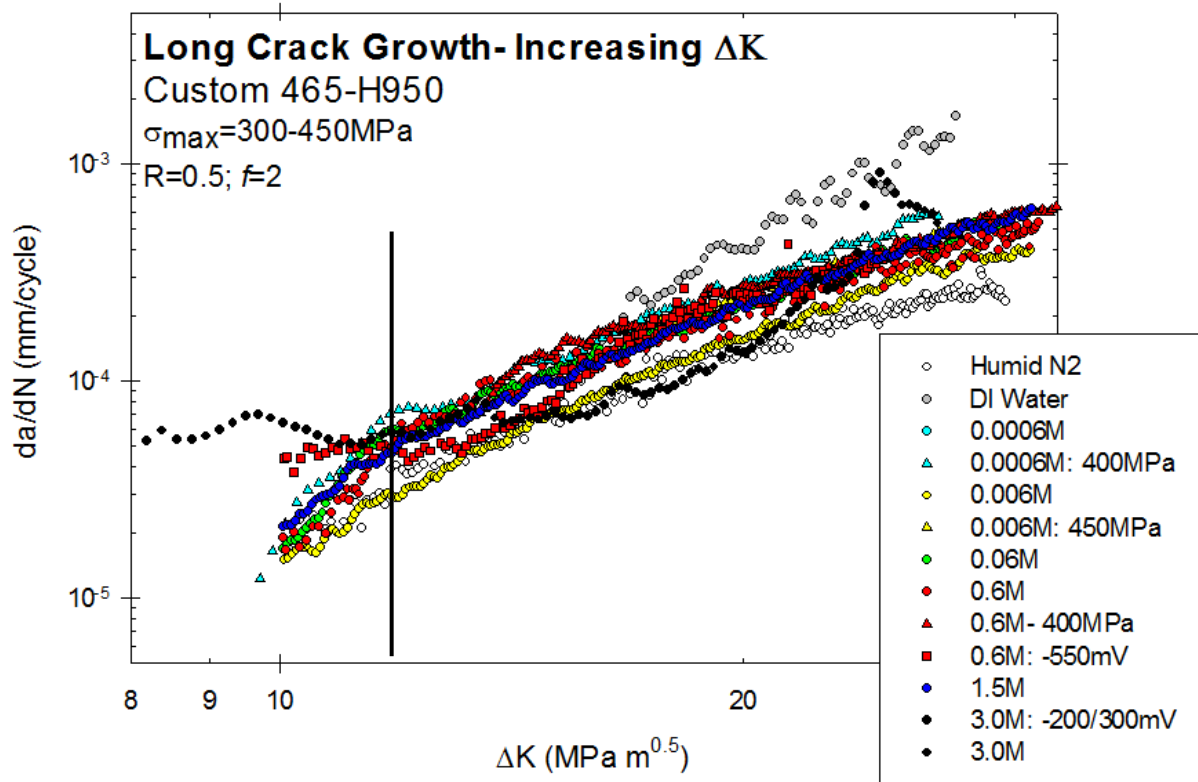


Figure 43: da/dN data collected from SEN specimens the Phase I increasing- K regime. All fatigue was conducted at an $R=0.5$, $f=2$, and a nominal stress between 300-450MPa. K increased up to a K_{max} of $55\text{MPa}\sqrt{\text{m}}$.

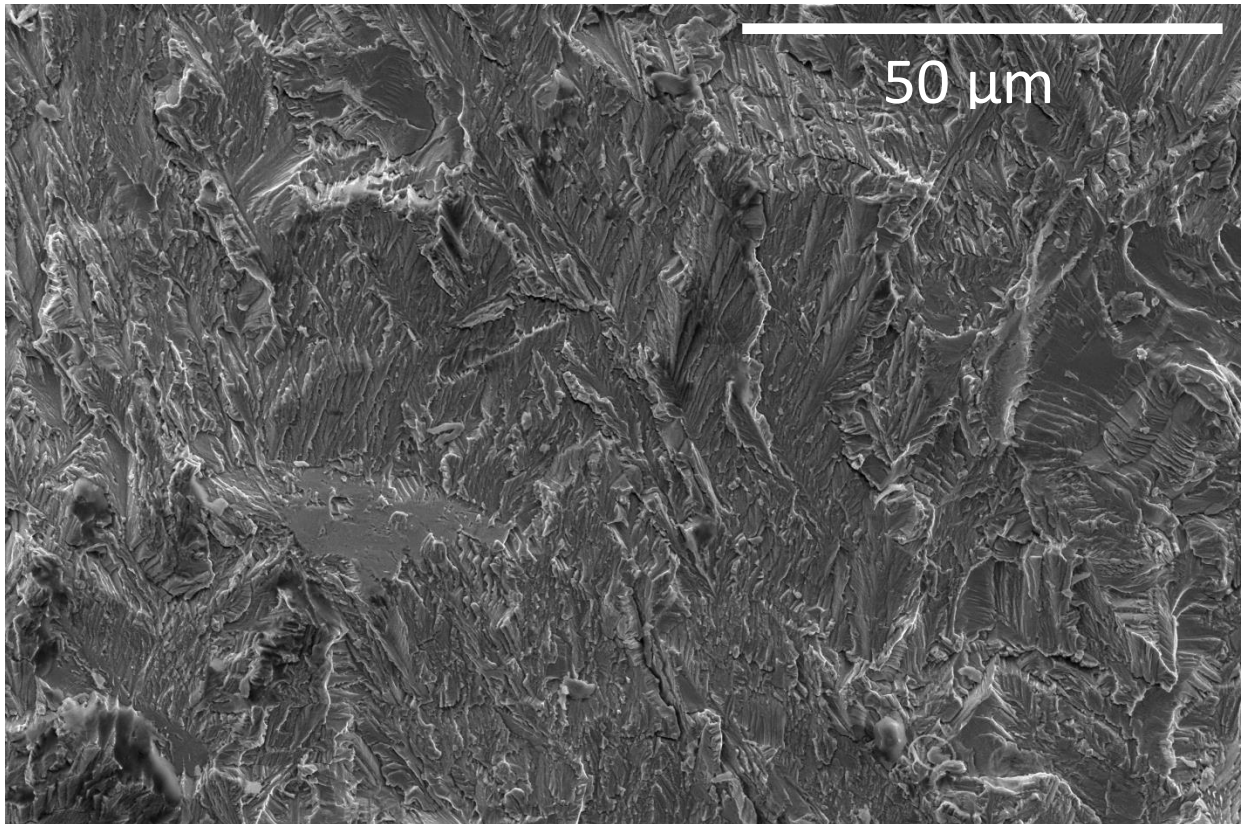


Figure 44: Transgranular cleavage exemplifying typical fracture morphology in the Phase I increasing- K regime. This is taken from a specimen fatigued in a $0.0006M [Cl^-]$ solution at an $R=0.5$, $f=2$, and a nominal stress of $300MPa$.

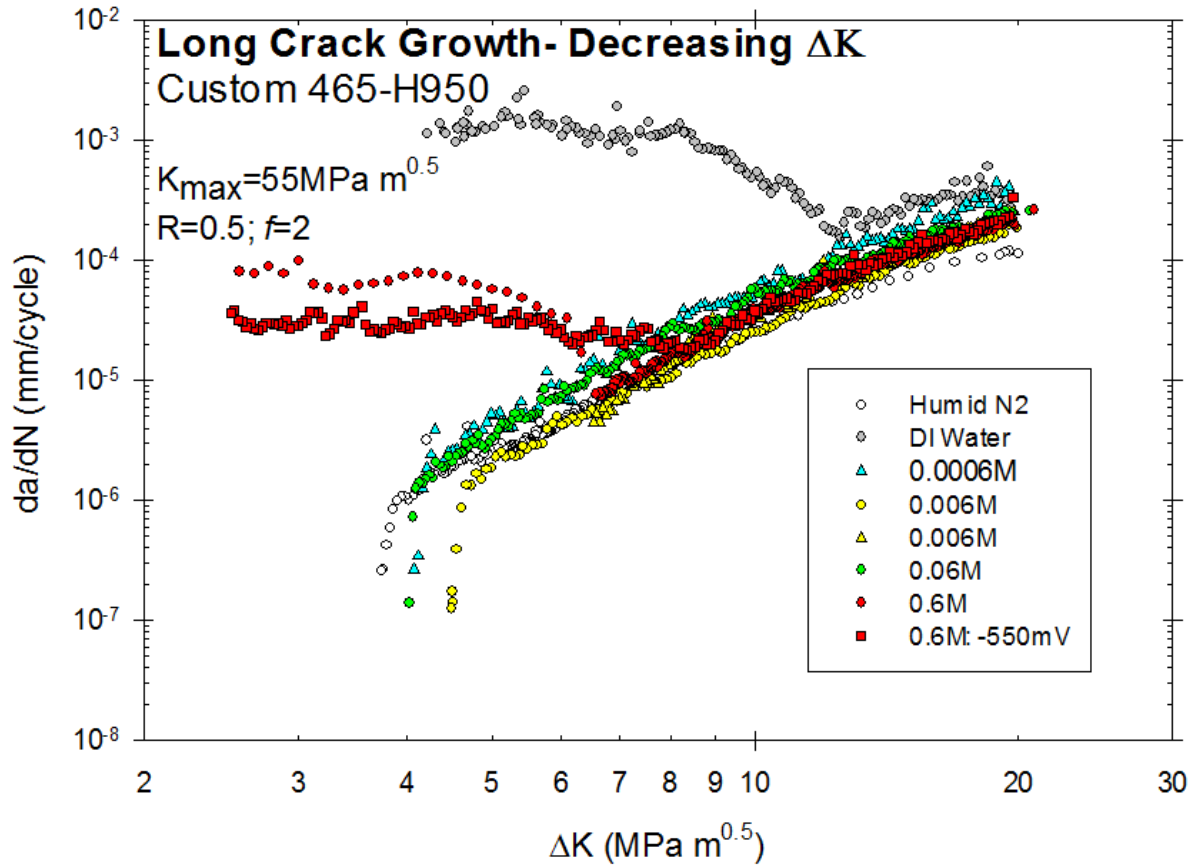


Figure 45: da/dN vs ΔK for the constant K_{max} -decreasing ΔK fatigue testing. All fatigue was conducted at an $R=0.5$, $f=2$ and a K_{max} of $55\text{MPa}\sqrt{\text{m}}$.

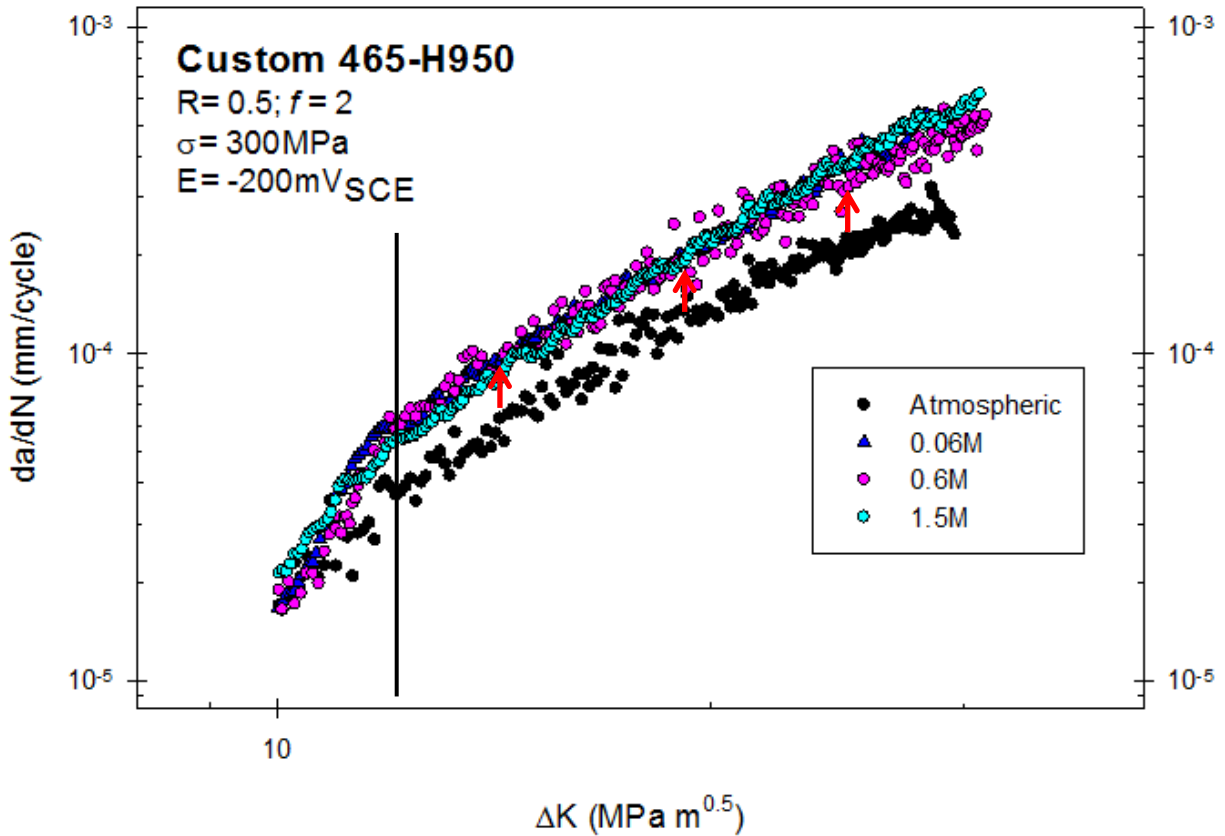


Figure 46: Increasing- K data more clearly demonstrating deviation from atmospheric crack behavior at low ΔK . The red arrows show the contribution of corrosion fatigue phenomena as an increase in da/dN from humid N_2 testing. The black line denotes the $\Delta K = 11.5 \text{ MPa m}^{0.5}$. All fatigue was conducted at an $R = 0.5$, $f = 2$, and a nominal stress between 300-450 MPa. K increased up to a K_{max} of $55 \text{ MPa m}^{0.5}$.

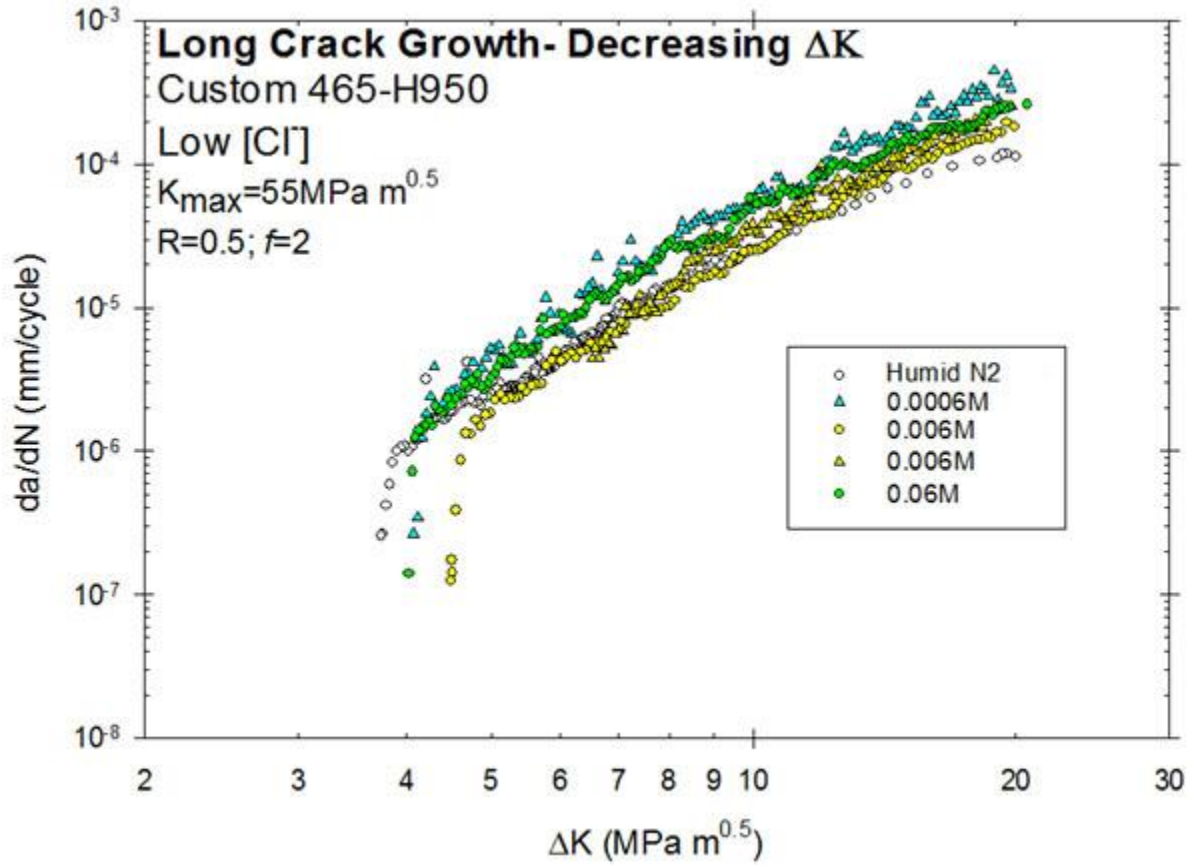


Figure 47: Low [Cl⁻] decreasing-K fatigue test. All fatigue was conducted at an $R=0.5$, $f=2$, and a nominal stress between 300-450MPa. K increased up to a K_{max} of 55MPa \sqrt{m} .

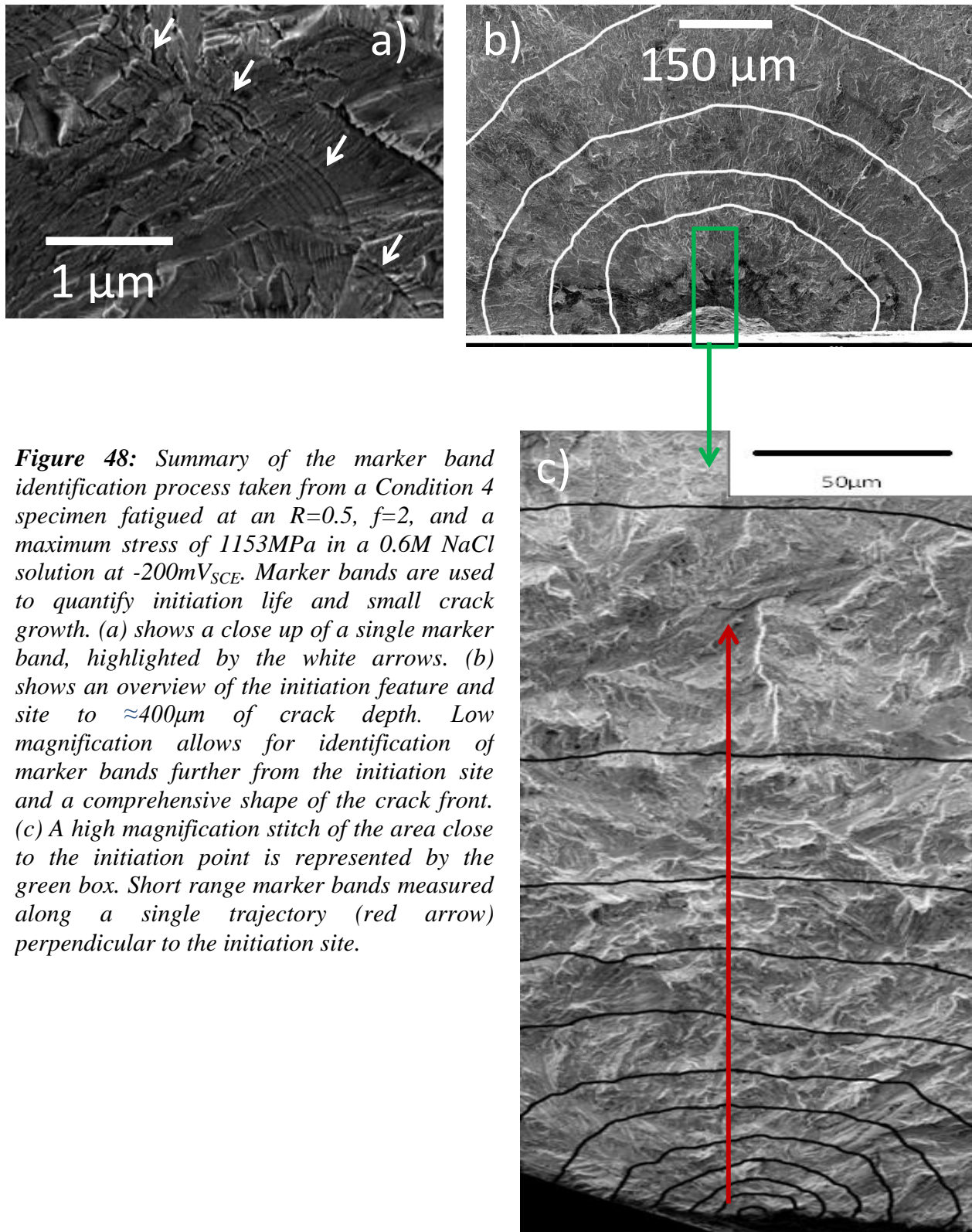


Figure 48: Summary of the marker band identification process taken from a Condition 4 specimen fatigued at an $R=0.5$, $f=2$, and a maximum stress of 1153MPa in a 0.6M NaCl solution at $-200\text{mV}_{\text{SCE}}$. Marker bands are used to quantify initiation life and small crack growth. (a) shows a close up of a single marker band, highlighted by the white arrows. (b) shows an overview of the initiation feature and site to $\approx 400\mu\text{m}$ of crack depth. Low magnification allows for identification of marker bands further from the initiation site and a comprehensive shape of the crack front. (c) A high magnification stitch of the area close to the initiation point is represented by the green box. Short range marker bands measured along a single trajectory (red arrow) perpendicular to the initiation site.

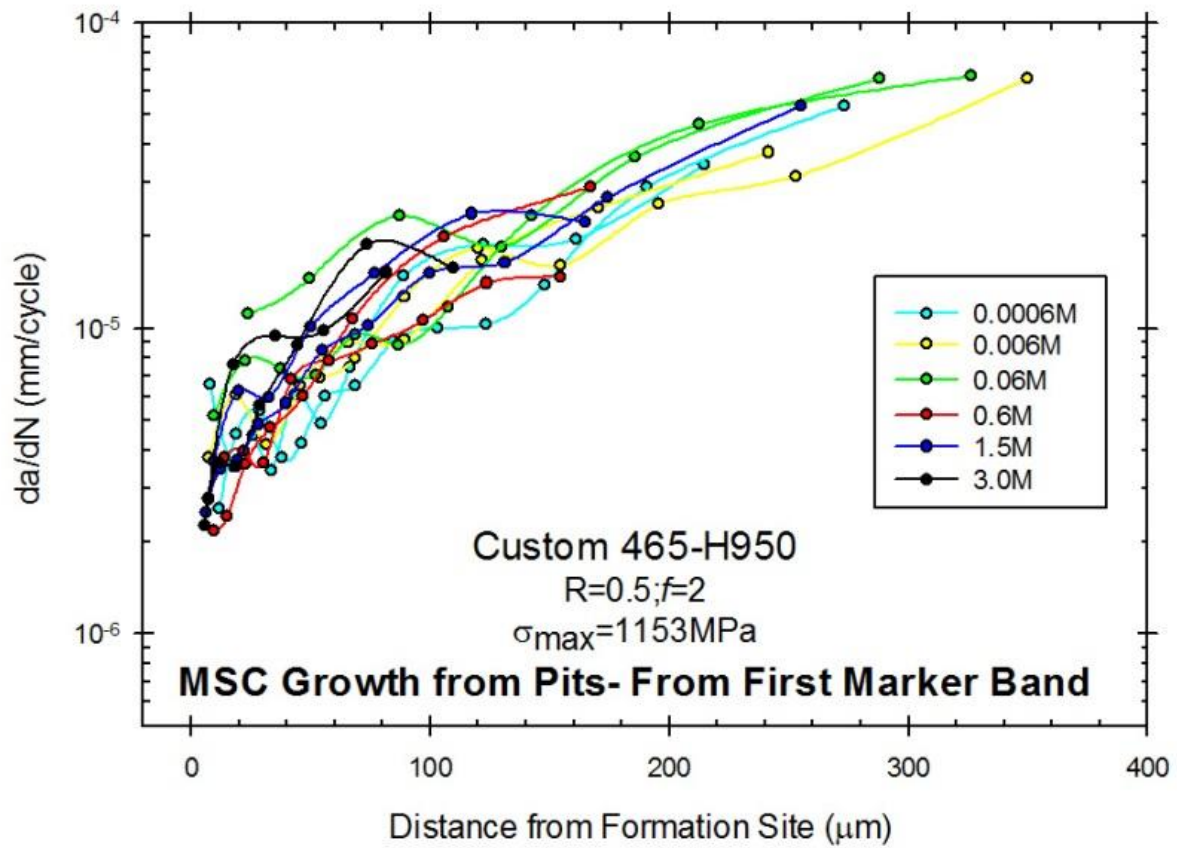


Figure 49: Plot showing the minimal effect of $[Cl^-]$ on small crack growth kinetics nucleating at Condition 4 designer pits. Condition 4 specimen fatigued at an $R=0.5$, $f=2$, and a maximum stress of 1153MPa at -200mV_{SCE} .

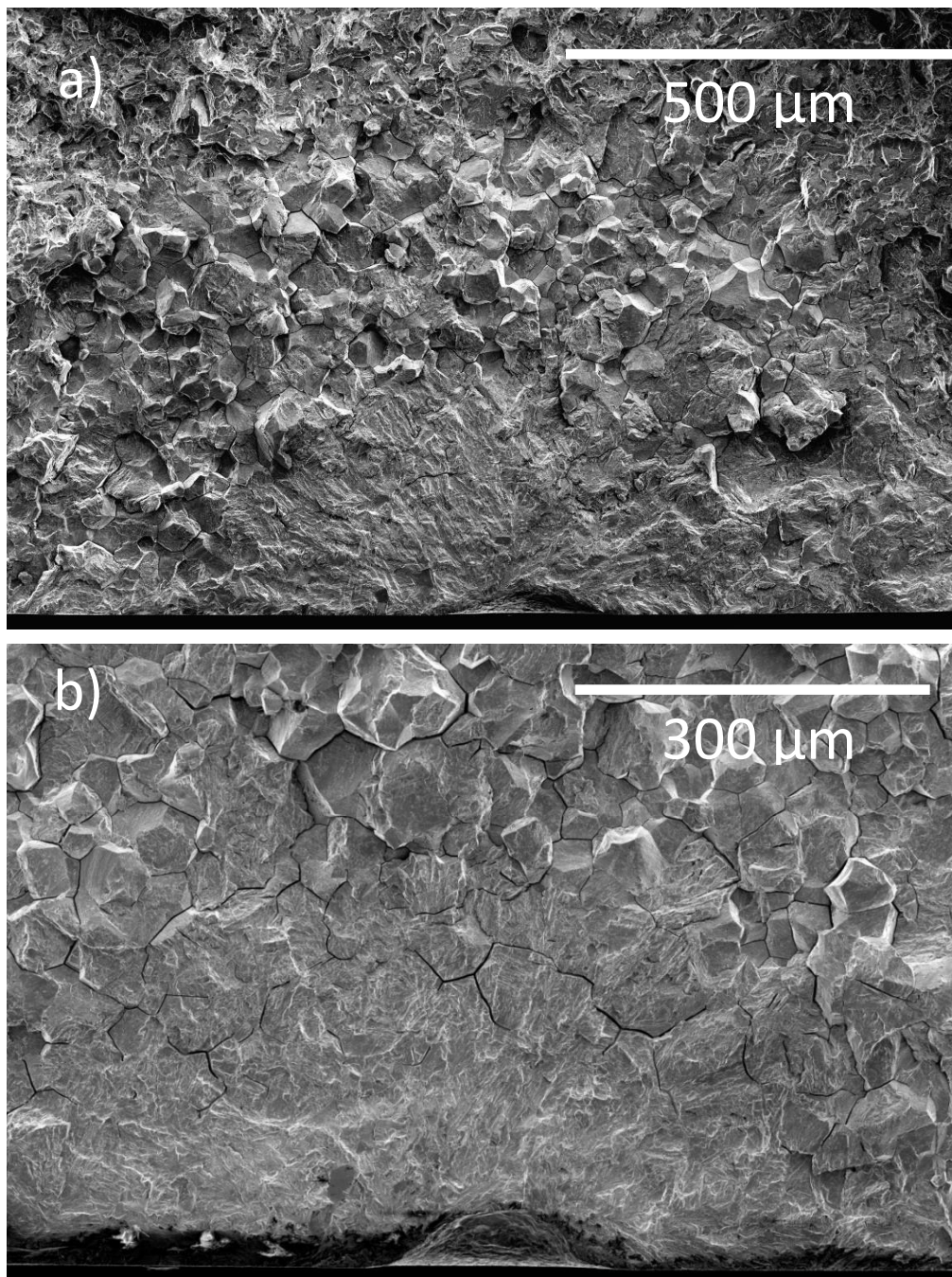


Figure 50: Images of the initiation area of Condition 4 specimens fatigued at an $R=0.5$, $f=2$, and a maximum stress of 1153MPa at $-200\text{mV}_{\text{SCE}}$. Low magnification (a) and higher magnification (b) fractography of the initiation site of two Condition 4 pits in 3.0M NaCl solution.

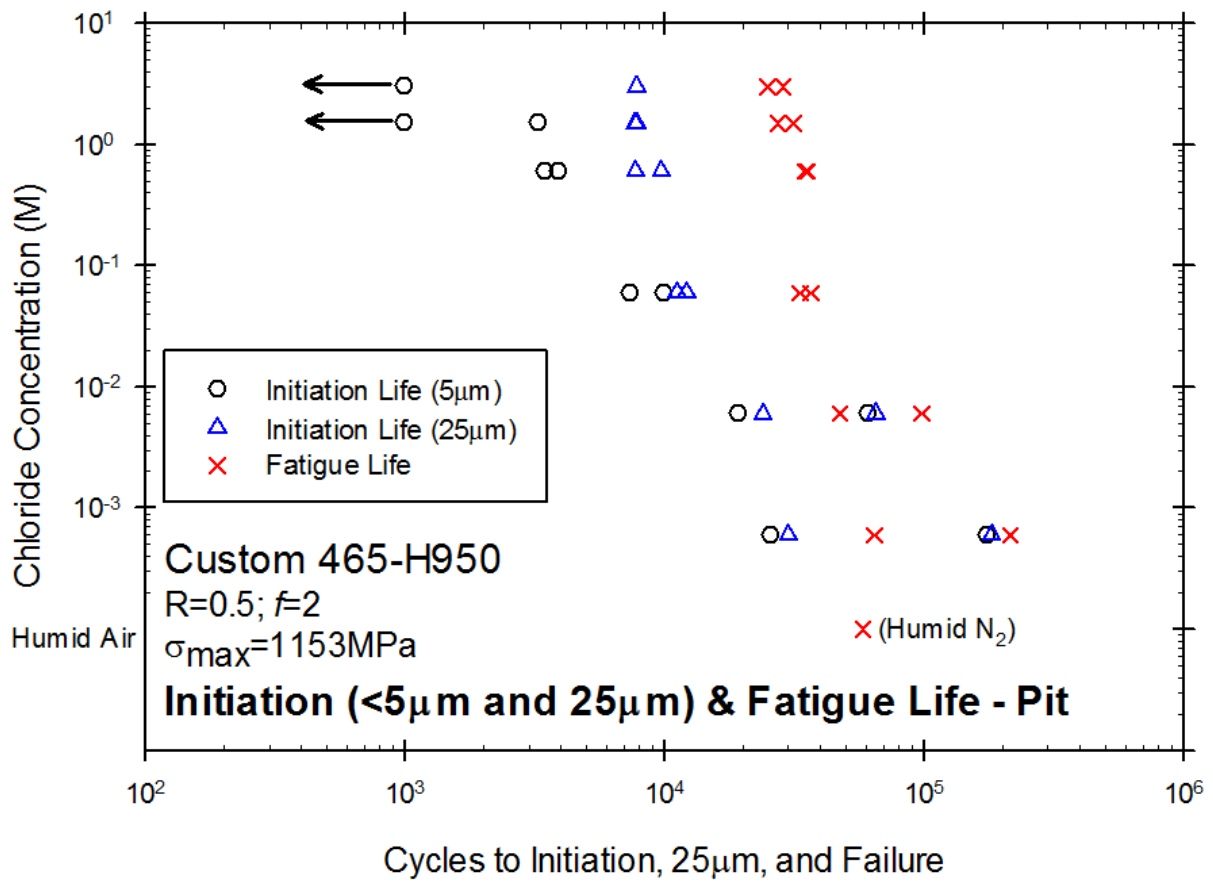


Figure 51: N_i , $N_{i,25}$, and N_f for Condition 4 specimens fatigued at an $R=0.5$, $f=2$, and a maximum stress of 1153MPa in various NaCl environments and humid N_2 .

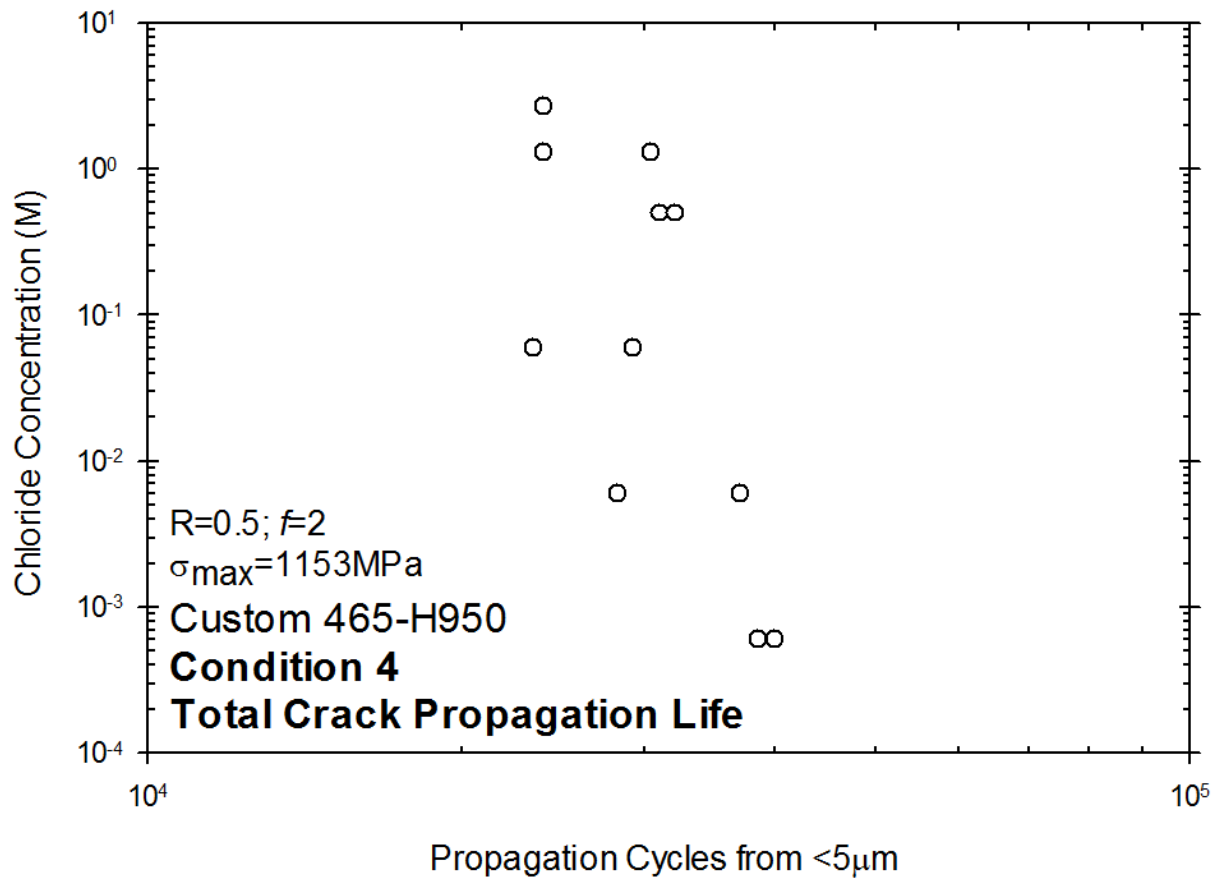


Figure 52: Total crack propagation life for Condition 4 specimen fatigued at an $R=0.5$, $f=2$, and a maximum stress of 1153MPa and a polarization of $-200\text{mV}_{\text{SCE}}$.

Appendix A

Long crack growth rates observed in Phase I were generally consistent across a wide range of ΔK and $[Cl^-]$. However, anomalous fatigue crack growth was observed in both the increasing and decreasing-K regimes. This behavior is generally independent of ΔK and is characterized by above average crack growth rates in certain environments. In the increasing-K regime (Figure 43), a plateau region of unusually high growth rates is observed starting at very low ΔK when the specimen is in 3.0M NaCl or is polarized to $-550mV_{SCE}$. These growth rates maintain independence from ΔK up to $\Delta K=16MPa\sqrt{m}$, at which point rates increase in the expected fashion with ΔK . In the decreasing-K constant K_{max} regime (Figure 45), sudden deviations from expected linear behavior resulting in a plateau occurring when the specimen is in 0.6M NaCl, DI water, or is polarized to $-550mV_{SCE}$. Deviations occur at a variety of $\Delta K < 11MPa\sqrt{m}$, and crack growth rate plateaus remain even as ΔK approaches $2MPa\sqrt{m}$.

Stress corrosion cracking is hypothesized to be the cause of this unusual behavior. SCC is a cracking phenomenon that may occur when a susceptible metal is exposed to a corrosive environment and loaded in tension. Literature reports SCC in a variety of steels in many aqueous environments, particularly those containing chlorides [152-156]. It is a particularly insidious form of corrosion capable of significantly reducing mechanical strength and toughness. As such, empirical research of SCC phenomena in relatively new UHSSS is paramount to predictive modeling-based engineering component design. The goals of this appendix are to: (1) develop and validate an SCC-based explanation of the observed anomalous growth rate behavior (Figure 43 and Figure 45) that is observed during increasing and decreasing-K experiments, (2) discuss a potential mechanism to explain why this SCC behavior is occurring below the critical stress intensity threshold (K_{ISCC}) developed for quasi-static loading, and (3) discuss the implication of this behavior in the context of component structural integrity.

A.1 Validation of SCC

Accelerated long crack growth is observed in both increasing and decreasing K regimes, serving as a starting point for this SCC investigation. Mild increases in da/dN over atmospheric rates, as seen in low $[Cl^-]$ fatigue testing, are certainly a product of the corrosive environment but are unlikely the result of SCC. The plateau regions associated with high $[Cl^-]$ environments and $-550mV_{SCE}$ cathodic polarization are of particular interest as these rates approximately

independent of ΔK , suggesting that a non-fatigue process is determining growth kinetics. Such a plateau behavior shows the classic growth rate trends that are attributed to a strong contribution from SCC [157]. This hypothesis will be tested by examining the fracture surface morphology as well as targeted fatigue testing where the frequency is systematically varied.

SEM fractography of crack sizes corresponding to the unusual crack growth rate behavior is shown in Figure 53 for two entire Phase I specimens. The top image is from a test in 0.0006M NaCl solution polarized to $-200\text{mV}_{\text{SCE}}$ in which transgranular fracture modes were active throughout the test. The bottom image is from a test in 0.6M NaCl solution polarized to $-200\text{mV}_{\text{SCE}}$ and shows remarkably different fracture morphology, further detailed in Figure 54. In this figure, region 1 refers to the increasing-K regime where $R=0.5$ spanning a K of $20\text{-}55\text{MPa}\sqrt{\text{m}}$ and shows the associated transgranular fracture characteristic of this regime. Crack growth rates in this regime align well with rates gathered from humid N_2 , save a slight increase due to corrosion fatigue. Regions 2 and 3 are taken from the decreasing-K regime with a constant K_{max} and decreasing ΔK from $20\text{MPa}\sqrt{\text{m}}$ to threshold or failure which corresponds to a ΔK on the order of a few $\text{MPa}\sqrt{\text{m}}$. As expected, region 2 shows crack growth rates aligning with the humid N_2 data. Like the increasing-K regime, these crack growth rates correspond to a transgranular fracture surface morphology, though slight intergranular morphology is observed. Region 3 depicts the crack growth rate plateaus mentioned previously. These K -independent anomalously high crack growth rates correspond directly to pure intergranular cleavage observed on the fracture surface.

Coupling crack growth rate data and SEM fractography confirms the consistent coincidence of crack growth acceleration and intergranular fracture modes. While intergranular fracture could be a result of corrosion fatigue, it is more commonly associated with SCC in stainless steels. Intergranular failure is noted as a fracture mechanism indicative of SCC in martensitic steels [29], and has even been shown to occur in chloride-free solutions [146, 147]. As such, the fractography fully supports the hypothesis that the plateau regions are caused by the dominance of a SCC-based mechanism.

Additionally, the SCC cracking mode is largely governed by the K_{max} value. Therefore, in decreasing-K testing where the K_{max} value is constant, the rate of SCC-based cracking (da/dt) should be constant and independent of cycling frequency. If da/dt is constant during the

decreasing-K testing for this SCC-based cracking mode, then varying the frequency should result in a direct change in cycle-based cracking rate (da/dN) as captured by the relationship:

$$\frac{da}{dN} = \frac{1}{f} \times \frac{da}{dt} \quad (5)$$

Variable frequency testing was performed in two decreasing-K tests in 0.6M and 1.5M [Cl⁻] solutions to further investigate factors governing crack growth and to determine if SCC was occurring. Once a plateau was observed, frequency was changed from the standard 2Hz to 0.2Hz and then, after some time, increased to 20Hz. In both cases, this change in frequency was met respectively by an order of magnitude increase then decrease, indicating that in this regime, da/dN is inversely proportional to the frequency. This is shown graphically in Figure 55. A simple calculation shows that the crack growth rates in this plateau regime are actually constant with respect to time (i.e. da/dt is constant). The change in crack growth rate dependence indicates a change in the crack growth mechanism to SCC. Together, the fractography and variable frequency testing strongly supports the occurrence of SCC; however, it is necessary to establish why this SCC-based mechanism is active below the K_{ISCC} measured for quasi-static loading.

A.2 Sub-threshold Fatigue Cracking

The threshold for stress corrosion cracking for C465-H950 at $-550mV_{SCC}$ was reported to be greater than $72MPa\sqrt{m}$ as quantified by using a slow-rising displacement fracture mechanics based test [115]. At a potential of $-200mV_{SCE}$, the monotonic K_{ISCC} would be expected to be higher, as suggested by Figure 56 that reports the K_{TH} for various different potential values. Additionally, these data are presented for the H900 condition which should be more susceptible to environmentally assisted cracking than C465 in the H950 condition. Thus, the $>72MPa\sqrt{m}$ value reported in Figure 56 is expected to be a conservative estimate of the behavior for the environmental conditions of this research. As such, it is clearly observed in Figure 43, Figure 45 and from the discussion in Appendix A.1 that significant SCC-based growth is observed at K_{max} values ($55MPa\sqrt{m}$ and below) that are well below a conservative estimate of K_{ISCC} .

Crack growth rates in this research should also be compared to those generated by Pioszak. Figure 57 shows da/dt_{I-II} for C465-H900 associated with SCC crack growth validated by a da/dt_{II} independent of ΔK . The testing environment of the Pioszak study is 0.6M NaCl with an

applied potential of $-575\text{mV}_{\text{SCE}}$, loaded with a dK/dt of about $1\text{MPa}\sqrt{\text{m/hr}}$. Da/dt_{II} in C465-H900 in Pioszak's study are on the order of $1\mu\text{m/s}$, whereas da/dt_{II} in this research varies from $0.037\text{-}0.15\mu\text{m/s}$ (excluding DI test). This is not unexpected as C465 in the H950 should be less susceptible to SCC than in the H900 condition (less aged) which would be reflected in the lower growth rate. Polarization may also explain the difference in growth rate. The effect of applied potential on da/dt_{II} for C465-H900 is plotted in Figure 58. Crack growth rates are shown to reach a plateau maximum of about $1\mu\text{m/s}$ at a potential of $-575\text{mV}_{\text{SCE}}$, which is in agreement with the crack growth rates reported in Figure 57. The figure also shows that at $-200\text{mV}_{\text{SCE}}$, the potential applied in this research, that growth rates should be approximately $0.01\text{-}0.02\mu\text{m/s}$, which is markedly less than at $-575\text{mV}_{\text{SCE}}$ and strongly agrees with plateau da/dt observed in this research. Similar to growth rates, the threshold stress intensity also changes with applied potential. K_{TH} achieves its maximum value at a potential between $-550\text{mV}_{\text{SCE}}$ and $-250\text{mV}_{\text{SCE}}$. Outside of this range, K_{TH} declines dramatically to approximately $10\text{MPa}\sqrt{\text{m}}$ as seen in Figure 56. The fatigue potential of $-200\text{mV}_{\text{SCE}}$ is slightly anodic to this range of maximum K_{TH} which may partially explain why SCC occurs below expected thresholds. While the potential dependence is well understood in the context of H-embrittlement a full discussion is outside the scope of this work; the importance of the comparison lies in confirming that that current da/dt values observed in Figure 40 and 42 are reasonably aligned with da/dt_{II} observed in an independent study of SCC in C465.

A.2.1 Ripple Load Effects

The growth rate plateaus observed in Figure 43 and Figure 45 breach two traditional crack growth thresholds: (1) the fatigue ΔK_{TH} which is the threshold for cyclically-induced plasticity interacting with hydrogen, and (2) the SCC threshold K_{ISCC} for monotonic/quasi-static time-dependent cracking. One hypothesis to explain these deviations from classic environmental fatigue and SCC-based thresholds is that the chemical destabilization of the passive film possibly responsible for the SCC behavior is assisted by the mechanical breakdown of the passive film due to local crack tip strains associated with cyclic loading. Researchers have previously reported that small amplitude load perturbations (e.g. $R>0.9$), known as ripple loads, superimposed on a constant stress can induce fracture at sub- K_{ISCC} stress intensity levels [158-161]. An example of a ripple loading stress protocol is represented in Figure 59. Prior research on ripple loading effects in steels generally agrees that ripple loading effects are only of

relevance at small amplitude cyclic loads where $R > 0.9$, where the stress range is insufficient for cyclic damage accumulation to dominate. Research has shown differing behavior in different steels. Ford reports that stainless steel 304 is highly susceptible to ripple load effects [160] while Pao reports 4340 to be essentially immune [158]. da/dt resulting from ripple load induced SCC is agreed to vary inversely with R [160, 162]. Ripple loading effects have been shown to greatly reduce SCC resistance up to $R = 0.97$ [163], though some steels in certain environments are not susceptible to K_{ISCC} -depression at $R > 0.95$ [158]. These dependencies and trends as they relate to C465 are not known.

This environmentally-induced ripple load effect is distinctly different from the other contributions to the environmental crack growth rate captured in Equation 4. Specifically, this behavior is similar to the film rupture hydrogen embrittlement model proposed by others [98, 164-166] in which cyclic ripple loading mechanically destabilizes the crack tip passive film via rupture events. These rupture events occur when crack tip accumulated tensile strain exceeds that required for film rupture which is intrinsic to the material and the environment. Repassivation may occur and is a function of time and the crack tip strain rate. When this behavior occurs in stress intensity ranges above K_{TH} , the H produced at the crack tip is absorbed and interacts with the cyclically-accumulated plastic damage to cause crack progression (as captured by da/dN_{CF}). When this mechanism is active below the fatigue threshold, the magnitude of the cyclically accumulated plastic damage is insufficient to control behavior. Instead, the crack progresses at a rate likely limited by the diffusion of H into the area of maximum hydrostatic stress ahead of the crack tip [151]. This mechanism is distinct from other crack tip driving forces; as such, a term may be added to the previously discussed Wei superposition model to account for these effects:

$$\frac{da}{dN} = (1) \frac{da}{dN_{Vac}} + (2) \frac{da}{dN_{CF}} + (3) \frac{da}{dN_{SCC}} + (4) \frac{da}{dN_{SCC-cyclic}} \quad (6)$$

where term #4 is the contribution of aggressive environment sub-threshold monotonic and cyclic cracking due to conjoint mechanical and environmental destabilization of the passive film at the crack tip. At ΔK above the threshold value, crack growth should be dictated by mechanical driving forces (corrosion fatigue) because the crack tip advance will outpace hydrogen diffusion into the material and provide insufficient time for electrochemical degradation of metal at the

crack tip. SCC is more likely to be active at lower K because the mechanical driving forces are not as great, allowing time for deleterious environmental effects to manifest.

To investigate the degree to which different mechanical and environmental loading conditions influence the growth rate, additional experiments were performed and compared with the plateau data from Figure 43 and Figure 45. Figure 60 plots the K_{\max} versus the da/dt which enables analysis of the effect of loading parameters on the four driving forces influencing crack growth behavior. Fatigue performed at $R=0.5$ is indicated by the triangular data sets inside the light blue ellipse. Higher R fatigue is found outside of this ellipse. A K_{ISCC} threshold value from quasi-static SCC testing ($>72\text{MPa}\sqrt{\text{m}}$) is denoted by the vertical red line. The green line shows the range of diffusion-limited maximum da/dt values that were observed in the quasi-static testing for conditions where SCC will occur. This is not plotted at appropriate K values and is included just to show the range of pure SCC cracking rates [115]. There are two additional tests to note. Test 1 is denoted by the green circles and was held at a decreasing K_{\max} of $55\text{MPa}\sqrt{\text{m}}$ to $5\text{MPa}\sqrt{\text{m}}$ and fatigued with a ripple load $\Delta K=1\text{MPa}\sqrt{\text{m}}$, effectively decreasing in R from 0.98 for the data point at $55\text{MPa}\sqrt{\text{m}}$ to 0.8 for the data point at $5\text{MPa}\sqrt{\text{m}}$. Test 2 is denoted by the blue circles and fatigued with a ripple load of $R=0.95$, effectively decreasing ΔK from $2.75\text{MPa}\sqrt{\text{m}}$ at a K_{\max} of $55\text{MPa}\sqrt{\text{m}}$ to $1\text{MPa}\sqrt{\text{m}}$ at a K_{\max} of $20\text{MPa}\sqrt{\text{m}}$.

Higher da/dt was produced by $R=0.5$ than at $R=0.95$ despite environmental consistency. The contribution of da/dN_{vac} should apply equally to all tests, eliminating this driving force as a cause. K_{\max} is below the SCC_{mono} threshold, also eliminating da/dN_{SCC} as an explanation. It was hypothesized that low- R fatigue was driven both by corrosion fatigue and cyclic-SCC. The low ΔK associated with high- R fatigue was insufficient to exceed the corrosion fatigue K_{TH} , so these cracks propagate at a slower rate as they are driven only by $da/dn_{\text{SCC-cyclic}}$. Fractography in Figure 61 supports this hypothesis, as both intergranular and transgranular features are seen in low- R tests, corresponding to the contributions of SCC_{cyclic} and corrosion fatigue, respectively.

The importance of the ripple load effect ($da/dN_{\text{SCC-cyclic}}$) is clear when looking at the high- R crack growth rates (blue and green circles in Figure 60). Although these rates are not as fast as those achieved from low- R fatigue, significant crack growth rates are observed repeatedly at very low K_{\max} in both Test 1 and Test 2. Test 2 demonstrates significant stage II crack growth at a constant $R=0.95$ down to a K_{\max} of $20\text{MPa}\sqrt{\text{m}}$. Test 1 exhibits even faster stage II cracking

with respect to K at a constant ΔK and maintains a significant crack growth rate down to a K_{\max} of as little as $5\text{MPa}\sqrt{\text{m}}$. Comparing the mechanical parameters of these two tests shows that as K_{\max} decreases, decreasing R and a small ΔK reduces K_{TH} more severely than a constant R and a decreasing ΔK . Test 1 also shows that ripple-load induced SCC can occur at higher K , evidenced by the SCC at high ΔK where $R > 0.95$. Rigorous quantitative comparison of the da/dt values between Test 1 and 2 is complicated by the shifting potentials for the $R=0.95$ data but regardless these data strongly illustrate the importance of high R ripple loads in inducing cracking well below quasi-state K_{ISCC} .

It is shown here that C465-H950 experiences deleterious ripple load effects inducing cyclic SCC at R at very low ripple loads ($\Delta K=1\text{MPa}\sqrt{\text{m}}$ and $R=0.95$), representing extremely mild cyclic loading conditions. The presence of cyclic-SCC-induced subthreshold cracking complicates traditional design criteria by enabling substantial crack propagation well below the measured and expected ΔK_{TH} and K_{ISCC} . As such, an understanding of ripple load effects in these SCC-inducing environments is critically important for the design of structural components subject to corrosive conditions.

Appendix A Figures

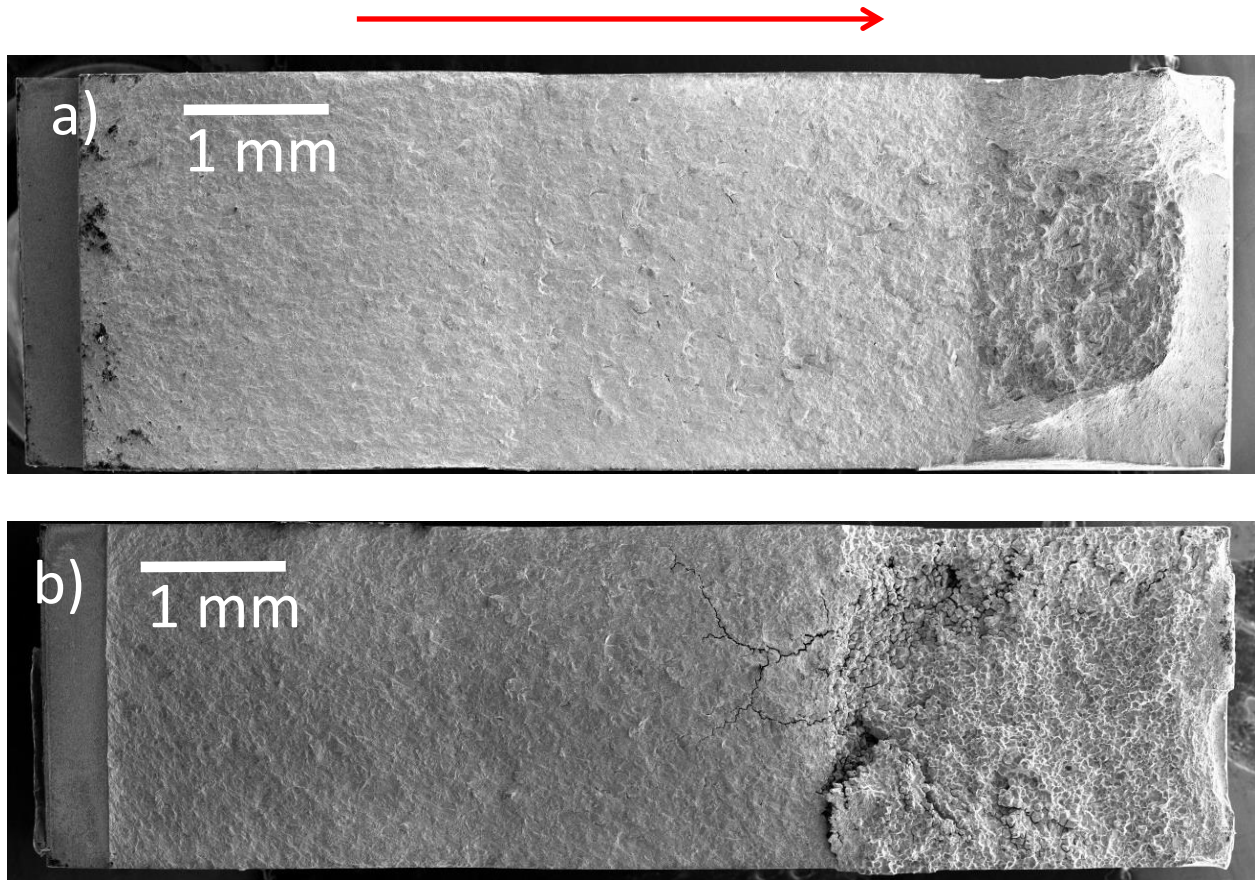


Figure 53: Overview shots of two Phase I tests fatigued at an $R=0.5$, $f=2$ and a nominal stress of 300MPa for the increasing- K test and fatigued at $K_{\max}=55\text{MPa}\sqrt{\text{m}}$ and a decreasing- ΔK starting at $20\text{MPa}\sqrt{\text{m}}$ to threshold or failure. Both specimens were polarized to $-200\text{mV}_{\text{SCE}}$. The crack initiates at the notch on the right and propagates in the direction given by the red arrow. The fracture surface in (a) is from a specimen that was fatigued in 0.0006M aqueous NaCl , and the fracture surface in (b) is from a specimen that was fatigued in 0.6M aqueous NaCl . Both tests were polarized to $-200\text{mV}_{\text{SCE}}$.

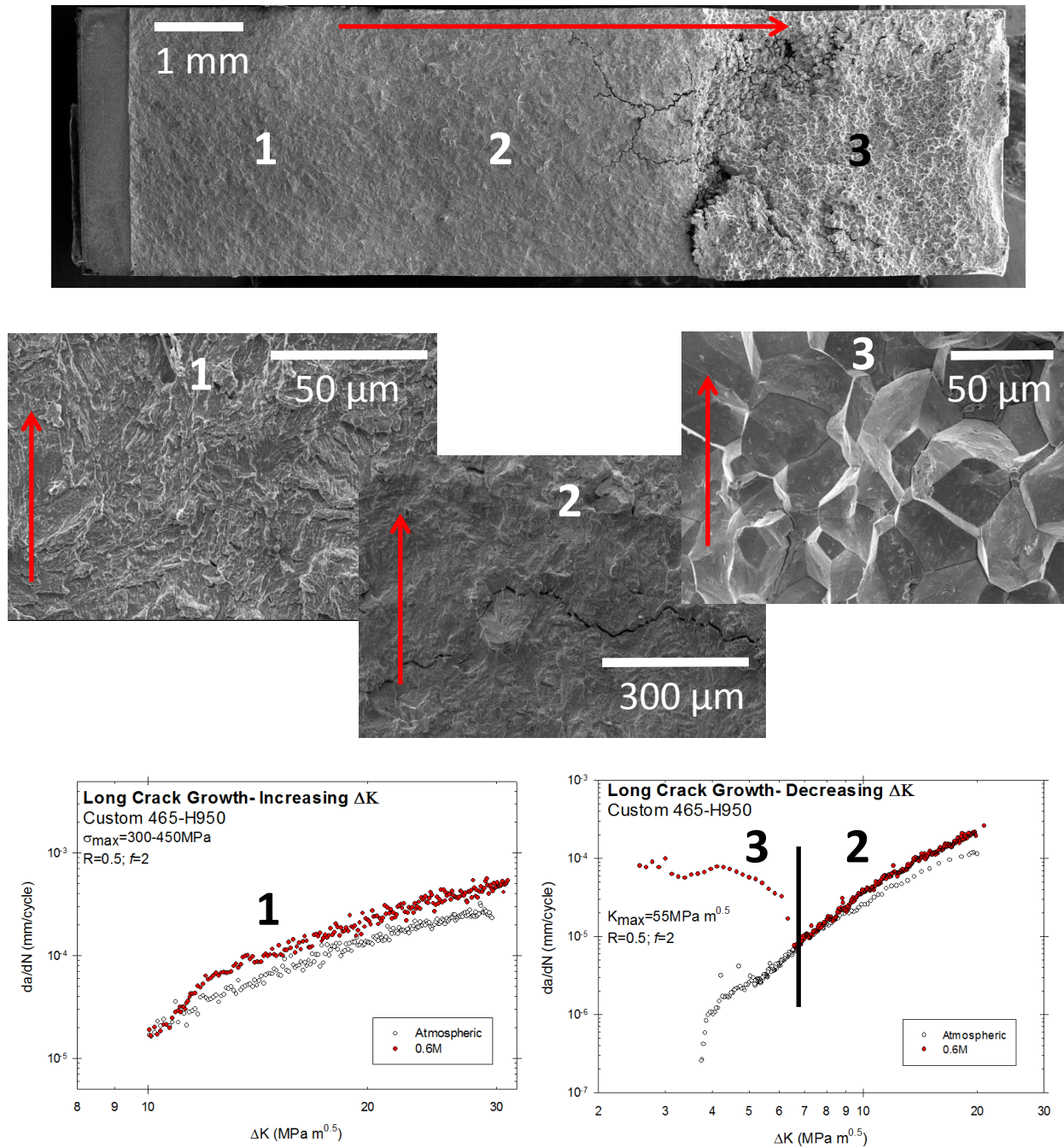


Figure 54: This figure breaks down the fracture morphology of a C465-H950 SEN specimen fatigued in a 0.6M NaCl solution polarized to -200mV_{SCE} in accordance with the increasing- K protocol where $R=0.5$, $f=2$, nominal stress = 300MPa, and the decreasing- K protocol where $K_{max}=55\text{MPa}\sqrt{\text{m}}$, $f=2$. Red arrows show the direction of crack propagation.

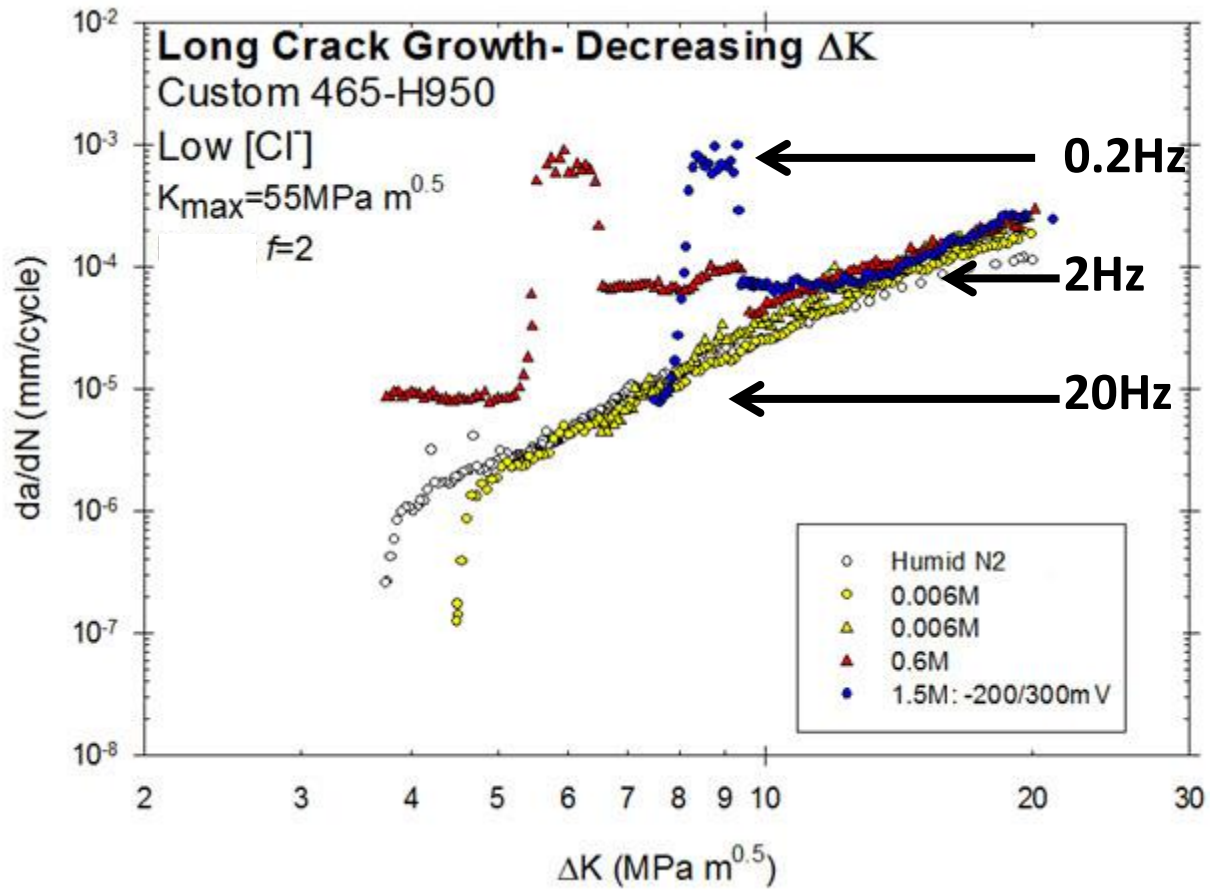


Figure 55: An abridged plot of decreasing- ΔK crack growth rates is presented to show the effect of frequency modulation. All fatigue was conducted with a K_{max} of $55\text{MPa}\sqrt{\text{m}}$ and polarized to -200mV_{SCE} .

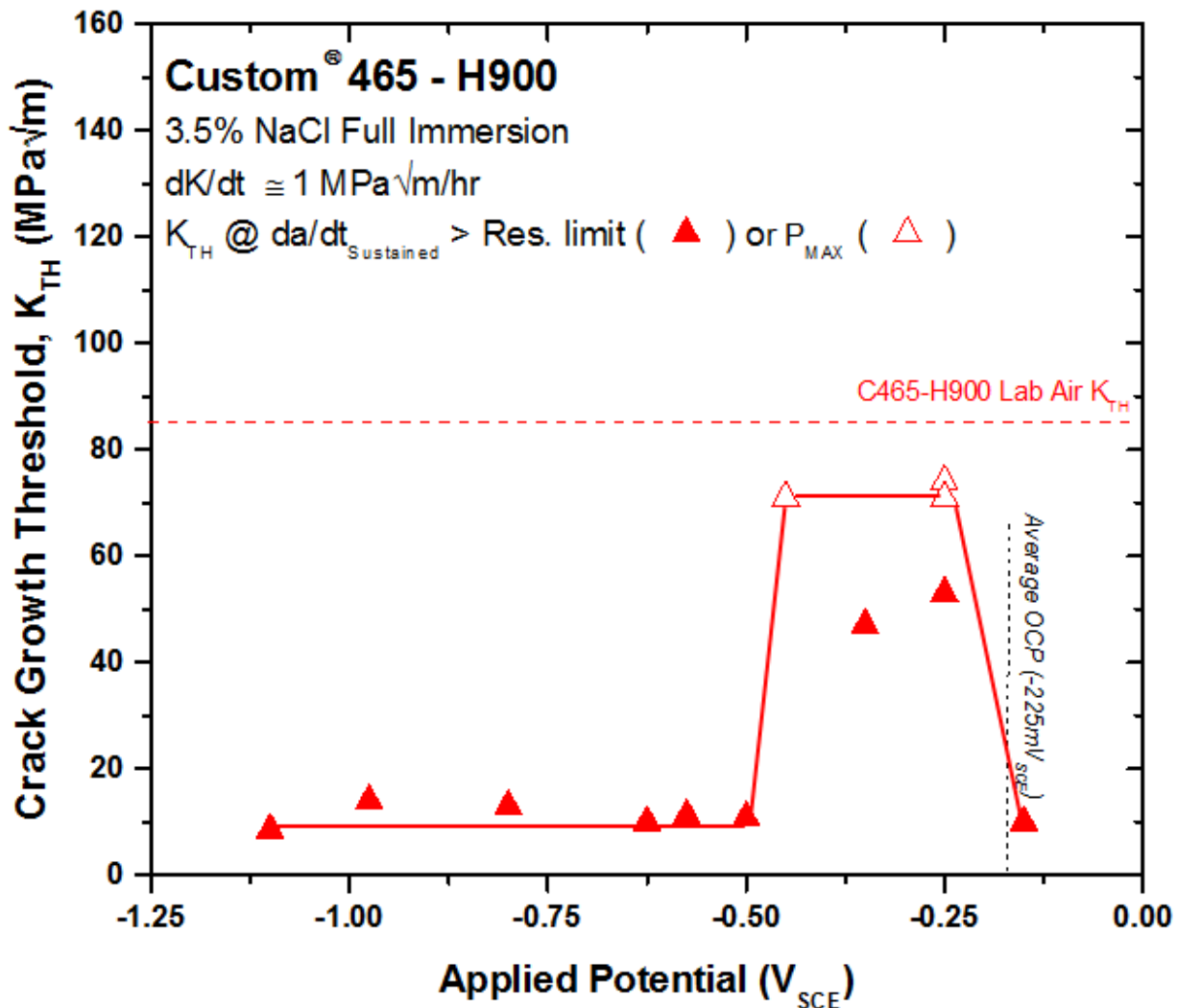


Figure 56: Threshold stress intensity (K_{TH}) vs. applied potential (E_{app}) for Custom465 stressed in 0.6 M NaCl at an increasing- K rate of 1MPa√m/hr. Open triangles indicate tests reaching maximum nominal load with no resolvable hydrogen-assisted crack growth. Reproduced from Pioszak 2013 [115].

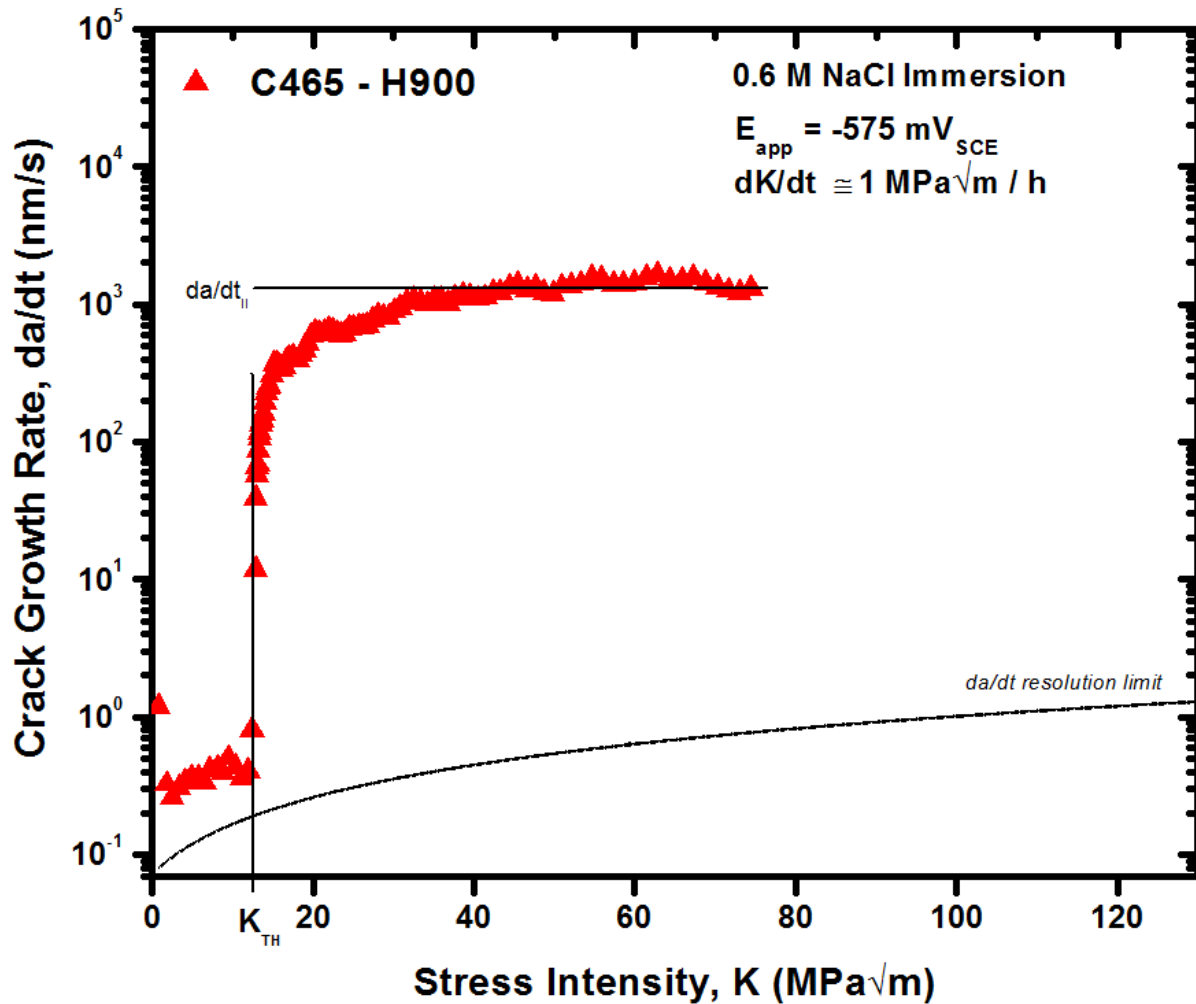


Figure 57: Monotonic tensile testing performed showing K_{TH} , given by the sudden onset of stage I crack growth, and stage II crack growth rates. This test was performed on C465-H900 in 0.6M NaCl at an applied potential of -575mV_{SCE} . K rose at a rate of $1\text{MPa}\sqrt{\text{m}}/\text{hr}$. Reproduced from Pioszak 2013 [115].

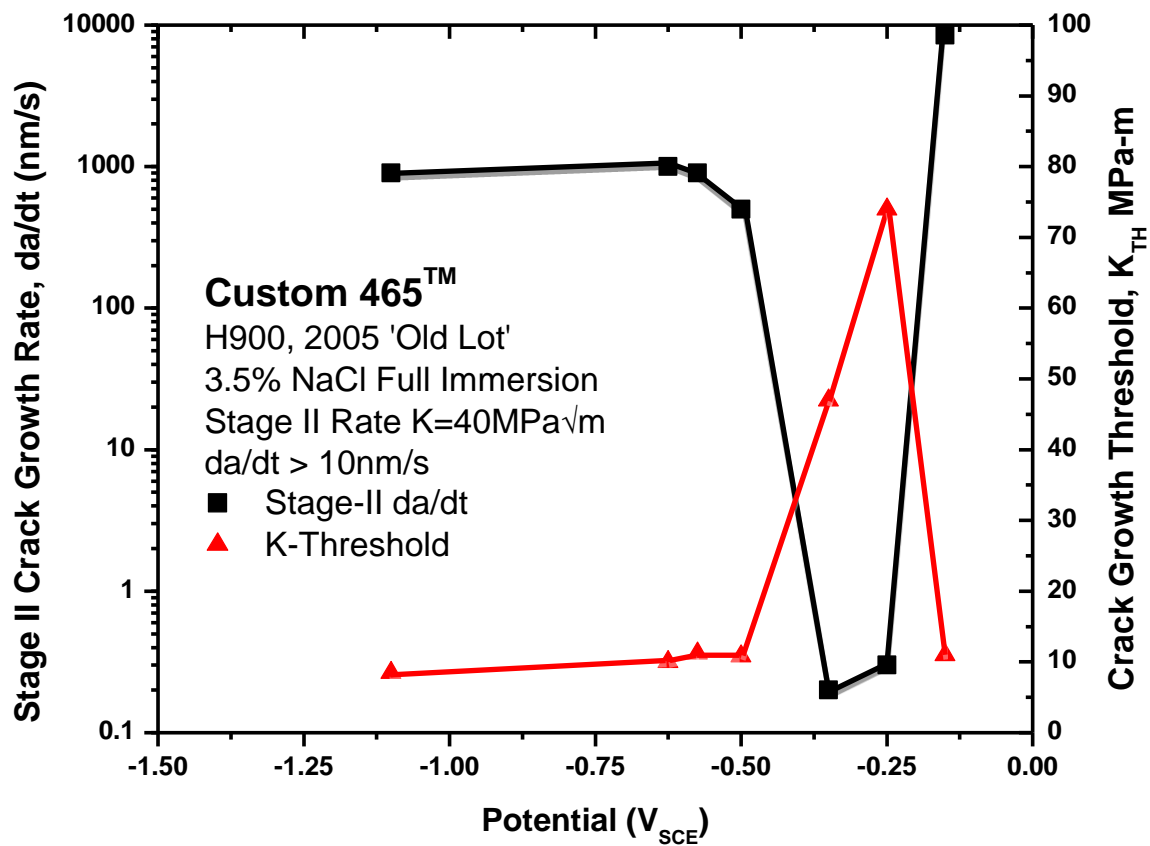


Figure 58: Monotonically increasing- K stage II crack growth rates with respect to applied potential are plotted for C465-H900 in 0.6M NaCl at a $K=40\text{MPa}\sqrt{\text{m}}$. Reproduced from Pioszak 2013 [115].

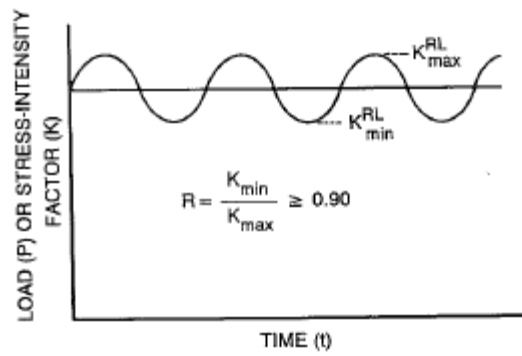


Fig. 3(a)

Yoder A

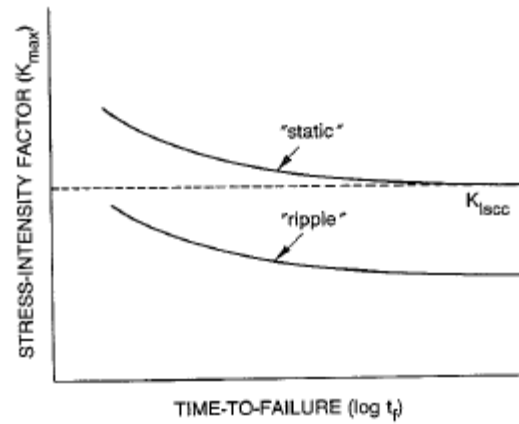


Fig. 3(b)

Figure 59: Ripple loading protocol and its potential effect on K_{ISCC} is visually represented. The small cyclic load superimposed over constant monotonic tension seen in (a) effectively reduces K_{ISCC} in many materials shown schematically in (b) [158].

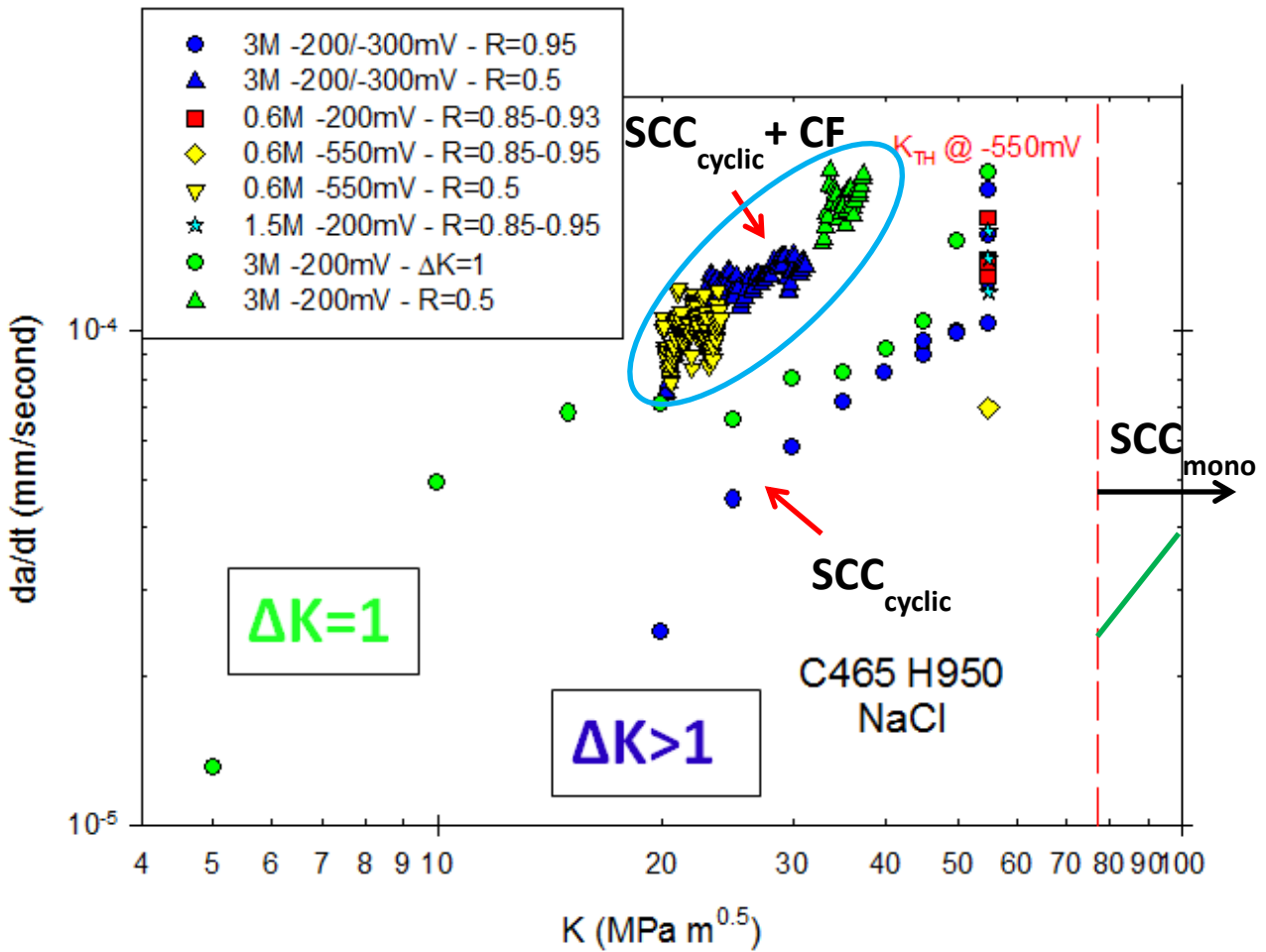


Figure 60: This plot summarizes sub-threshold crack growth in different environments at different loading parameters. Testing was conducted in accordance to increasing and decreasing- K fatigue parameters at $f=2$ and the applied potential of $-200mV_{SCE}$. Further conditions specific to individual tests are noted in the legend.

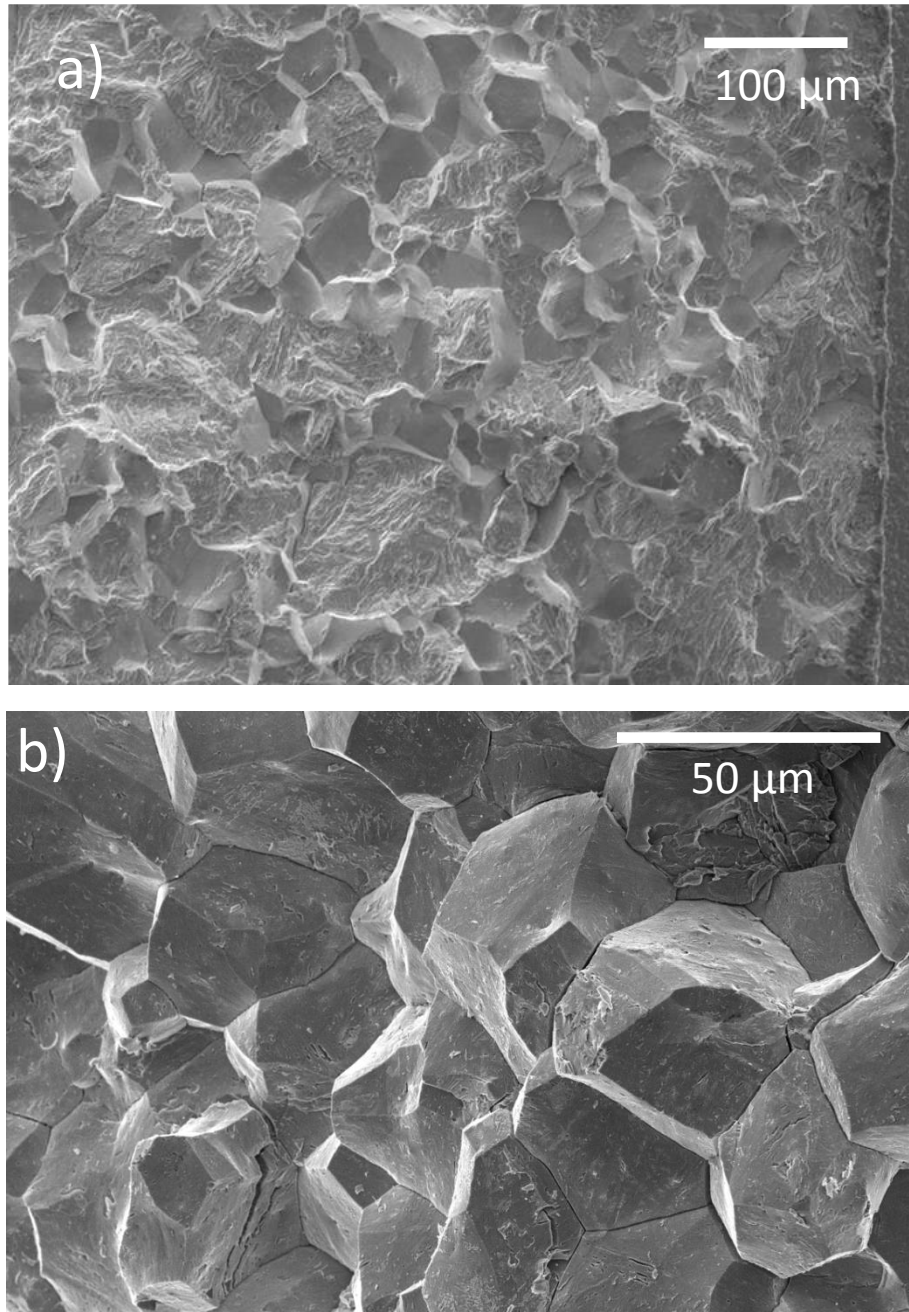


Figure 61: Micrographs show different fracture modes in Phase I testing. Mixed fracture modes in (a) are observed at an $R=0.5$, an $f=2$, and a nominal stress of 300MPa in a 3.0M NaCl solution polarized to $-200\text{mV}_{\text{SCE}}$, subject to the increasing- K loading protocol (b) shows tests conducted at a K_{max} of $55\text{MPa}\sqrt{\text{m}}$ in 3.0M NaCl polarized to $-200\text{mV}_{\text{SCE}}$ subject to a $\Delta K=1\text{MPa}\sqrt{\text{m}}$.

Appendix B

The one test conducted in chlorine-free deionized water produced some unexpected and remarkable results shown in Figure 62. This environment was hypothesized to produce growth rates and behavior most similar to low $[Cl^-]$ and atmospheric testing because of the lack of chlorides so often the culprit of environmental damage failure. During increasing-K testing, this environment produced the highest growth rates of any environment from a ΔK of approximately $17\text{MPa}\sqrt{\text{m}}$ to the conclusion of the regime. High growth rates continued into the decreasing-K regime until falling to a ΔK of approximately $12.3\text{MPa}\sqrt{\text{m}}$ at which a da/dN plateau formed. Fractography (Figure 63) shows transgranular mechanisms dominant in early stages of crack growth followed a mixed, increasingly intergranular fracture mode until the later mode was exclusive.

Though this behavior is highly unexpected, it is not unprecedented. Prior work recently performed by Kalnaus and Weng investigated SCC in 4340 steel in a variety of chloride environments and distilled water [146, 147]. Results reported in Figure 64 show the effects of $[Cl^-]$ on da/dt_{II} . Stage II crack growth exposed to a distilled water environment was greater than the rates observed in tests performed in aqueous chloride environments in which $[Cl^-]$ ranged from 0.0006-0.6M. Intergranular fracture, presumably associated with SCC, is observed in the distilled water test. The environmental and mechanistic causes of this unexpected behavior are outside the scope of this work.

Appendix B Figures

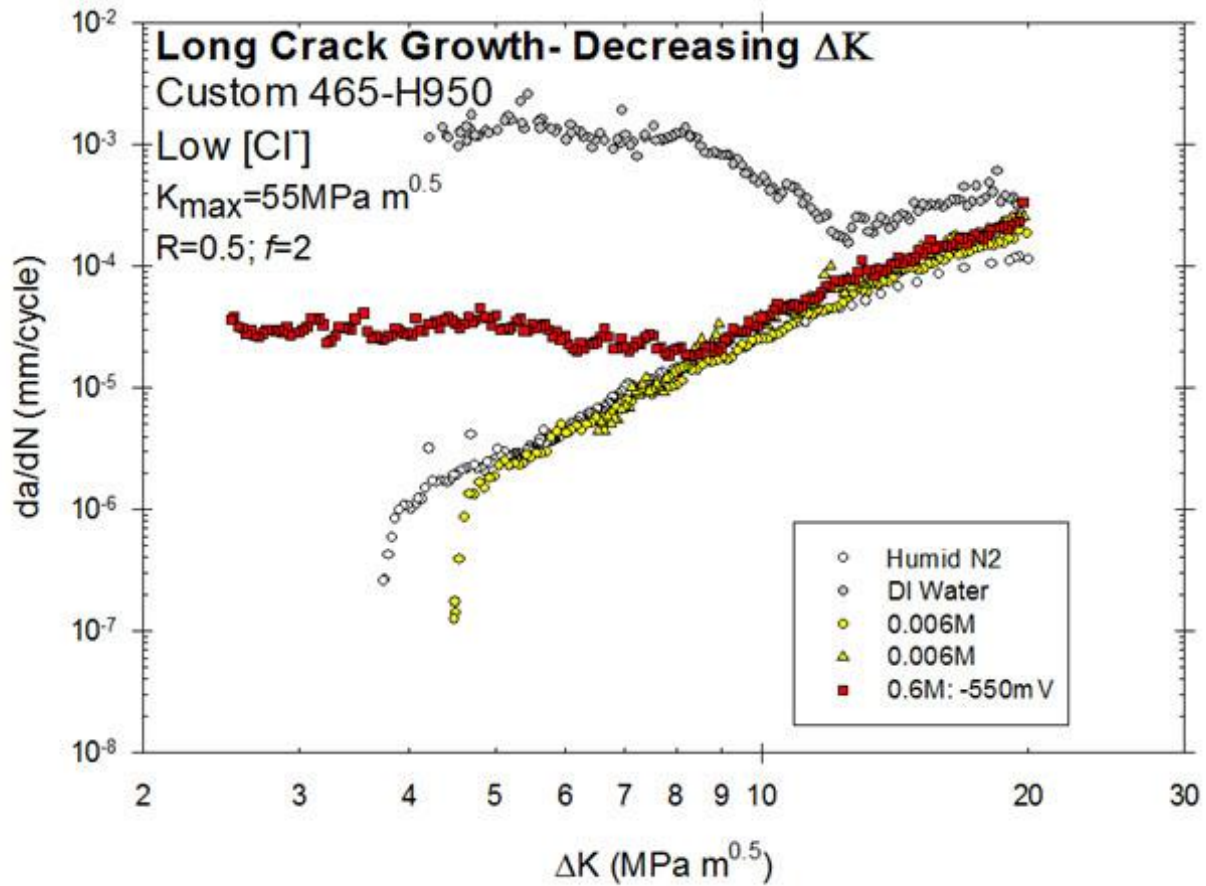


Figure 62: This plot is an abridged version of the Phase I decreasing- K data in order to show the unusual crack growth behavior induced by the chloride-free water environment. All fatigue is conducted at $f=2$, a K_{max} of $55\text{MPa}\sqrt{\text{m}}$, and a decreasing ΔK to either threshold or failure.

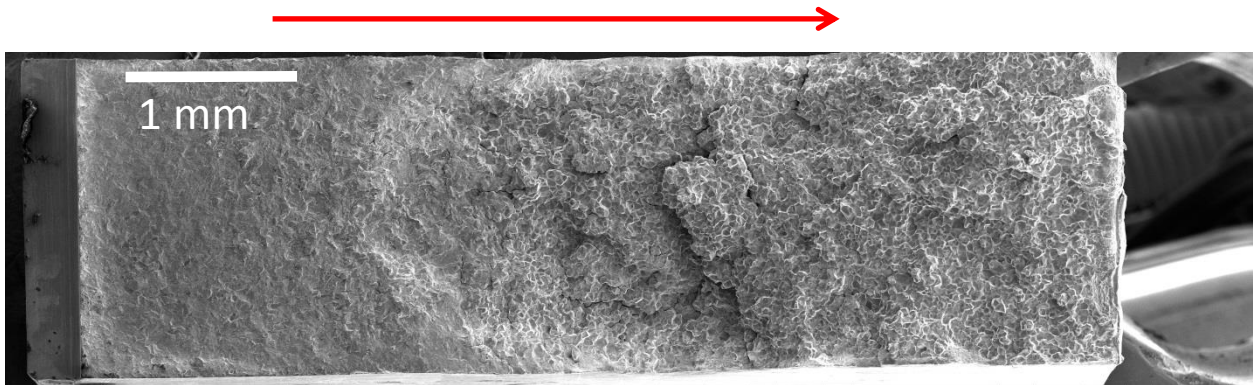


Figure 63: Fracture surface taken from the DI water test fatigued in accordance to increasing and decreasing- K protocol at the OCP. The red arrow indicated direction of crack propagation.

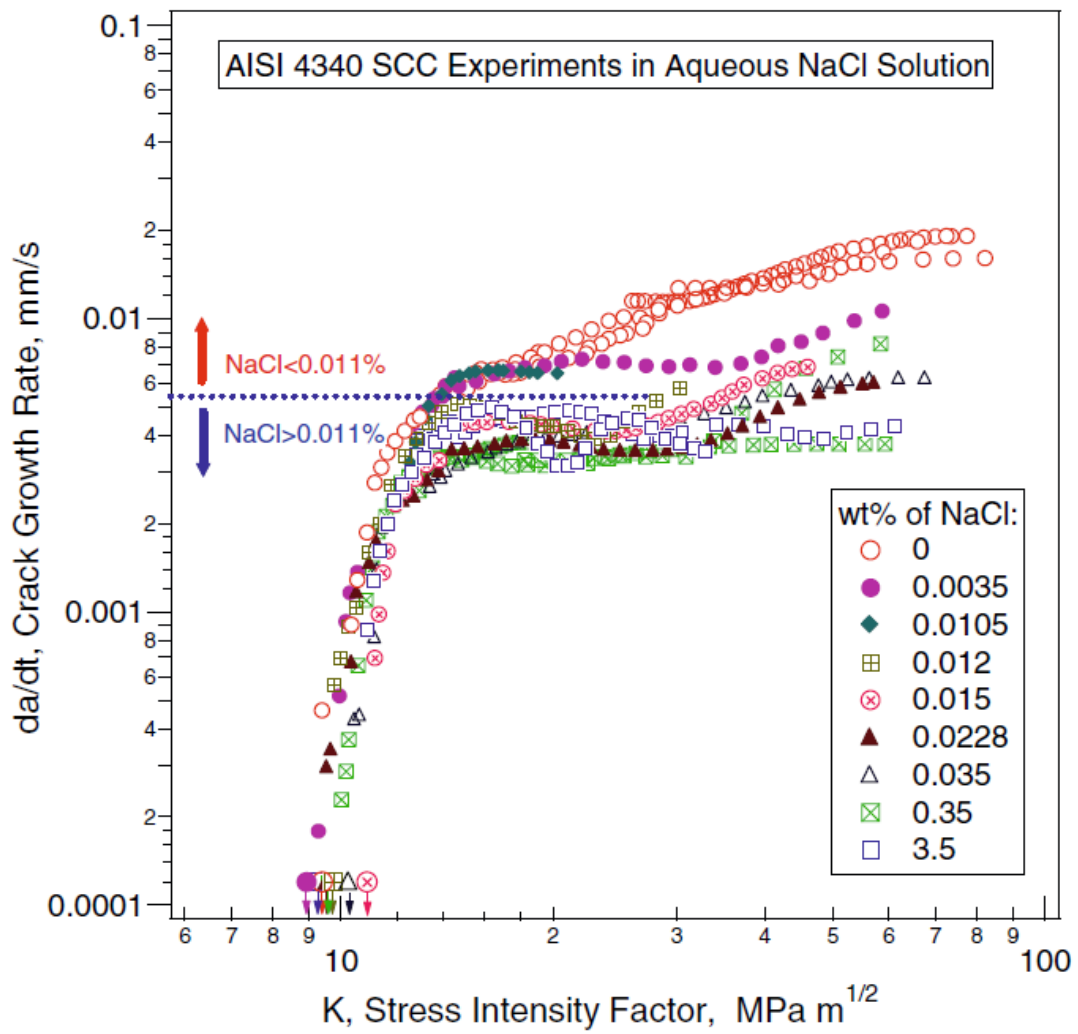


Figure 64: Other research has also reported unusually rapid SCC-induced stage II crack growth behavior in a chloride-free water environment. Reproduced from Kalnaus 2011 [146].

6 References

1. Hyatt, M., R. Caton, and D. Lovell, Advanced materials development in commercial aircraft, in Aircraft Design and Operations Meeting 1989, American Institute of Aeronautics and Astronautics.
2. Lovell, D. and M. Disotell, Structural material trends in commercial aircraft, in Conference on Air Transportation: Technical Perspectives and Forecasts 1978, American Institute of Aeronautics and Astronautics.
3. Hale, J., Boeing 787: From the ground up, in Aeromagazine 2006, Boeing.
4. Leygraf, C. and T.E. Graedel, Atmospheric Corrosion 2000, New York, NY: John Wiley & Sons.
5. Schindelholz, E. and R.G. Kelly, Wetting phenomena and time of wetness in atmospheric corrosion: a review. Corrosion Reviews, 2012. 30(5-6): p. 135-170.
6. Hata, S., et al., Investigation of Corrosion Fatigue Phenomena in Transient Zone and Preventive Coating and Blade Design against Fouling and Corrosive Environment for Mechanical Drive Turbines. International Journal of Fluid Machinery and Systems, 2008. 1(1): p. 121-139.
7. Lin, C.K., W.C. Fan, and W.J. Tsai, Corrosion Fatigue of Precipitation-Hardening Martensitic Stainless Steel. Corrosion, 2002. 58(11): p. 904-911.
8. Lin, C.K. and W.J. Tsai, Corrosion fatigue behaviour of a 15Cr-6Ni precipitation-hardening stainless steel in different tempers. Fatigue & Fracture of Engineering Materials & Structures, 2000. 23(6): p. 489-497.
9. Ragab, A., H. Alawi, and K. Sorein, Corrosion fatigue of steel in various aqueous environments. Fatigue & Fracture of Engineering Materials & Structures, 1989. 12(6): p. 469-479.
10. Islam, M., G. Campbell, and R. Hsu, FATIGUE AND TENSILE PROPERTIES OF EB WELDED 17-4 PH STEEL-EVALUATION SHOWED THAT EBW RESULTED IN MINIMAL LOSS IN TENSILE-STRENGTH. Welding Journal, 1989. 68(9): p. 45-50.
11. Beutner, T., et al., Sea-Based Aviation: A National Naval Responsibility, 2011, ONR: Arlington, VA.
12. Cole, G.K., G. Clark, and P.K. Sharp, The implication of corrosion with respect to aircraft structural integrity, Report DSTO-RR-0201, 1997: Melbourne, Australia.
13. Hoffman, M.E. and P.C. Hoffman, Corrosion and fatigue research - structural issues and relevance to naval aviation. International Journal of Fatigue, 2001. 23: p. S1-S10.
14. Burns, J.T. and R.P. Gangloff, Scientific advances enabling next generation management of corrosion induced fatigue. Procedia Engineering, 2011. 10(International Conference on the Mechanical Behavior of Materials): p. 362-369.
15. Goranson, U.G., Fatigue issues in aircraft maintenance and repairs. International Journal of Fatigue, 1998. 20(6): p. 413-431.
16. Bray, G.H., R.J. Bucci, and R.L. Brazil, Lessons neglected: effects of moist air on fatigue and fatigue crack growth in aluminum alloys. Mat Sci Forum, 2000. 331-337: p. 1143-1156.
17. Garrison, W.M., Jr., Ultrahigh-strength steels for aerospace applications. JOM, 1990. 42(5): p. 20-24.
18. Miyata, K., et al., Coarsening kinetics of multicomponent MC-type carbides in high-strength low-alloy steels. Metallurgical and Materials Transactions A, 2003. 34(8): p. 1565-1573.
19. Xu, W., P.E.J. Rivera-Díaz-del-Castillo, and S. van der Zwaag, Designing nanoprecipitation strengthened UHS stainless steels combining genetic algorithms and thermodynamics. Computational Materials Science, 2008. 44(2): p. 678-689.
20. Figueroa, D. and M.J. Robinson, The effects of sacrificial coatings on hydrogen embrittlement and re-embrittlement of ultra high strength steels. Corrosion Science, 2008. 50(4): p. 1066-1079.
21. Xu, W., et al., Genetic design and characterization of novel ultra-high-strength stainless steels strengthened by Ni₃Ti intermetallic nanoprecipitates. Acta Materialia, 2010. 58(10): p. 3582-3593.
22. Sedriks, A.J., Corrosion of stainless steel, 2. edition. Other Information: PBD: 19961996. Medium: X; Size: [200] p.
23. Olsson, C.O.A. and D. Landolt, Passive films on stainless steels—chemistry, structure and growth. Electrochimica Acta, 2003. 48(9): p. 1093-1104.
24. Lizlovs, E.A. and A.P. Bond, Anodic Polarization Behavior of High-Purity 13 and 18% Cr Stainless Steels. Journal of The Electrochemical Society, 1975. 122(6): p. 719-722.
25. Ilevbare, G.O. and G.T. Burstein, The role of alloyed molybdenum in the inhibition of pitting corrosion in stainless steels. Corrosion Science, 2001. 43(3): p. 485-513.

26. McGuire, M.F., *Stainless Steels for Design Engineers*, ASM International.
27. Grujicic, M., et al., Effect of iron additions on structure of Laves phases in Nb-Cr-Fe alloys. *Materials Science and Engineering: A*, 1993. 160(1): p. 37-48.
28. Hochanadel, P.W., et al., Heat treatment of investment cast PH 13-8 Mo stainless steel: Part I. Mechanical properties and microstructure. *Metallurgical and Materials Transactions A*, 1994. 25(4): p. 789-798.
29. Lee, E.U., et al., *Aircraft Steels*. DTIC- Naval air warfare center, Aircraft division, 2009.
30. Carpenter. Custom 465 Stainless- Technical Datasheet. 2013 05/17/13 11/25/13]; Available from: <http://cartech.ides.com/datasheet.aspx?i=103&e=55>.
31. Grujicic, M., et al., A linear friction welding process model for Carpenter Custom 465 precipitation-hardened martensitic stainless steel: A weld microstructure-evolution analysis. *Proceedings of the Institution of Mechanical Engineers, Part B: Journal of Engineering Manufacture*, 2014: p. 0954405414542137.
32. Syrett, B.C., et al., Effect of Microstructure on Pitting and Corrosion Fatigue of 17-4 PH Turbine Blade Steel in Chloride Environments. *Corrosion*, 1982. 38(5): p. 273-282.
33. Perkins, K.M. and M.R. Bache, Corrosion fatigue of a 12%Cr low pressure turbine blade steel in simulated service environments. *International Journal of Fatigue*, 2005. 27(10-12): p. 1499-1508.
34. Ritchie, R. and J. Lankford, *Small fatigue cracks: A statement of the problem and potential solutions*, 1986, The Metallurgical Society Inc., Warrendale, PA.
35. Gangloff, R.P., *Corrosion fatigue crack propagation in metals*. 1990.
36. Turnbull, A., The environmentally small/short crack growth effect: current understanding. *Corrosion Reviews*, 2012. 30(1-2): p. 1-17.
37. Ernst, P. and R.C. Newman, Pit growth studies in stainless steel foils. I. Introduction and pit growth kinetics. *Corrosion Science*, 2002. 44(5): p. 927-941.
38. Ernst, P. and R.C. Newman, Pit growth studies in stainless steel foils. II. Effect of temperature, chloride concentration and sulphate addition. *Corrosion Science*, 2002. 44(5): p. 943-954.
39. Frankel, G.S., Pitting Corrosion of Metals: A Review of the Critical Factors. *Journal of The Electrochemical Society*, 1998. 145(6): p. 2186-2198.
40. Galvele, J.R., Transport Processes and the Mechanism of Pitting of Metals. *Journal of The Electrochemical Society*, 1976. 123(4): p. 464-474.
41. Punckt, C., et al., Sudden Onset of Pitting Corrosion on Stainless Steel as a Critical Phenomenon. *Science*, 2004. 305(5687): p. 1133-1136.
42. Ryan, M.P., et al., Corrosion Pits in Thin Films of Stainless Steel. *Journal of The Electrochemical Society*, 1999. 146(1): p. 91-97.
43. Ryan, M.P., et al., Why stainless steel corrodes. *Nature*, 2002. 415(3873): p. 770-774.
44. Williams, D.E., C. Westcott, and M. Fleischmann, Stochastic Models of Pitting Corrosion of Stainless Steels: I. Modeling of the Initiation and Growth of Pits at Constant Potential. *Journal of The Electrochemical Society*, 1985. 132(8): p. 1796-1804.
45. Zhou and Turnbull, Influence of pitting on the fatigue life of a turbine blade steel. *Fatigue & Fracture of Engineering Materials & Structures*, 1999. 22(12): p. 1083-1093.
46. Williams, D.E., et al., Passivity breakdown and pitting corrosion of binary alloys. *Nature*, 1991. 350(6315): p. 216-219.
47. Wranglen, G., Pitting and sulphide inclusions in steel. *Corrosion Science*, 1974. 14(5): p. 331-349.
48. Eklund, G.S., Initiation of Pitting at Sulfide Inclusions in Stainless Steel. *Journal of The Electrochemical Society*, 1974. 121(4): p. 467-473.
49. Baker, M.A. and J.E. Castle, The initiation of pitting corrosion at MnS inclusions. *Corrosion Science*, 1993. 34(4): p. 667-682.
50. Szklarska-smialowska, Z. and E. Lunarska, The effect of sulfide inclusions on the susceptibility of steels to pitting, stress corrosion cracking and hydrogen embrittlement. *Materials and Corrosion*, 1981. 32(11): p. 478-485.
51. Webb, E.G. and R.C. Alkire, Pit Initiation at Single Sulfide Inclusions in Stainless Steel: I. Electrochemical Microcell Measurements. *Journal of The Electrochemical Society*, 2002. 149(6): p. B272-B279.
52. Stewart, J. and D.E. Williams, The initiation of pitting corrosion on austenitic stainless steel: on the role and importance of sulphide inclusions. *Corrosion Science*, 1992. 33(3): p. 457-474.

53. Ke, R. and R. Alkire, Surface Analysis of Corrosion Pits Initiated at MnS Inclusions in 304 Stainless Steel. *Journal of The Electrochemical Society*, 1992. 139(6): p. 1573-1580.
54. Turnbull, A., Corrosion pitting and environmentally assisted small crack growth. *Proceedings. Mathematical, Physical, and Engineering Sciences / The Royal Society*, 2014. 470(2169): p. 20140254.
55. Gavriljuk, V.G. and H. Berns. Precipitates in tempered stainless martensitic steels alloyed with nitrogen, carbon or both. in *Materials Science Forum*. 1999. Trans Tech Publ.
56. Klueh, R.L., N. Hashimoto, and P.J. Maziasz, Development of new nano-particle-strengthened martensitic steels. *Scripta Materialia*, 2005. 53(3): p. 275-280.
57. Padilha, A.F., G. Schanz, and K. Anderko, Ausscheidungsverhalten des titanstabilisierten austenitischen stahls 15% Cr-15% Ni-1% Mo-Ti-B (Din-werkstoff-nr. 1.4970). *Journal of Nuclear Materials*, 1982. 105(1): p. 77-92.
58. Leitnaker, J.M. and J. Bentley, Precipitate phases in type 321 stainless steel after aging 17 years at ~ 600° C. *Metallurgical Transactions A*, 1977. 8(10): p. 1605-1613.
59. Kimura, M., et al., Corrosion Resistance of High-Strength Modified 13% Cr Steel. *Corrosion*, 1999. 55(8): p. 756-761.
60. Merello, R., et al., Influence of chemical composition on the pitting corrosion resistance of non-standard low-Ni high-Mn-N duplex stainless steels. *Corrosion Science*, 2003. 45(5): p. 909-921.
61. Kim, J., et al., Effect of alloying elements on the contact resistance and the passivation behaviour of stainless steels. *Corrosion Science*, 2002. 44(4): p. 635-655.
62. Stratmann, M. and H. Streckel, On the atmospheric corrosion of metals which are covered with thin electrolyte layers—II. Experimental results. *Corrosion Science*, 1990. 30(6-7): p. 697-714.
63. Gangloff, R.P., Crack size effects on the chemical driving force for aqueous corrosion fatigue. *Metallurgical Transactions A*, 1985. 16(5): p. 953-969.
64. Gangloff, R.P., Corrosion fatigue crack propagation in metals, in *Environment Induced Cracking of Metals*, R.P. Gangloff and M.B. Ives, Editors. 1990, NACE: Houston, TX. p. 55-110.
65. Kondo, Y., Prediction of fatigue crack initiation life based on pit growth. *Corrosion*, 1989. 45(1): p. 7-11.
66. Muto, I., E. Sato, and S. Ito, Pitting Corrosion Behavior of Stainless Steels in a Marine Environment and Its Estimation Method. *CORROSION ENGINEERING-ENGLISH EDITION-*, 1993. 42: p. 877-877.
67. Shedd, M.E. and R.G. Kelly, The Modeling and Measurement of Boundary Conditions for Pit Size on Stainless Steels under Atmospheric Exposure Conditions. *ECS Transactions*, 2012. 41(25): p. 31-37.
68. Moller, G. The successful use of austenitic stainless steels in sea water. in *Offshore Technology Conference 1976*.
69. Leckie, H.P. and H.H. Uhlig, Environmental Factors Affecting the Critical Potential for Pitting in 18-8 Stainless Steel. *Journal of The Electrochemical Society*, 1966. 113(12): p. 1262-1267.
70. Schaller, R., Atmospheric Hydrogen Uptake in Ultra-High Strength Steels (Proposal). *Proposal*, 2014.
71. Rusk, D.T. and W. Hoppe, Fatigue life prediction of corrosion-damaged high-strength steel using an equivalent stress riser (ESR) model: Part I: Test development and results. *International Journal of Fatigue*, 2009. 31(10): p. 1454-1463.
72. Burns, J.T., J.M. Larsen, and R.P. Gangloff, Driving forces for localized corrosion-to-fatigue crack transition in Al-Zn-Mg-Cu. *Fatigue & Fracture of Engineering Materials & Structures*, 2011. 34(10): p. 745-773.
73. Turnbull, A., The solution composition and electrode potential in pits, crevices and cracks. *Corrosion Science*, 1983. 23(8): p. 833-870.
74. Cooper, K.R. and R.G. Kelly, Crack tip chemistry and electrochemistry of environmental cracks in AA 7050. *Corrosion Science*, 2007. 49(6): p. 2636-2662.
75. McEvily, A.J. and R.P. Wei, Fracture mechanics and corrosion fatigue, in *Corrosion Fatigue: Chemistry, Mechanics, and Microstructure*, NACE-2, A.J. McEvily and R.W. Staehle, Editors. 1972, NACE: Houston, TX. p. 381-395.
76. Gangloff, R.P., Corrosion fatigue crack propagation in metals, in *Environment-Induced Cracking of Metals*, R.P. Gangloff and M.B. Ives, Editors. 1990, NACE: Houston, TX. p. 55-110.
77. Paris, P.C., R.J. Bucci, and C.D. Little, Fatigue crack propagation of D6ac steel in air and distilled water, in *Stress Analysis and Growth of Cracks*, ASMT STP 5131972, ASTM: West Conshohocken, PA. p. 196-217.

78. Weng, L., et al., Corrosion fatigue crack growth of AISI 4340 steel. *International Journal of Fatigue*, 2013. 48: p. 156-164.
79. Wei, R.P. and M. Gao, Reconsideration of the superposition model for environmentally assisted fatigue crack growth. *Scripta Metallurgica*, 1983. 17(7): p. 959-962.
80. Crooker, T.W. and J.A. Hauser, A literature review on the influence of small-amplitude cyclic loading on stress-corrosion cracking in alloys, 1986, Naval Research Laboratory: Arlington, VA.
81. Mendoza, J.A. and J.M. Sykes, The Effect of Low-Frequency Cyclic Stresses on the Initiation of Stress-Corrosion Cracks in X60-Line Pipe Steel in Carbonate Solutions. *Corrosion Science*, 1983. 23(6): p. 547-558.
82. Parkins, R.N. and B.S. Greenwell, The interface between corrosion fatigue and stress-corrosion cracking. *Metal Science*, 1977: p. 405-413.
83. Ford, F.P. and M. Silverman, Effect of Loading Rate on Environmentally Controlled Cracking of Sensitized-304 Stainless-Steel in High-Purity Water. *Corrosion*, 1980. 36(11): p. 597-603.
84. Pao, P.S., et al., On ripple-load, stress-corrosion, and sustained-load cracking behavior in a high strength beta titanium alloy. *Scripta Materialia*, 1997. 36(11): p. 1321-1326.
85. Gerberich, W.W., J.P. Birat, and V.F. Zackay, On the superposition model for environmentally-assisted fatigue crack propagation, in *Corrosion Fatigue: Chemistry, Mechanics, and Microstructure*; NACE 2, A.J. McEvily and R.W. Staehle, Editors. 1972, NACE: Houston, TX.
86. Staehle, R.W., et al., eds. *Stress Corrosion Cracking and Hydrogen Embrittlement of Iron Based Alloys*; NACE 5. 1977, NACE: Houston, TX.
87. Devereux, O.F., A.J. McEvily, and R.W. Staehle, eds. *Corrosion Fatigue: Chemistry, Mechanics, and Microstructure*; NACE 2. 1972, NACE: Houston, TX.
88. Gangloff, R.P. and M.B. Ives, eds. *Environment-Induced Cracking of Metals*; NACE 10. 1990, NACE: Houston, TX.
89. Fujii, C.T. and J.A. Smith, Environmental influences on the aqueous fatigue crack growth rates of HY-130 steel, in *Corrosion Fatigue: Mechanics, Metallurgy, Electrochemistry, and Engineering*, ASTM 801, T.W. Crooker and B.N. Leis, Editors. 1983, ASTM: West Conshohocken, PA. p. 390-402.
90. Crooker, T.W., F.D. Bogar, and W.R. Cares, Effects of flowing natural seawater and electrochemical potential on fatigue-crack growth in several high-strength marine alloys, in *Corrosion-Fatigue Technology*, ASTM STP 642, H.L. Craig, T.W. Crooker, and D.W. Hoepfner, Editors. 1978, ASTM: West Conshohocken, PA. p. 189-201.
91. Lee, E.U., et al., *Aircraft Steels*, 2009, Naval Air Warfare Center: Patuxent River, MD.
92. Frazier, J.C.W., R.K. Tayler, and A. Grollman, *Int Critical Tables of Numerical Data*, Vol. III1928, New York, NY: McGraw-Hill.
93. Shedd, M.E. and R.G. Kelly, The modeling and measurement of boundary conditions for pit size on stainless steels under atmospheric exposure conditions. *ECS Trans*, 2012. 41(25): p. 31-37.
94. Frankel, G.S., et al., Potential control under thin aqueous layers using a Kelvin Probe. *Corrosion Science*, 2007. 49(4): p. 2021-2036.
95. Stratmann, M. and H. Streckel, On the Atmospheric Corrosion of Metals Which Are Covered with Thin Electrolyte Layers .2. Experimental Results. *Corrosion Science*, 1990. 30(6-7): p. 697-714.
96. Stratmann, M., et al., On the Atmospheric Corrosion of Metals Which Are Covered with Thin Electrolyte Layers .3. The Measurement of Polarization Curves on Metal-Surfaces Which Are Covered by Thin Electrolyte Layers. *Corrosion Science*, 1990. 30(6-7): p. 715-734.
97. Kirk, W.W. and H.H. Lawson, eds. *Atmospheric Corrosion*, ASTM STP 1239. 1995, ASTM: West Conshohocken, PA.
98. Warner, J.S., *Inhibition of Environmental Fatigue Crack Propagation in Age-Hardenable Aluminum Alloys*, in PhD Dissertation, Department of Materials Science and Engineering 2010, University of Virginia: Charlottesville, VA.
99. Lee, E.U., et al., Environment-Assisted Cracking in Custom 465 Stainless Steel. *Metallurgical and Materials Transactions A*, 2011. 42(2): p. 415-423.
100. Logsdon, W.A., An evaluation of the crack growth and fracture properties of AISI 403 modified 12 Cr stainless steel. *Engineering Fracture Mechanics*, 1975. 7(1): p. 23-40.
101. Akita, M., et al., Fatigue crack propagation of 444 stainless steel welded joints in air and in 3%NaCl aqueous solution. *Materials & Design*, 2006. 27(2): p. 92-99.

102. Slifka, A.J., et al., FATIGUE CRACK GROWTH OF TWO PIPELINE STEELS IN A PRESSURIZED HYDROGEN ENVIRONMENT. *Corrosion Science*, 2013.
103. Miller, K.J. and R. Akid, The Application of Microstructural Fracture Mechanics to Various Metal Surface States. Vol. 452. 1996. 1411-1432.
104. Lynch, S., Hydrogen embrittlement phenomena and mechanisms. *Corrosion Reviews*, 2012. 30(3-4): p. 105-123.
105. Lynch, S.P., Metallographic and fractographic techniques for characterizing and understanding hydrogen-assisted cracking, in *Gaseous Hydrogen Embrittlement of Materials in Energy Technologies*, R.P. Gangloff and B.P. Somerday, Editors. 2011, Woodhead Publishing Limited: Cambridge, UK.
106. Gangloff, R.P., Hydrogen assisted cracking of high strength alloys, in *Comprehensive Structural Integrity: Environmentally Assisted Fracture*, J. Petit and P. Scott, Editors. 2003, Elsevier: New York, NY. p. 31-101.
107. Brown, B.F., Solution chemistry within cracks in steel, in *Stress Corrosion Cracking and Hydrogen Embrittlement of Iron Based Alloys*, NACE-5, R.W. Staehle, et al., Editors. 1977, NACE: Houston, TX. p. 747-750.
108. Brown, B.F., C.T. Fujii, and E.P. Dahlberg, Methods for studying the solution chemistry within stress corrosion cracks. *Journal of Electrochemical Society*, 1969. 116(2): p. 218-219.
109. Sandoz, G., C.T. FuJii, and B.F. Brown, Solution chemistry within stress-corrosion cracks in alloy steels. *Corrosion Science*, 1970. 10(12): p. 839.
110. Smith, J.A., M.H. Peterson, and B.F. Brown, Electrochemical Conditions at Tip of an Advancing Stress Corrosion Crack in Aisi-4340 Steel. *Corrosion*, 1970. 26(12): p. 539-&.
111. Andresen, P.L. and L.M. Young, Characterization of the roles of electrochemistry, convection and crack chemistry in stress corrosion cracking, in *7th Environmental Degradation of materials In Nuclear Power Systems 1995*, NACE: Breckenridge, CO. p. 579-596.
112. Turnbull, A. and J.G.N. Thomas, A Model of Crack Electrochemistry for Steels in the Active State Based on Mass Transport by Diffusion and Ion Migration. *Journal of The Electrochemical Society*, 1982. 129(7): p. 1412-1422.
113. Turnbull, A., A.S. Dolphin, and F.A. Rackley, Experimental Determination of the Electrochemistry in Corrosion Fatigue Cracks in Structural Steel in Artificial Seawater. *Corrosion*, 1988. 44(1): p. 55-61.
114. Burstein, G.T. and S.P. Vines, Repetitive Nucleation of Corrosion Pits on Stainless Steel and the Effects of Surface Roughness. *Journal of The Electrochemical Society*, 2001. 148(12): p. B504-B516.
115. Pioszak, G., 2013, University of Virginia: Charlottesville.
116. Seetharaman, V., M. Sundararaman, and R. Krishnan, Precipitation hardening in a PH 13-8 Mo stainless steel. *Materials Science and Engineering*, 1981. 47(1): p. 1-11.
117. Vasudevan, V., S. Kim, and C.M. Wayman, Precipitation reactions and strengthening behavior in 18 Wt Pct nickel maraging steels. *Metallurgical Transactions A*, 1990. 21(10): p. 2655-2668.
118. Grujicic, M., et al., Linear Friction Welding Process Model for Carpenter Custom 465 Precipitation-Hardened Martensitic Stainless Steel. *Journal of Materials Engineering and Performance*, 2014. 23(6): p. 2182-2198.
119. Midha, A. and D.E. Wert, Martensitic Age-Hardenable Stainless Steel: Versatility for Wide Array of Applications. *Advanced Materials & Processes*, 2011. 169(9): p. 30-33.
120. Dayal, R.K., Laser surface modification for improving localised corrosion resistance of austenitic stainless steels. *Surface Engineering*, 1997. 13(4): p. 299-302.
121. Rhouma, A.B., et al., Effects of surface preparation on pitting resistance, residual stress, and stress corrosion cracking in austenitic stainless steels. *Journal of Materials Engineering and Performance*, 2001. 10(5): p. 507-514.
122. Gangloff, R.P., et al., Direct Current Electrical Potential Measurement of the Growth of Small Cracks. *Small-Crack Test Methods*, ASTM ed. J.M. Larsen and J.E. Allison. Vol. STP 1149. 1992, Philadelphia.
123. Donald, J. and J. Ruschau, Direct current potential difference fatigue crack measurement techniques. *Fatigue crack measurement: techniques and applications*, 1991: p. 11-37.
124. ASTM, E466-07: Standard Practice for Conducting Force Controlled Constant Amplitude Axial Fatigue Tests of Metallic Materials.
125. ASTM, E1012-12: Standard practice for verification of testing frame and specimen alignment under tensile and compressive axial force application. *ASTM International*, 2012: p. 814-830.

126. Burns, J.T., J.M. Larsen, and R.P. Gangloff, Effect of initiation feature on microstructure-scale fatigue crack propagation in Al–Zn–Mg–Cu. *International Journal of Fatigue*, 2012. 42(0): p. 104-121.
127. Herman, W.A., R.W. Hertzberg, and R. Jaccard, A simplified laboratory approach for the prediction of short crack behavior in engineering structures. *Fatigue & Fracture of Engineering Materials & Structures*, 1988. 11(4): p. 303-320.
128. Burns, J.T., S. Kim, and R.P. Gangloff, Effect of corrosion severity on fatigue evolution in Al–Zn–Mg–Cu. *Corrosion Science*, 2010. 52(2): p. 498-508.
129. Kim, S., J.T. Burns, and R.P. Gangloff, Fatigue crack formation and growth from localized corrosion in Al–Zn–Mg–Cu. *Engineering Fracture Mechanics*, 2009. 76(5): p. 651-667.
130. Sunder, R., Fatigue as a process of cyclic brittle microfracture. *Fatigue & Fracture of Engineering Materials & Structures*, 2005. 28(3): p. 289-300.
131. Sunder, R., W.J. Porter, and N.E. Ashbaugh, The role of air in fatigue load interaction. *Fatigue & Fracture of Engineering Materials & Structures*, 2003. 26(1): p. 1-16.
132. Fawaz, S.A., Equivalent initial flaw size testing and analysis of transport aircraft skin splices. *Fatigue & Fracture of Engineering Materials & Structures*, 2003. 26(3): p. 279-290.
133. Horvath, J. and H.H. Uhlig, Critical Potentials for Pitting Corrosion of Ni, Cr-Ni, Cr-Fe, and Related Stainless Steels. *Journal of The Electrochemical Society*, 1968. 115(8): p. 791-795.
134. Liang, J. and Z. Suo, Stress-Assisted Reaction at a Solid-Fluid Interface. *Interface Science*, 2001. 9(1-2): p. 93-104.
135. Sahal, M., et al., Consequences of plastic strain on the dissolution process of polycrystalline nickel in H₂SO₄ solution. *Scripta Materialia*, 2004. 51(9): p. 869-873.
136. Stashchuk, M., Analysis of the influence of elastic deformation on the electrode potential of a metal cylinder in a medium. *Materials Science*, 2000. 36(1): p. 54-59.
137. Horner, D., et al., Novel images of the evolution of stress corrosion cracks from corrosion pits. *Corrosion Science*, 2011. 53(11): p. 3466-3485.
138. Schönbauer, B.M., et al., Fatigue life estimation of pitted 12% Cr steam turbine blade steel in different environments and at different stress ratios. *International Journal of Fatigue*, (0).
139. Zhao, W., et al., Study on the mechanism of high-cycle corrosion fatigue crack initiation in X80 steel. *Corrosion Science*, 2012. 57(0): p. 99-103.
140. Burns, J.T., R.P. Gangloff, and R.W. Bush, Effect of environment on corrosion induced fatigue crack formation and early propagation in aluminum alloy 7075-T651. DoD, 2011.
141. Gruenberg, K.M., et al., Predicting fatigue life of pre-corroded 2024-T3 aluminum. *International Journal of Fatigue*, 2004. 26(6): p. 629-640.
142. van der Walde, K. and B.M. Hillberry, Characterization of pitting damage and prediction of remaining fatigue life. *International Journal of Fatigue*, 2008. 30(1): p. 106-118.
143. Qiao, L. and X. Mao, Thermodynamic analysis on the role of hydrogen in anodic stress corrosion cracking. *Acta Metallurgica et Materialia*, 1995. 43(11): p. 4001-4006.
144. Fatemi, A. and L. Yang, Cumulative fatigue damage and life prediction theories: a survey of the state of the art for homogeneous materials. *International Journal of Fatigue*, 1998. 20(1): p. 9-34.
145. Wei, R.P. and G.W. Simmons, Recent progress in understanding environment assisted fatigue crack growth. *International Journal of Fracture*, 1981. 17(2): p. 235-247.
146. Kalnaus, S., J. Zhang, and Y. Jiang, Stress-Corrosion Cracking of AISI 4340 Steel in Aqueous Environments. *Metallurgical and Materials Transactions A*, 2011. 42(2): p. 434-447.
147. Weng, L., et al., Corrosion fatigue crack growth of AISI 4340 steel. *International Journal of Fatigue*, 2013. 48(0): p. 156-164.
148. Burns, J.T. and V.K. Gupta, 2010, University of Virginia: Charlottesville.
149. de los Rios, E.R., et al., Fatigue crack initiation and propagation on shot-peened surfaces in A316 stainless steel. *International Journal of Fatigue*, 1995. 17(7): p. 493-499.
150. Fontana, M.G., *Corrosion engineering* 2005: Tata McGraw-Hill Education.

151. Turnbull, A., Modeling of the Chemistry and Electrochemistry in Cracks—A Review. *Corrosion*, 2001. 57(2): p. 175-189.
152. Shreir, L.L., R.A. Jarman, and G.T. Burstein, *Stress Corrosion Cracking*, U. National Physics Laboratory, Editor 2000, Crown: Teddington.
153. Truman, J.E., Stress-corrosion cracking of martensitic and ferritic stainless steels. *International Metals Reviews*, 1981. 26(1): p. 301-349.
154. Gangloff, R.P. Fracture mechanics prediction of component SCC using accelerated laboratory testing. in Department of Defense Corrosion Conference. 2013. NACE International.
155. Turnbull, A., D. Horner, and B. Connolly, Challenges in modelling the evolution of stress corrosion cracks from pits. *Engineering Fracture Mechanics*, 2009. 76(5): p. 633-640.
156. Bhambri, S.K., Intergranular fracture in 13 wt% chromium martensitic stainless steel. *Journal of Materials Science*, 1986. 21(5): p. 1741-1746.
157. McEvily, A.J. and R.P. Wei, *Fracture mechanics and corrosion fatigue*, 1972, DTIC Document.
158. Pao, P.S., R.A. Bayles, and G.R. Yoder, Effect of Ripple Load on Stress-Corrosion Cracking in Structural Steels. *Journal of Engineering Materials and Technology*, 1991. 113(1): p. 125-129.
159. Crooker, T. and J. Hauser, *A Literature Review on the Influence of Small-Amplitude Cyclic Loading on Stress-Corrosion Cracking in Alloys*, 1986, DTIC Document.
160. Ford, F. and M. Silverman, Effect of Loading Rate on Environmentally Controlled Cracking of Sensitized 304 Stainless Steel in High Purity Water. *Corrosion*, 1980. 36(11): p. 597-603.
161. Mendoza, J.A. and J. Sykes, The effect of low-frequency cyclic stresses on the initiation of stress corrosion cracks in X60 line pipe steel in carbonate solutions. *Corrosion Science*, 1983. 23(6): p. 547-558.
162. SHOJI, T., et al., Effects of Stress Intensity Rate K and Stress Ratio R on Corrosion Fatigue Crack Growth Enhancement Below KISCC. *Corrosion*, 1978. 34(8): p. 276-282.
163. Fessler, R.R. and T.J. Barlo, Threshold-Stress Determination Using Tapered Specimens and Cyclic Stresses. *ASTM STP*, 1984. 821: p. 368-382.
164. Newman, J.F., The stress corrosion of steel in sodium hydroxide solution: a film-rupture model. *Corrosion Science*, 1981. 21(7): p. 487-503.
165. Page, R.A., A. McMinn, and S.J.H. Jr., Characterization of Crack Tip Electrochemistry Using a Simulated Crack. *Corrosion*, 1988. 44(9): p. 623-631.
166. Andresen, P.L. and F. Peter Ford, Life prediction by mechanistic modeling and system monitoring of environmental cracking of iron and nickel alloys in aqueous systems. *Materials Science and Engineering: A*, 1988. 103(1): p. 167-184.